

Inkjet Printing of Paper-Based Wideband and High Gain  
Antennas

Thesis by:

Benjamin S. Cook

In partial Fulfillment of the Requirements

For the Degree of:

Masters of Science

King Abdullah University of Science and Technology, Thuwal,  
Kingdom of Saudi Arabia

December, 2011

*December 7, 2011*

EXAMINATION COMMITTEE APPROVALS FORM

The dissertation/thesis of Benjamin Cook is approved by the examination committee.

Committee Chairperson Atif Shamim

Committee Member Hakan Bagci

Committee Member Ghassan Jabbour

© December 7, 2011

Benjamin S. Cook

All Rights Reserved

# ABSTRACT

---

This thesis represents a major contribution to wideband and high gain inkjet-printed antennas on paper. This work includes the complete characterization of the inkjet printing process for passive microwave devices on paper substrate as well as several ultra-wideband and high gain antenna designs. The characterization work includes the electrical characterization of the permittivity and loss tangent for paper substrate through 10 GHz, ink conductivity data for variable sintering conditions, and minimum feature sizes obtainable by today's current inkjet processes for metallic nanoparticles.

For the first time ever, inkjet-printed antennas are demonstrated that operate over the entire UWB band and demonstrate gains up to 8dB. This work also presents the first fractal-based inkjet-printed antennas with enhanced bandwidth and reduced production costs, and a novel slow wave log periodic dipole array which shows minimizations of 20% in width over conventional log periodic antennas.

## ACKNOWLEDGMENTS

---

I would like to thank Dr. Atif Shamim for the opportunities I have been provided that allowed me to produce the work presented in this thesis. His guidance and vision were a major contribution to this work. I would also like to thank Dr. Ian Foulds and Ghassan Jabbour for their willingness to allow us access to their facilities which were integral to this research.

I would also like to thank Virang Shah of Microfab Technologies and Yuri Didanko of UTDots for working with me while learning the inkjet printing process, and KACST for access to their anechoic chamber. Finally I would like to thank Manos Tentzeris for allowing me access to his printing facilities in Georgia Tech. This thesis would not have been completed without help from all of you.

---

# TABLE OF CONTENTS

---

List of Figures and Tables-----	9
<b>1. Introduction</b> -----	<b>3</b>
<b>1.1 Objectives</b> -----	<b>4</b>
<b>1.2 Challenges</b> -----	<b>5</b>
1.2.1 Substrate Characterization-----	6
1.2.2 Inkjet Fabrication on Organic and Polymer Substrates-----	6
<b>1.3 Contributions</b> -----	<b>7</b>
<b>1.4 Thesis Organization</b> -----	<b>8</b>
<b>2. Review of Literature</b> -----	<b>9</b>
<b>2.1 Polymer and Organic Substrates</b> -----	<b>9</b>
<b>2.2 The Inkjet Printing Process</b> -----	<b>12</b>
2.2.1 Inkjet Printing Techniques-----	12
2.2.2 Conducting Inks-----	15
2.2.3 Printers-----	17
<b>2.3 Inkjet Printed Antennas</b> -----	<b>20</b>
2.3.1 Simple Sensor-Integrated Inkjet-printed Antennas-----	21
2.3.2 Printed Circuit Integrated Inkjet-printed Antennas-----	22
2.3.3 Fully Printed Systems-----	23
<b>2.4 Summary</b> -----	<b>24</b>
<b>3. Characterization</b> -----	<b>25</b>
<b>3.1 Inkjet Printing Process</b> -----	<b>25</b>

3.1.1	Microfab Jetlab II Printing	26
3.1.2	Dimatix 2830 Printing	29
3.1.3	Printer Comparison	32
3.1.4	Conductivity	33
3.1.4.1	Heat Sintering	33
3.1.5	Laser Sintering	38
3.1.6	Conductivity Summary	39
<b>3.2</b>	<b>Substrate Characterization</b>	<b>41</b>
3.2.1	Ring Resonator Technique	42
3.2.2	T-Resonator Technique	47
3.2.3	Transmission Line Method	54
<b>3.3</b>	<b>Summary</b>	<b>56</b>
<b>4.</b>	<b>Wideband Fractal-Based Inkjet Printed Antennas</b>	<b>--Error! Bookmark not defined.</b>
<b>4.1</b>	<b>2.4 GHz Sierpinski Fractal Monopole</b>	<b>58</b>
4.1.1	Sierpinski Monopole Design	60
4.1.2	Sierpinski Monopole Fabrication	63
4.1.3	Sierpinski Monopole Measurements	65
4.1.4	Summary	67
<b>4.2</b>	<b>UWB Sierpinski Monopole</b>	<b>68</b>
4.2.1	UWB Sierpinski Monopole Design	69
4.2.2	UWB Monopole Measurements	74
4.2.3	Summary	78
<b>4.3</b>	<b>UWB Sierpinski Monopole Version 2</b>	<b>79</b>
4.3.1	UWB Sierpinski Monopole Version 2 Measurements	80
4.3.2	Summary	83
<b>5.</b>	<b>Directive UWB Inkjet-Printed Antennas</b>	<b>84</b>
<b>5.1</b>	<b>UWB Antipodal Vivaldi</b>	<b>86</b>

---

5.1.1	Antipodal Vivaldi Design	87
5.1.2	Antipodal Vivaldi Measurements	91
5.1.3	Summary	95
<b>5.2</b>	<b>UWB Antipodal Vivaldi Version 2</b>	<b>96</b>
5.2.1	UWB Antipodal Vivaldi V2 Design	97
5.2.2	UWB Antipodal Vivaldi V2 Measurement	99
5.2.3	Summary	103
<b>5.3</b>	<b>Applied Log Periodic Dipole Array with Slow Wave Structures</b>	<b>104</b>
5.3.1	Log Periodic Dipole Array Design	105
5.3.2	Log Periodic Measurements	111
5.3.3	Summary	113
<b>6.</b>	<b>Conclusions</b>	<b>114</b>
6.1	Conclusions	114
6.2	Future Work	114
	<b>Works Cited</b>	<b>115</b>



---

# LIST OF FIGURES AND TABLES

---

Figure 1: Ink Jetting Technique .....	12
Figure 2: Continuous vs. DOD Inkjet-Printing .....	14
Figure 3: Inkjet Actuator Types.....	15
Figure 4: Sintering Effect on Nanoparticle Inks.....	16
Figure 5: Wetting Angle of Ink on Substrate .....	17
Figure 6: Single Nozzle Printing Technique .....	18
Figure 7: Multi Nozzle Printing Technique.....	18
Figure 8: Ink Droplet Formation.....	26
Figure 9: Poor Ink Droplet Formation .....	27
Figure 10: Calibration Structs.....	28
Figure 11: Transient Effects .....	28
Figure 12: Dimatix Drop Watcher .....	30
Figure 13: Dimatix 10pL Calibration Structures .....	30
Figure 14: Dimatix 1pL Calibration Structures .....	31
Figure 15: Minimum Spacing Pattern .....	31
Figure 16: Sheet Resistance Vs. Temperature for Cabot Ink .....	35
Figure 17: Cabot Vs. UT Dots Sheet Resistance Vs. Temperature .....	36
Figure 18: Cabot Ink Sheet Resistance Vs. Time .....	36
Figure 19: Thickness of Printed Cabot Ink Layers on Glass .....	37
Figure 20: Laser Sintering.....	38
Figure 21: Paper 120C (Left) 200C (Right).....	38

---

Figure 22: Laser Vs. Heat Sintering for 5 Layers of Cabot Ink.....	39
Figure 23: Ring Resonator.....	42
Figure 24: Microstrip Structure .....	43
Figure 25: Fabricated PET Ring Resonator .....	45
Figure 26: PET Ring Resonator Return Loss.....	46
Figure 27: PET Ring Resonator Permittivity.....	46
Figure 28: Microstrip T-Resonator .....	47
Figure 29: Microstrip T-Resonator .....	50
Figure 30: Paper T-Resonator Insertion Loss.....	51
Figure 31: Extracted Relative Permittivity of Photo Paper .....	52
Figure 32: Extracted Loss Tangent of Photo Paper .....	52
Figure 33: Top – Sputtered Line, Bottom - Printed Line .....	53
Figure 34: Extracted Permittivity of Kapton and PET.....	53
Figure 35: Transmission Line Loss Tangent Extraction.....	54
Figure 36: Insertion Loss of Two Lengths of Transmission Line .....	55
Figure 37: Loss Tangent Comparison Between Methods.....	55
Figure 38: Microstrip T-Resonator (Units in mm) .....	60
Figure 39: Return Loss for Fractal Iterations .....	61
Figure 40: Increased Match by Tapering Ground Plane .....	62
Figure 41: Simulated Radiaton Pattern of Sierpinski Monopole.....	62
Figure 42: Mask for Sierpinski Fractal Monopole.....	63
Figure 43: Layer Alignment for Printed Structures.....	64
Figure 44: Fabricated Sierpinski Monopole.....	65

---

Figure 45: Mask for Sierpinski Fractal Monopole .....	65
Figure 46: Increased Match by Tapering Ground Plane .....	67
Figure 47: UWB Monopole Design .....	68
Figure 48: UWB Monopole .....	69
Figure 49: Sweep of Ground Tapering Angle on UWB Monopole .....	70
Figure 50: Fractal vs. Non Fractal Matching Network.....	71
Figure 51: Simulated Pattern for UWB Monopole .....	72
Figure 52: Simulated Gain vs. Frequency of the UWB Monopole Antenna .....	73
Figure 53: Fabricated UWB Monopole .....	74
Figure 54: UWB Monopole Return Loss Measurement.....	74
Figure 55: Simulated vs. Measured Gain and Radiation Pattern of UWB Monopole.	77
Figure 56: Max Realized Gain vs. Frequency.....	77
Figure 57: Version 2 UWB Monopole Antenna .....	79
Figure 58: First and Second Version of the UWB Monopole.....	80
Figure 59: Fabricated UWB Monopole V2.....	80
Figure 60: UWB Monopole Version 2 Return Loss Measurement .....	81
Figure 61: UWB Monopole Version 2 Pattern Measurements .....	82
Figure 62: UWB Monopole Version 2 Gain Vs. Frequency.....	83
Figure 63: UWB Antipodal Vivaldi .....	86
Figure 64: Vivaldi Transition .....	87
Figure 65: Vivaldi Transition Return and Insertion Loss.....	87
Figure 66: $\alpha = 0.04$ (Left), $0.055$ (Middle), $0.07$ (Right) .....	88
Figure 67: Return Loss for Different Alpha Values.....	89

---

Figure 68: Vivaldi Radiation Pattern at 6 GHz.....	89
Figure 69: Vivaldi Gain vs. Frequency .....	90
Figure 70: Fabricated Vivaldi.....	91
Figure 71: Vivaldi Measurement Vs. Simulation.....	91
Figure 72: Vivaldi Radiation Pattern.....	94
Figure 73: Vivaldi Gain vs. Frequency .....	95
Figure 74: UWB Antipodal Vivaldi V2.....	96
Figure 75: Vivaldi Version 1 Time Domain Signal .....	96
Figure 76: Vivaldi V2 vs. V1 Return Loss.....	97
Figure 77: Minimized Time Domain Reflections .....	98
Figure 78: Fabricated Vivaldi V2 .....	99
Figure 79: Vivaldi V2 Return Loss Measurements.....	100
Figure 80: Vivaldi V2 Radiation Pattern Measurements .....	102
Figure 81: Vivaldi V2 Gain Measurements.....	103
Figure 82: Energy Harvesting from UHF Band.....	104
Figure 83: Log Periodic Design.....	105
Figure 84: Stepped Capacitor 400% Dipole Width (Top), 200% (Middle), 0% (Bottom).....	107
Figure 85: Return Loss for Stepped Capacitor Dipoles.....	107
Figure 86: Final Log Periodic .....	108
Figure 87: Log Periodic Simulated Return Loss.....	109
Figure 88: Log Periodic Simulated Gain.....	109
Figure 89: Log Periodic Simulated Radiation Pattern .....	110

---

Figure 90: Fabricated Log Periodic.....	111
Figure 91: Log Periodic Simulated and Measured Return Loss.....	112
Figure 92: Log Periodic Simulated and Measured Gain.....	113
Table 1 : Taxonomy of Inkjet Printing Techniques.....	13
Table 2 : List of Inkjet-printed Antennas and their Properties.....	21
Table 3: Printer Comparison Chart.....	32
Table 4: Resonator Dimensions .....	50
Table 5: Wideband Monopole Types.....	58
Table 6: Fractal Pattern Examples .....	59
Table 7: Sierpinski Fractal Iterations.....	59
Table 8: Triangular Monopole with Sierpinski Progression .....	60
Table 9: Comparison of Measured and Simulated Sierpinski Monopole Parameters.....	67

---

# 1. INTRODUCTION

---

As electronics technology has progressed, market demands have caused devices to become smaller, lighter weight, and lower cost than ever before. One of the promising areas of research that is allowing advances in these three areas is fabrication on low cost organic substrates such as paper and polymers using the inkjet printing process. Organic and polymer substrates offer the unique advantages of being much cheaper, lighter, and in the case of organics more environmentally friendly in processing and disposal than current substrates such as silicon and FR-4. They have the additional advantage of providing flexibility. Coupled with inkjet printing of silver nanoparticles – a technology that has recently brought ink conductivities close to that of bulk metals [1]– cheap and flexible devices can be fabricated quickly and at minimal cost. Another major advantage is that inkjet printing on organic and polymer substrates can be run reel to reel or roll to roll making the transition from the lab to large scale production easier and more cost effective than wafer by wafer processing [2]. Increased demands for wearable devices used for medical monitoring, cheap and flexible RFID tags for inventory tracking, and disposable, environmentally friendly devices all can be met using this new fabrication strategy.

Flexible device fabrication has been around since the early 1960's when light weight solar cells and ribbon cabling were required for satellite and space shuttle applications [2]. And by the early 1970's, thin film transistor (TFT) matrix displays on polymer substrates had been produced. But, up until the early 2000's, flexible

substrates had mainly been used for low frequency screen technology and cabling. Recent research has moved toward being able to create high frequency devices such as MHz TFT's, antennas for RFID, and other microwave devices to eventually allow entire systems such as radio transceivers to be fabricated on flexible and organic substrates [3]. But in order to make this happen, the complexities of inkjet printing conductive structures on flexible substrates and using these substrates for applications at frequencies far beyond current use have to be overcome.

## 1.1 Objectives

This thesis tackles the challenges of advancing antenna design on organic substrates using the inkjet printing of conductive structures with silver nanoparticle inks – using paper as the primary substrate. The main areas of focus include:

- Organic and polymer substrate characterization for microwave frequencies including:
  - Photo Paper, Kapton, and Polyethylene (PET)
- Inkjet printing of conductive structures on flexible and organic substrates
- The design of wideband and ultra-wideband (UWB) inkjet-printed antennas
- Applying inkjet-printed antennas to real-world problems

The results of this work bring together the basic building blocks of fabrication and characterization to produce some of the first ever UWB antennas printed on paper as well as several applied antenna designs to address real world problems.

## 1.2 Challenges

Since organic and polymer substrate use at microwave frequencies and the inkjet printing of conductive structures with silver nanoparticle inks are relatively new fields [2], there are several basic foundations that need to be built to allow for successful device fabrication which include a few main areas:

- Characterizing flexible substrates at microwave frequencies to determine their material properties
- Designing reliable processes for inkjet printing conductive structures on organic and polymer substrates which requires tuning of
  - Ink/Substrate compatibility
  - Ink layer thickness
  - Sintering temperature
- Finding effective ways to measure structures as connector mounting on thin and temperature sensitive materials is an issue
- Designing antennas which exploit benefits of thin organic substrates

While other issues do come up, these are the main areas that will be explored in this thesis as these are the main problems that need to be solved for inkjet printing on organic and polymer substrates to become an effective and reliable fabrication technique.



### **1.2.1 Substrate Characterization**

Currently very few flexible substrates are available that are characterized for microwave frequencies. The majority of flexible polymer substrates that are electrically characterized are used in discrete capacitor fabrication as a dielectric layer and are therefore only characterized for a few hundreds of megahertz. And, organics such as paper have only recently been characterized through 2GHz [4] which is still not high enough for many microwave applications such as the Wifi (5GHz) and UWB (3.1 – 10.6) bands. To allow for accurate modeling of microwave circuits and antennas using these substrates, it is critical to characterize the relative permittivity  $\epsilon_r$  and loss tangent  $\tan\delta$  of these materials for higher frequencies.

### **1.2.2 Inkjet Fabrication on Organic and Polymer Substrates**

Several fabrication processes have been used for fabricating on flexible substrates including inkjet printing, screen printing, photolithography, and shadow masking [4], [5], [6]. Inkjet printing silver nanoparticle inks which is used in this work is a relatively new process and therefore has no distinct method or prior recipe to follow. Before being able to design antennas and microwave structures for this process, the process limitations need to be discovered and the process needs to be characterized. For example, ink droplet size and formation is a function of the ink viscosity, surface tension, temperature, transducer waveform, and a variety of other variables. And, the conductivity of the final structures is a function of the ink droplets as well as substrate surface roughness, sintering temperature, number of layers printed, etc... The vast array of variables and the recent adaptation of

inkjetting to printing microwave structures means much experimenting is required to develop reliable and effective processes.

### 1.3 Contributions

- **A fully characterized process for inkjet printing:** This thesis demonstrates characterization of inkjet printing for microwave devices including feature size realization on Dimatix and Microfab printers, ink conductivity of Cabot and UTDots silver nanoparticle ink with a variety of sintering methods, and characterization of the permittivity and loss tangent of Paper, Kapton, and PET.
- **The smallest UWB antenna realized with inkjet printing:** In this thesis, a paper-based UWB antenna is proposed that is sixteen times smaller than current inkjet-printed UWB antennas.
- **The highest gain antenna realized with inkjet printing:** A Vivaldi antenna on paper that demonstrates 8dB gain – 5 dB higher than currently published paper-based antennas – is demonstrated.
- **A novel design for miniaturization of the log periodic antenna:** Slow wave structures are used to minimize the width of a log periodic by 20% which is implemented on a paper-based inkjet-printed log periodic.

## 1.4 Thesis Organization

- Chapter 2 of the thesis gives an overview of the inkjet-printing process and discusses the current status of the inkjet-printed antenna field including a summary of the current inkjetted antennas in literature along with applications that have been addressed.
- Chapter 3 discusses the characterization of two separate inkjet printing processes using a Microfab Jetlab II and Dimatix inkjet printing system. The chapter then discusses the microwave characterization of several organic and polymer substrates.
- Chapter 4 includes the design, simulation, and measurement of several wideband and ultra-wideband antennas using fractal patterns to reduce size, and decrease fabrication cost.
- Chapter 5 discusses the design, simulation, and measurement of three directive wideband antennas including two renditions of the antipodal Vivaldi and a log periodic that provide high gain on paper substrates.

---

## 2. REVIEW OF LITERATURE

---

This chapter gives an overview of the inkjet printing process and its employment in the fabricating of RF and microwave devices. It discusses the role that flexible substrates have played in device fabrication, including a justification on why they are beneficial in certain cases over standard microwave substrates. It then delves into the details of the inkjet printing process and how it has evolved into a process for fabricating microelectronics. And finally, previous work in inkjet-printed antennas on organic and polymer substrates is reviewed which provides a foundation for the work presented in this thesis.

### 2.1 Polymer and Organic Substrates

Organic and polymer substrates such as paper possess a wide array of benefits when it comes to microwave device and antenna fabrication. These substrates have recently become of interest in the literature. For example, Yang et al. have been using paper as a substrate for low-frequency RFID tag printing [7], [8], [9], [4], Mohammed et al. have demonstrated a patch antenna on Kapton [10], and Hyung et al. have demonstrated a monopole on PET [11]. However, only Yang et al. have characterized the substrate up to 2.4GHz [4].

Paper, Kapton, and Polyethylene are widely used materials in many fields which means they are much cheaper than typical microwave substrates. Paper is referenced as being one of the cheapest materials currently produced on the planet [12]. As a comparison, paper substrate is nearly one hundred times cheaper than an

equivalent sized FR4 substrate. These substrates are also extremely light weight and much more pliable than current microwave substrates lending them as better substrates for applications such as wearable antennas where weight and conformity to the body are important issues.

Aside from the obvious benefits of these substrates, there are several physical characteristics which make them interesting prospects for antennas, microwave systems, and packaging. Many organic and polymeric substrates have a low permittivity [12]. While low permittivity increases the size of antennas, it has the benefits of enhancing the bandwidth and decreasing surface wave propagation which in turn enhances an antenna's radiation performance [13]. The substrates are also inherently insulating so losses due to substrate conductivity are negligible unlike silicon substrates. However, there are also a few physical characteristics which are considered disadvantages. One being that the dielectric losses in paper are higher than standard microwave substrates as paper has not been tailored for microwave operation [12]. It is also important to design structures that are able to perform on substrates that flex as unlike FR4 and Rogers material, organic and polymer substrates are flexible – if used properly though, this can be used to the designers advantage.

One of the major advantages that makes fabricating on polymer and paper substrates such a promising process is that system on package (SOP) designs can be realized. SOP is a fabrication technique where components are integrated vertically as well as horizontally by using multiple layers and connections by vias or proximity

coupling which translates to appreciable size reductions in packaging . It is also very easy to form cavities in these substrates using wet etching or laser cutting allowing IC's to be embedded within the stack-up. With this concept the DC wiring, interconnects, and antennas can all be integrated into a multi-layer paper or polymer package with minimum size and weight. And, in the case of polymer packaging, the package is already inherently hermetically sealed.

## 2.2 The Inkjet Printing Process

The inkjet printing process has become an area of interest in the fabrication world over the last 10 year due to the fact that inkjet printing can be used on a wide array of substrates and can deposit almost any material that can be put into a liquid form [1]. Inkjet printing is a lithography free process which removes the need for masks, exposure equipment, and etching which leads to large time cuts and cost reductions in the fabrication process. It is mainly used as an additive process which means it deposits the material that will be part of the final structures, but, resist-like material can also be deposited for use as an etching mask and removed after etching. The inkjet printing process has been used to create light emitting diodes, TFT's, conducting lines, and liquid crystal displays [1].

### 2.2.1 Inkjet Printing Techniques

Inkjet printing is a relatively simple concept. A liquid ink is loaded into a reservoir which feeds a nozzle as seen in Figure 1. As the nozzle or substrate is moved horizontally, one of several methods is used to eject a drop of ink from the nozzle which then hits and adsorbs to the substrate. By moving the nozzle and ejecting droplets at the correct points, patterned features are created. Inkjet printing comes in several varieties. A simple taxonomy of the different processes is shown in Table 1.

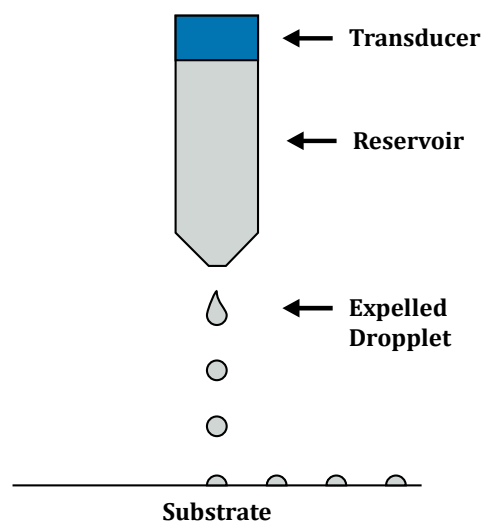


Figure 1: Ink Jetting Technique

Table 1 : Taxonomy of Inkjet Printing Techniques

<b>Inkjet Printing Techniques</b>	
<b>Drop on Demand</b>	Thermal Inkjet
	Piezo Inkjet
	Electrostatic Inkjet
	Acoustic Inkjet
<b>Continuous</b>	Piezo Inkjet
	Thermal Inkjet

The two main differences between inkjet printing techniques are drop on demand (DOD) and continuous inkjet printing. Continuous inkjet printing works by continuously ejecting drops from the reservoir at a constant frequency by setting up an acoustic wave with a transducer. When the drops exit the reservoir it is given an electrostatic charge using charging plates. It is then either directed towards the substrate or into a collection bin with a pair of electrodes. This method allows for patterning without turning off the jet which helps mitigate clogging of the nozzle due to ink drying and inconsistent excitation of the ink, and allows for faster fly velocities [1] – which is the velocity at which the substrate moves past the nozzle. This process is best suited for commercial printing as it is usually only compatible with one type of ink and requires inks that can be electrostatically charged [14].

DOD printing is similar to continuous printing in that a transducer generates a pressure wave in the ink reservoir which ejects a drop of ink. However, a signal is only sent to the transducer when a drop is required instead of continuous operation. DOD printing allows for a wider range of inks with varying viscosities and surface tensions to be accounted for by changing the signal to the transducer and can print



at higher resolutions [1]. But, clogging is still a prominent issue due to the inconsistent waveform applied to the reservoir and ink drying. Continuous and DOD printing are shown in Figure 2.

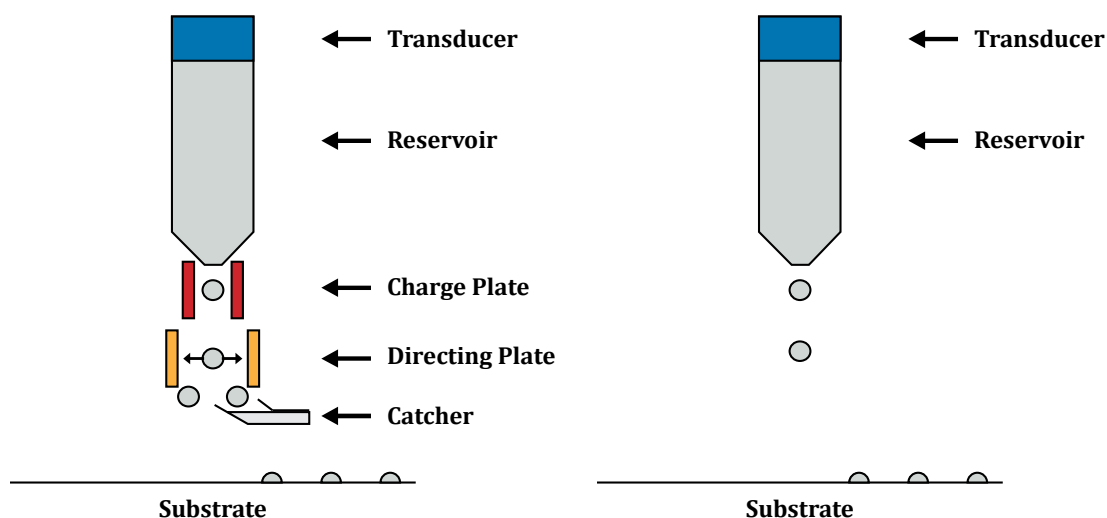


Figure 2: Continuous vs. DOD Inkjet-Printing

Within each type of printing, several types of actuators are used including thermal, piezo, electrodynamic, and acoustic. Thermal and piezo actuators work by inducing a pressure wave in the reservoir which expels a drop from the nozzle while electrodynamic and acoustic actuators work by disrupting the surface tension of the meniscus formed at the end of the nozzle causing a drop to jet towards the substrate [14]. Thermal actuators are typically used in commercial and office inkjet printers where the same ink is used. This allows the thermal expansion properties of the ink to be controlled which results in consistent jetting. For research projects where many different types of inks with different thermal properties may be used, Piezo systems are more common. Acoustic systems are nearly exclusive to continuous jet printers found in industrial production and are an extension of the piezo nozzle as

the acoustic wave is generated with a piezo crystal [1]. Figure 3 demonstrates the different types of actuators available.

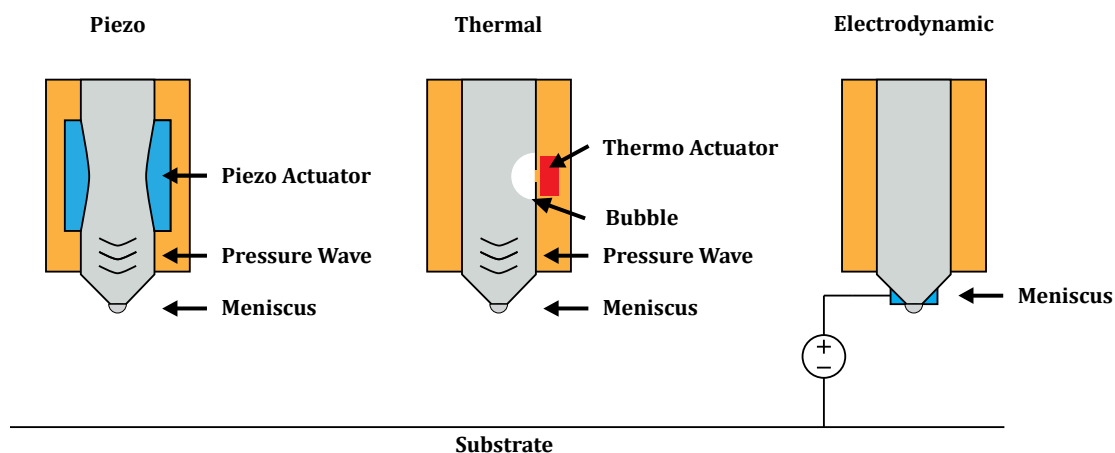


Figure 3: Inkjet Actuator Types

### 2.2.2 Conducting Inks

The ink is perhaps the most important part of the inkjet printing process as the properties of the ink effect dispensing from the nozzle as well as droplet formation on the substrate. The viscosity, surface tension, thermal properties, and chemical compatibility with substrates and dissolved material are all very important in creating a reliable printing process. There are two main types of inks used in inkjet printing: dye-based, and pigment-based. Dye based inks dissolve the delivered material into solution and evaporate the solvent away upon deposition while pigment based inks disperse the material to be delivered throughout the ink using dispersing agents to prevents clustering [15].

While there are several types of conductive inks such as PEDOT:PSS [16], organic complex-based silver, and metallic nanoparticle [1], the inks used in this thesis are

silver nanoparticle-based inks with an organic coating which can have conductivity near that of bulk silver under the correct processing conditions. Metallic nanoparticle inks are a very recent creation, with the earliest published work starting around eight years ago. These inks have allowed for realization of high frequency conducting structures on polymer and organic substrates. The reason nanoparticle inks are such a large leap forward for pigment-style inks is that when the ink is deposited on the substrate, the silver particles are in close proximity but are not one continuous conductor. This means the conductivity is rather low. Sintering or heating of the substrate is required to burn away the dispersant coating and melt the particles together to obtain high conductivities. Silver nanoparticles have the unique property of having a melting point much lower than that of bulk silver which is  $960^{\circ}\text{C}$  [15]. This is due to the high surface to volume ratio and allows for inkjet printing on substrates with much lower processing temperatures such as paper and polymers since sintering can occur as low as  $80^{\circ}\text{C}$ . Conductivities have been reported up to  $10^5\text{ S/m}$  [15] whereas conductive polymer inks of the past were around  $10^1\text{ S/m}$ . An example of pre and post-sintered ink is shown in Figure 4.

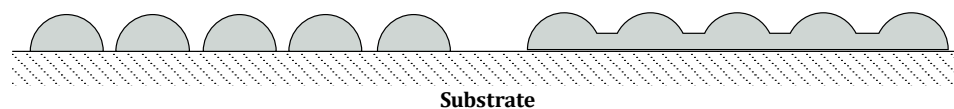


Figure 4: Sintering Effect on Nanoparticle Inks

Another important quality of an ink beyond conductivity is substrate wetting. The nanoparticles are dispensed in a solvent, dispersant, and a series of buffers which

have a specific surface energy. When the ink droplet hits a substrate that is non-porous, the difference in surface energies between the droplet and substrate either cause the droplet to spread and wet the surface, or contract into ball on the surface. This quality is usually defined by the wetting angle  $\theta$ , which is the angle at which the droplet contacts the substrate [14]. Too high of a wetting angle and the droplet tends to “bounce” when it hits the substrate, and too low of a wetting angle causes large amounts of drop spreading which smears features and lowers conductivity as the silver particles are farther apart. An illustration is shown in Figure 5 of a droplet coming in contact with the substrate at wetting angle  $\theta$ . The importance of wetting angle means different inks must be formulated for different substrates. However, if a porous substrate is used such as paper, the ink is absorbed by the pores and wetting is not as much of an issue. For this reason, paper is the main substrate used in this thesis.

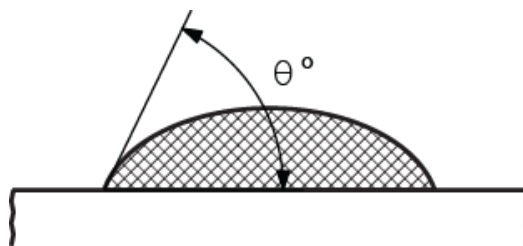


Figure 5: Wetting Angle of Ink on Substrate

### 2.2.3 Printers

There are several printers available for inkjet printing silver nanoparticle inks and they are best classified as single and multi-nozzle systems. Single nozzle systems such as the Microfab Jetlab [17] printers pass the substrate on an x-y moveable

stage under the nozzle as the pattern is jetted. The drop spacing and position is determined by the movement of the stage and can be controlled down to several microns or less [1]. An illustration is shown in Figure 6.

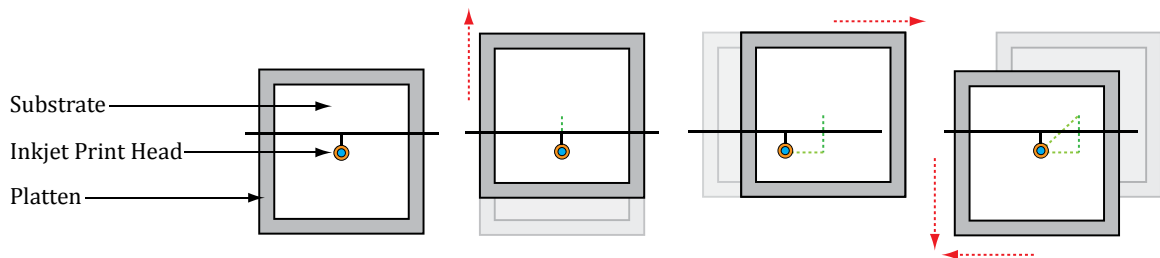


Figure 6: Single Nozzle Printing Technique

Multi-nozzle systems such as the Dimatix [18] and Ulvac M-Series [19] are more complex in configuration but benefit from faster print times and higher reliability with up to 16 nozzles jetting at once. Multi-nozzle systems work by aligning all nozzles in a row and angling them at what is called the “sabre angle”. The sabre angle determines the y-spacing of the drops, while the movement of the print head along the substrate in the x-direction determines the x-spacing. This is shown in Figure 7.

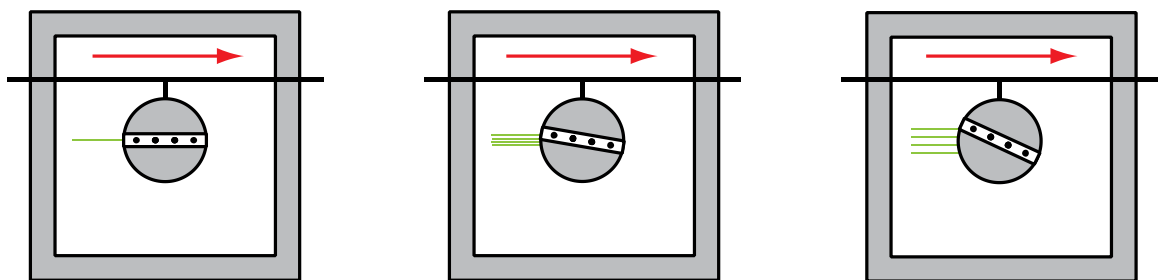


Figure 7: Multi Nozzle Printing Technique

Currently the commercially sold multi nozzle systems for research purposes contain up to sixteen nozzles which reduces print time and ruined samples from nozzle clogging tremendously.

## 2.3 Inkjet Printed Antennas

The first published inkjet-printed antennas started to appear in literature around 2007 and were geared towards RFID integration on flexible substrates. RF identification for supply chain management, pharmaceutical tracking, inventory control, and other applications is a fast growing market [12]. And, with such a large potential market base, a successful RFID tag needs to be cheap, effective, and preferably environmentally friendly due to the large volume that will be produced. These demands are all able to be met using paper or polymer based inkjet-printed tags which are flexible, cheap, and green [12].

Because of this, nearly all inkjet-printed antenna research up until now has focused on RFID based antennas and RFID antenna-based sensors. A table of all inkjet-printed antennas found in literature is shown below in Table 2. As shown, the majority of the antennas operate in the UHF band specifically from 400 – 900 MHz which is where the American and European RFID bands exist [20].

The rest of this section will focus on applications of published inkjet-printed antennas to show the state of the printed antenna field and justify the work performed in this thesis as a contribution to current work.

Table 2 : List of Inkjet-printed Antennas and their Properties

Antenna Type	Frequency (MHz)	~ Gain (dBi)	Bandwidth (MHz)	Size (cm <sup>2</sup> )	Material
Dipole over AMS [21]	400	3.5	4	100 x 100	Paper
Wideband Dipole [22]	433	N/A	250	8 x 15	Paper
Meandered Dipole [20]	854	1.94	190	12.5 x 5	Paper
Quadratic Bowtie [23]	865	1.33	30	9.2 x 3.2	Paper
CPW Monopole [24]	904	0.7	220	8.5 x 8	LCP
Z-monopole [25]	904	N/A	132	5 x 5.6	Paper
Saw RFID Tag [20]	2450	1.9	100	4.2 x 1.4	Paper
Transparent Patch [26]	2500	N/A	100	15 x 17	Polyethylene
Proximity Fed Patch [27]	4900	N/A	150	3 x 4.5	Kapton
Patch Array [28]	5000	N/A	400	2.5 x 2	Kapton
UWB Monopole [29]	2e3 – 8e3	N/A	6000	5.8 x 5.8	Paper

### 2.3.1 Simple Sensor-Integrated Inkjet-printed Antennas

A huge advantage of RFID over other technologies – specifically passive RFID – is that it can be remotely poled and powered by a wireless reading device meaning no battery replacement or power cords. By integrating sensors into RFID based antenna systems, large amounts of sensors can be distributed and interrogated cheaply and with minimal hassle.

Yang et al. have demonstrated an entirely passive printed RFID-based gas sensor which can detected ammonia (NO<sub>3</sub>) and other noxious gasses (NO<sub>x</sub>) by integrating single-walled carbon nanotubes (SWCNT's) between the arms of a printed bowtie-like dipole antenna operating at 900MHz [7]. As the gas hits the SWCNT's, their impedance and reactance nearly double which causes backscatter from the antenna



to change due to a mismatch in SWCNT impedance and the antenna impedance. This allows the polling device to perform real-time gas level monitoring by watching the back-scatter from these RFID sensors. The gain for the antenna is not published leaving efficiency difficult to infer from the results.

Vyas et al. have demonstrated yet another SWCNT based gas sensor which utilizes a patch antenna loaded with a SWCNT stub at the top radiating edge of the patch [9]. By activating the SWCNT's with ammonia gas, the resonant frequency of the patch shifted by nearly 1% (50MHz in 6.8GHz), allowing for sensing of gas flow over the sensor. The only issue with the sensor is that an air gap was required between the patch substrate which was paper and the ground plane as the high losses in the paper substrate would dampen the resonance otherwise. This makes antenna fabrication appreciably more difficult. Again, gain has not been measured for this antenna.

### **2.3.2 Printed Circuit Integrated Inkjet-printed Antennas**

Advancing beyond simple sensor-integrated printed antennas, printed circuit boards (PCB's) have been inkjet-printed on the same substrate as the antenna allowing entire system integration on a single piece of paper.

Tentzeris et al. have demonstrated a dipole printed antenna with a printed circuit layout on paper that integrates a battery, controller unit, and temperature sensor for remote temperature monitoring [8]. The RFID dipole antenna operates around 900MHz. The discrete circuit components are mounted using a conductive epoxy as solder is not compatible with paper substrates. This is the first demonstrated

example of an entire package on paper substrate. The design of the dipole allows for 50% bandwidth operation which is quite high for a dipole. However, some of this may be due to loss, and again, gain is not published so this is difficult to compare with highly conductive antennas. The same temperature sensor circuitry was integrated with a co-planar waveguide (CPW) monopole antenna to achieve similar results.

Vyas et al. have integrated circuitry in PCB form for a solar powered RFID tag with a printed z-shaped monopole antenna which is intended for bio-monitoring or other remote sensing applications which would benefit from removing a battery from the system [9]. The prototype proves that these sensors can be self-sustaining and lower cost due to paper or polymer based fabrication of the antennas and PCB's.

### **2.3.3 Fully Printed Systems**

A great demonstration of where this technology is headed is demonstrated by Chen et al. in which a fully integrated system is printed with aerosol jetted carbon nanotube FETs and inkjet-printed patch antennas to create a phased array on Kapton operating at 5GHz [28]. The performance of the system is measured in normalized power, so we don't get a good idea of the overall efficiency, but the system produces working results which is a big step forward for inkjet-printed devices.

## 2.4 Summary

The status of the inkjet-printed antenna field has been reviewed in this chapter. A review of published inkjet-printed antennas and sensors has been presented which covers the majority of published data as of this writing. While many unique antenna designs have been produced for the UHF RFID bands, and several novel sensors exploiting the inkjet printing technology have been implemented, there is still a lot of improvement to be made.

Very few inkjet-printed antennas have published gain measurements, or comparison of radiation patterns between simulation and measurement. This may be due to simulation/measurement discrepancies, and the fact that inkjet printing doesn't produce highly efficient antennas because of the lower conductivities received from inkjet inks. Either way, these are areas needed to be improved on for advancement of the inkjet-printed antenna field.

Another observation is that there are very few wideband and UWB inkjet-printed antennas. These are very important for wearable and body monitoring systems where high data rates are required. The design of highly directive inkjet-printed antennas also has a gap to be filled as the majority of current printed antennas are monopole or dipole-style which offer very low directivities. The inkjet-printed antenna field has a long way to go, and the work in this the following chapters strives to fill some of the gaps presented here.

---

## 3. CHARACTERIZATION

---

For accurate modeling and simulation of microwave devices and antennas, knowing the electrical properties of the substrate being used such as the electrical permittivity ( $\epsilon_r$ ) and loss tangent ( $\tan\delta$ ), as well as the capabilities and characteristics of the fabrication process are essential. In turn, accurate modeling drastically cuts down on design iterations due to modeling and measurement discrepancies. Characterization is also important to ensure that the electrical and process properties are appropriate for the specific application being designed for. Usually these properties are available from the manufacturer for typical RF substrates. However, for this thesis, unusual substrates such as paper, Kapton, and PET are being utilized so characterization is necessary. The work in this chapter includes the electrical characterization of several polymer and organic substrates; Polyethylene, Kapton, and Photo Paper – which is the main substrate of interest – along with the process characterization of two inkjet printing fabrication techniques.

### 3.1 Inkjet Printing Process

Two separate inkjet printing processes have been investigated in this thesis due to the availability of printers. The first printer is the Microfab Jetlab II which is a single nozzle drop on demand (DOD) printer that uses piezo actuation of a glass tube for dispensing. The second is the Dimatix 8120 which is a sixteen nozzle DOD printer that uses MEMS-based piezo actuation for drop dispensing.

### 3.1.1 Microfab Jetlab II Printing

The Microfab Jetlab II is the initial printer utilized for printing microwave structures and antennas. The inks provided by UTDots [30] have been formulated individually for Kapton, PET, and Paper. The Jetlab II works by feeding a glass tube with a reservoir of ink. The glass tube is surrounded by piezo material and the reservoir is connected to a pressure/vacuum line which adjusts the static force at the end of the nozzle which allows for different viscosity inks. Figure 8 shows droplet formation from the end of the glass tube over time as the piezo contracts. By using image analysis software provided with the printer, it has been found that the droplet volume is approximately 51pL which is near the 60pL specification for the piezo nozzle used.

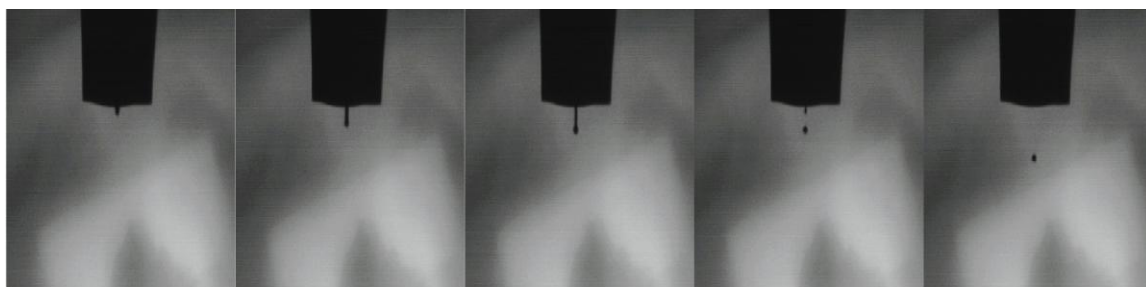


Figure 8: Ink Droplet Formation

In order to obtain the circular droplet shown in Figure 8, the back pressure, waveform fed to the piezo, and the ink temperature all need to be set correctly. Small differences in barometric pressure, humidity, and room temperature require the settings to be changed almost daily. An image of imperfect droplets as well as the effects on printed structures is shown in Figure 9. The two images on the left show droplets with satellites – or secondary droplets forming with the primary drop

– and the image on the right shows the effects of imperfect droplets on the edge of a structure. Where there should be a clean edge near the middle of the image, it is smeared, and smatterings of ink are seen on the left hand side where no ink should appear. This spatter extends nearly 200 $\mu\text{m}$  from the printed structure. Getting the perfect droplet is quite difficult with this printer and the silver nanoparticle inks. And, once the perfect drop has been attained, maintaining that droplet during the printing process remains an issue as this printer has no automatic cleaning cycles. Clogging and distorted droplets are very common occurrences.

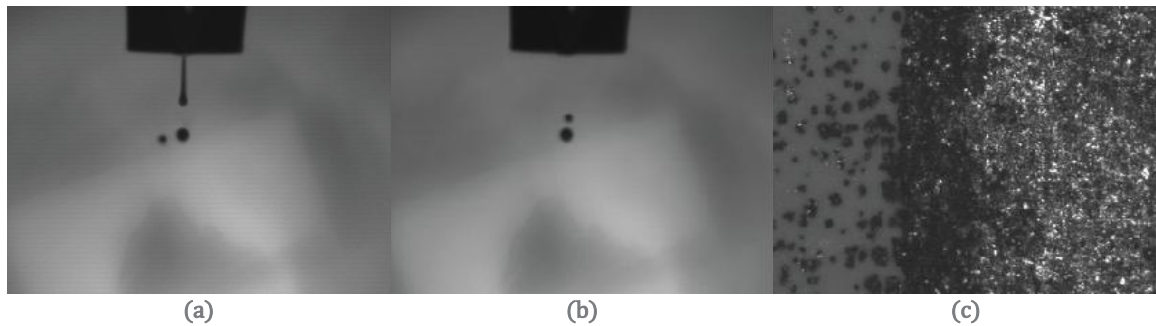


Figure 9: Poor Ink Droplet Formation

Once a good droplet is attained, several calibration structures are printed to test the capabilities of the printer. Figure 10 (top) shows a 10 x 10 array of individual droplets spaced 500  $\mu\text{m}$  apart. The droplets diameter on average is 100 $\mu\text{m}$ . Attempts to print multiple drops on top of each other to increase the conductivity causes the drops to widen.

The second calibration structure shown in Figure 10 (bottom) is a 5 x 5 array of 2 x 5 droplet rectangles. The droplets are spaced 50 $\mu\text{m}$  center to center, so there is an overlap. However, the average drop width on this run is 82 $\mu\text{m}$  as compared to 100 $\mu\text{m}$  in the previous case, though the

same parameters as the 10 x 10 array are used. This shows that the printing process lacks complete consistency.

A final calibration structure is a printed line shown in Figure 11. As shown, the line consists of an array of dots which are spaced 100um apart. The first few drops are out of line which is caused by a transient in the printing. Whenever the jet first starts, it takes several drops to reach a steady state printing condition. This causes several problems when it comes to printing structures that have disjoint features as the jet stops and starts while traveling between features.

Several attempts have been made at printing transmission lines and basic antennas but the large structures being printed (several centimeters in length) had too many difficulties with the nozzle clogging and disjoint features having transient edge effects. The printer worked well for smaller structures such as the calibration structures, but the large structures required much more tuning, experimentation with other inks that could help reduce clogging, and cleaning cycle abilities to keep the head free of debris during printing.

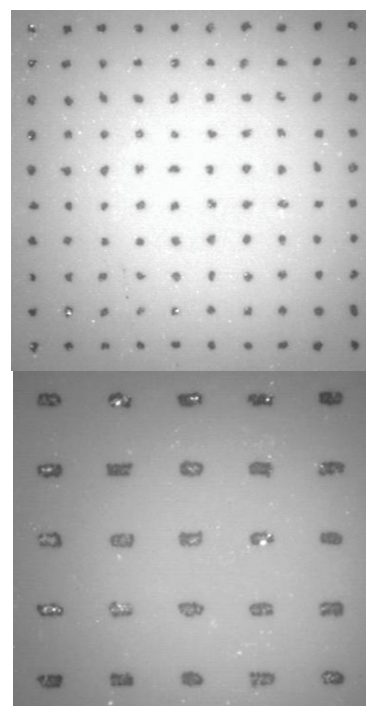


Figure 10: Calibration Structures

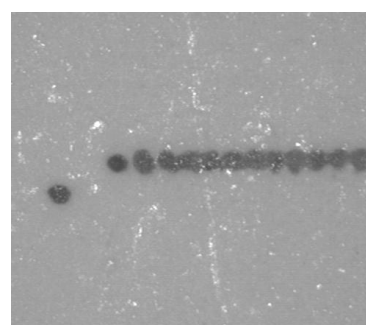


Figure 11: Transient Effects

### 3.1.2 Dimatix 2830 Printing

After attempts with the Microfab printer, the focus moved to the Dimatix 2830 – a printer that has shown promising results in several published inkjet-printed antennas [9], [8], [12]. The Dimatix printer has a 16 nozzle cartridge which is much closer to that of a traditional inkjet printer. Instead of filling a reservoir for each printing session, a cartridge is filled with the ink which could be removed and re-used between sessions. The nozzles are basically holes etched in a silicon substrate with a piezo actuator in each individual nozzle that expands to expel the droplet of ink. These nozzles require little to no adjustment to print properly as long as the same settings for ink temperature and waveform are retained. The print nozzle ejects 1 – 10 pL drops which are 50-60 times smaller than the drops from Microfab nozzles which decreases errors and increases precision. The printer is able to print with the nozzle much closer to the substrate which greatly decreases drop inconsistency, as drops ejected as satellites or on an angle have very little time to stray away from the center of the nozzle before hitting the substrate. Regular cleaning cycles remove the issue of nozzle clogging by cleaning the nozzles after every few minutes of printing. An image of four of the six jets working correctly is shown in Figure 12. Two of the nozzles – one on the far left and one second from the right – are clogged. Even though the nozzle on the right is working, it cannot be used in printing as only consecutive nozzles can be used. So in this case, the three next to each other in the middle are used to print. With a new cartridge, finding more than 5 consecutive nozzles working is difficult.



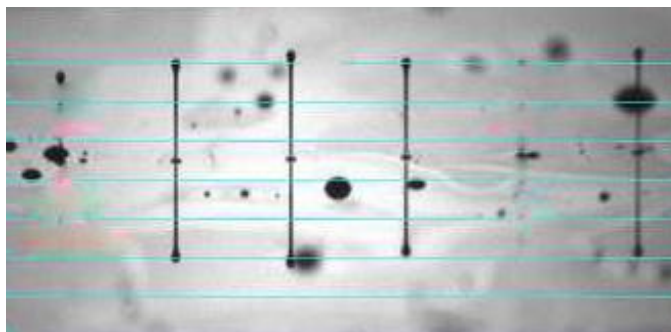


Figure 12: Dimatix Drop Watcher

The Dimatix printer has produced more reliable results than the Microfab printer with the similar printed structures. Figure 13 shows individual drops on paper from a 10pL cartridge along with a printed line using Cabot Silver Nanoparticle ink [31]. The diameter of the drops averages 43um, and the width of the line with 20um spacing between drops is about 60um. Notice there are little to no transient effects on these structures like seen in the Microfab printer which is attributed to closer nozzle spacing to the substrate and in-print cleaning cycles.

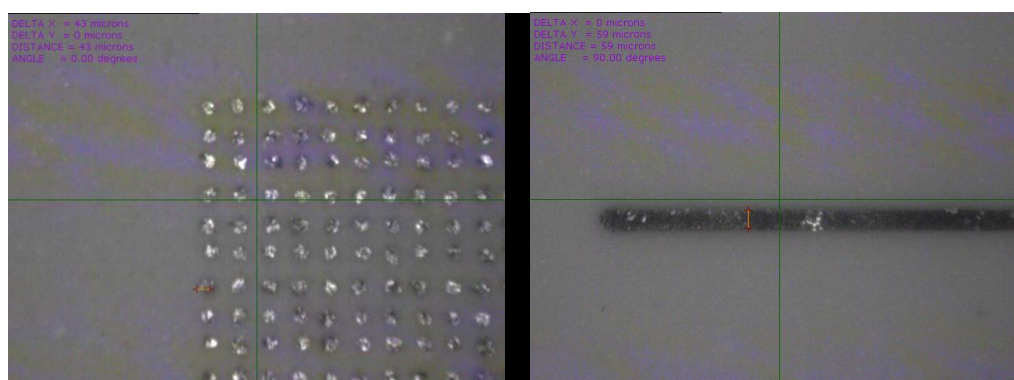


Figure 13: Dimatix 10pL Calibration Structures

An array of droplets using the 1pL cartridge is shown in Figure 14. It can be seen that the drop sizes are nearly half the diameter of the 10pL cartridge allowing for much better features to be attained.



Figure 14: Dimatix 1pL Calibration Structures

Several test structures with gaps are printed to test the minimum spacing that can be achieved with the

10 pL cartridge. Figure 15 shows a 50 and 100um gap as specified in the layout of the design. Notice that due to spreading of the drops, the gaps are 30, and 64um respectively, which can then be used to adjust the printing parameters to match the input design. The edge roughness is on the order of 10um.

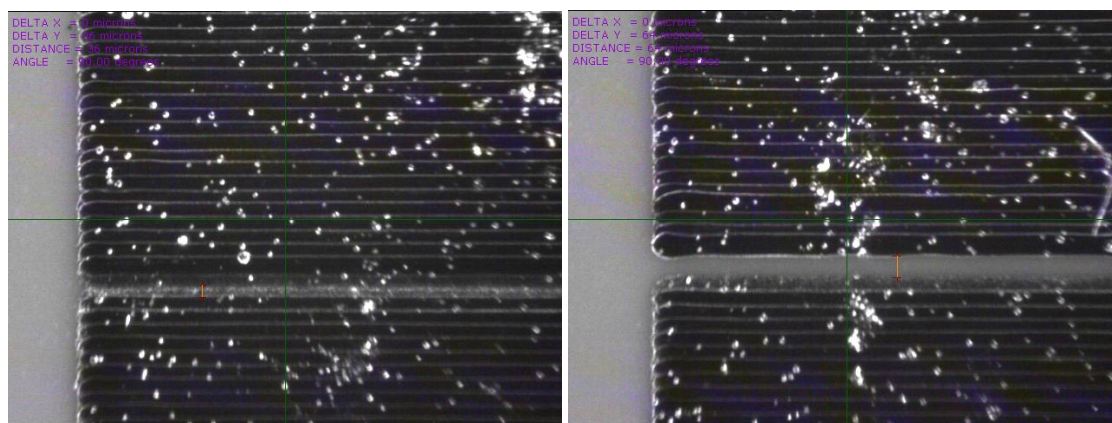


Figure 15: Minimum Spacing Pattern

Gaps of less than 30um are very difficult to achieve with the 10pL cartridge as ink bleeding between the two structures becomes an issue. Smaller gaps down to 10um can be attained by using a 1pL drop, but the sizes of the antennas printed for this

thesis do not require such small gaps and therefore the characterization will be limited to the 10pL cartridge.

### 3.1.3 Printer Comparison

Two printers have been discussed, and the Dimatix is chosen as the printer to be used for the inkjet-printed antennas, since it is more suited to large structure printing and has the capabilities to produce smaller features. A comparison of the two printers is presented in Table 3. As shown, the Dimatix has clear advantages due to smaller drop size leading to better feature definition, more nozzles, in-process nozzle cleaning to prevent clogging, and closer nozzle positioning to the substrate to allow for better drop precision.

Table 3: Printer Comparison Chart

	<b>Dimatix 2800</b>	<b>Microfab Jetlab II</b>
<b>Drop Volume</b>	1-10 pL	50-60 pL
<b>Minimum Feature</b>	28 um	80 um
<b>Minimum Spacing</b>	30 um	Not Reliable
<b>Number of Nozzles</b>	16	1
<b>Cleaning During Printing</b>	Yes, Automatic	No, Manual
<b>Nozzle Minimum Height</b>	0 um	1 mm

### **3.1.4 Conductivity**

Conductivity of printed silver nanoparticles is one of the major issues encountered with inkjet printing. When silver nanoparticles are deposited on the substrate, they form an agglomeration of silver particles 10-50nm in size. The structure at this point is not conductive as the particles are not a continuous body – similar to a metal trace with millions of hairline fractures that prevent electron flow. It is required to melt the particles together in order to achieve conductivities high enough to produce efficient antennas. Several methods have been used in the literature including heat sintering, laser sintering, and UV and microwave exposure. Along with sintering methods, several other variables play a role in the final conductivity of the printed structures, such as:

- Number of ink layers printed
- Surface roughness of the substrate
- Ink properties (viscosity, metal concentration by weight, surface tension)

The following sub-section provides a detailed study into heat and laser sintering of silver nanoparticle inks on polymer and organic substrates to determine the best methods of achieving highly conductive structures while reducing cost and fabrication time.

#### **3.1.4.1 Heat Sintering**

Heat sintering is one of the most common methods of annealing or melting nanoparticle inks to form continuous conducting structures. Metallic nanoparticles

exhibit a unique property in which their small size decreases their melting point to temperatures as low as 80°C which is important when printing on substrates such as paper and plastic which cannot handle high temperatures. A series of conductivity tests are performed using photo paper and PET as substrates using Cabot Silver Nanoparticle ink [31] and UTDots Silver Nanoparticle ink [30]. To test conductivity, a series of traces are printed on both substrates using 1 – 5 layers of ink. The substrates are then placed in an oven in air at atmospheric pressure using different times and temperatures for curing. The resistance of the traces is then measured using the four point method on a Cascade probing station. Figure 16 shows the sheet resistance of the traces for 1 – 5 layers of ink on paper at temperatures of 100 – 200°C for one hour. An important note is that all structures printed in this section use a 10pL cartridge with 20um drop spacing. It can be seen, as sintering temperature and number of ink layers printed increases, conductivity increases as well. The higher temperatures increase conductivity by burning off more of the polymer coating that is used as a dispersant coating and melting the particles together. Printing more layers helps by increasing the density of particles in a given area so that when melted together, the nanoparticles form less of a porous and more of a uniformly solid structure.

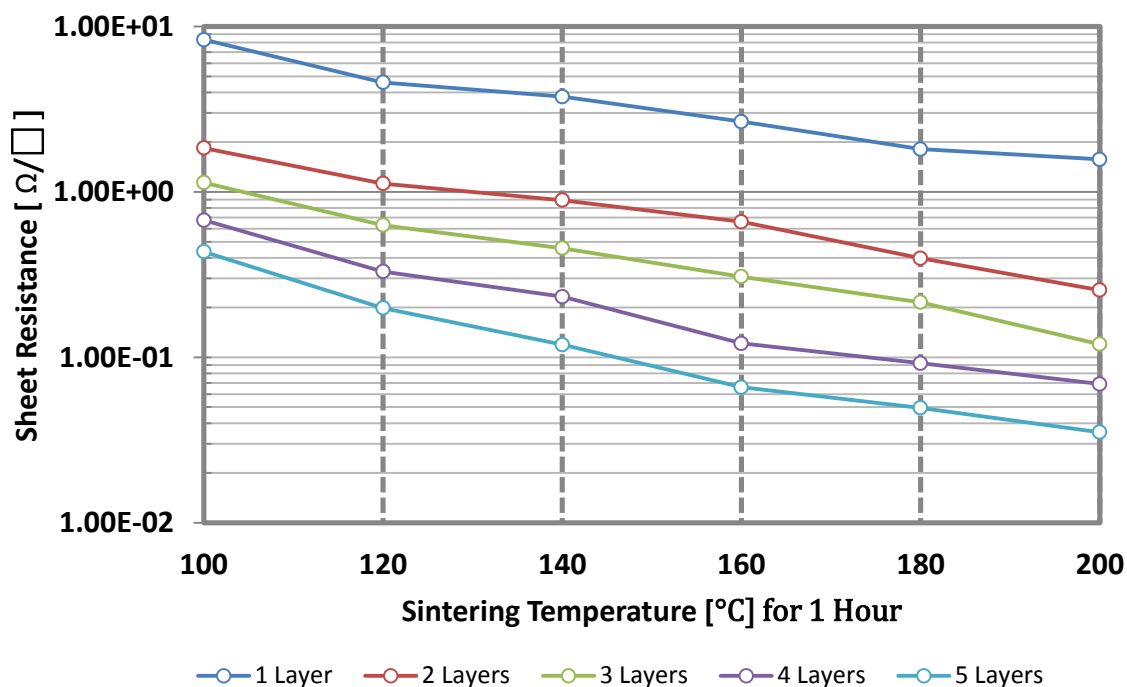


Figure 16: Sheet Resistance Vs. Temperature for Cabot Ink

Figure 17 shows a comparison of sheet resistance between 5 layers of UTDots and 5 layers of Cabot ink on paper versus temperature. As shown, the inks exhibit very similar properties in temperature curing except at lower temperature which is due to a different polymer coating used as a dispersant on the silver nanoparticles, and different mean particle sizes. A second study was run using sintering time as the independent variable to determine the shortest times allowed to obtain highly conductive structures using Cabot ink on paper. Figure 18 shows the results of sintering over time at 120 and 200°C.

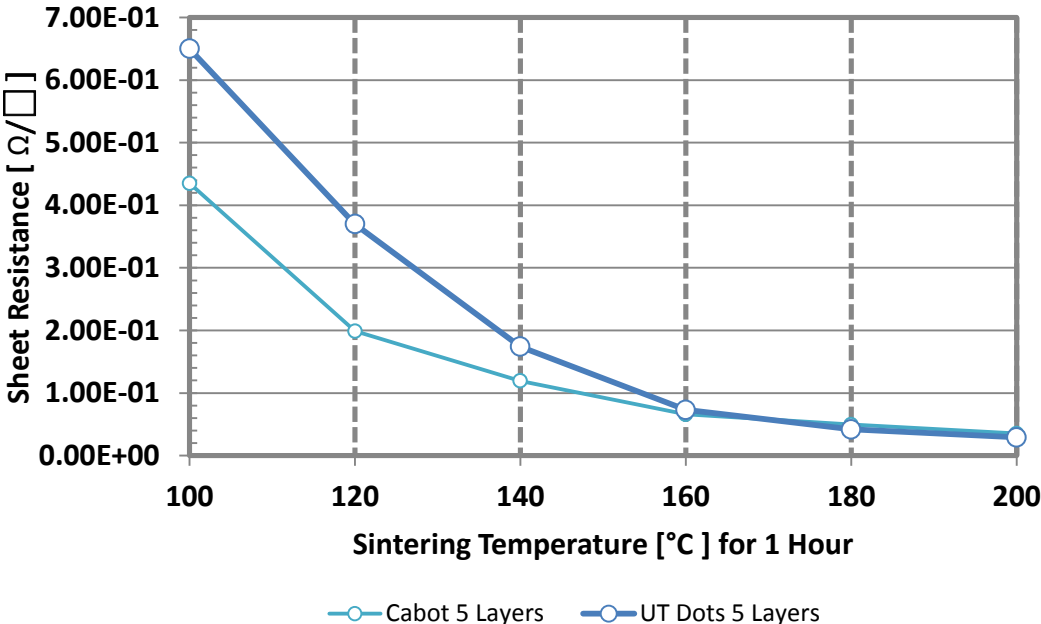


Figure 17: Cabot Vs. UT Dots Sheet Resistance Vs. Temperature

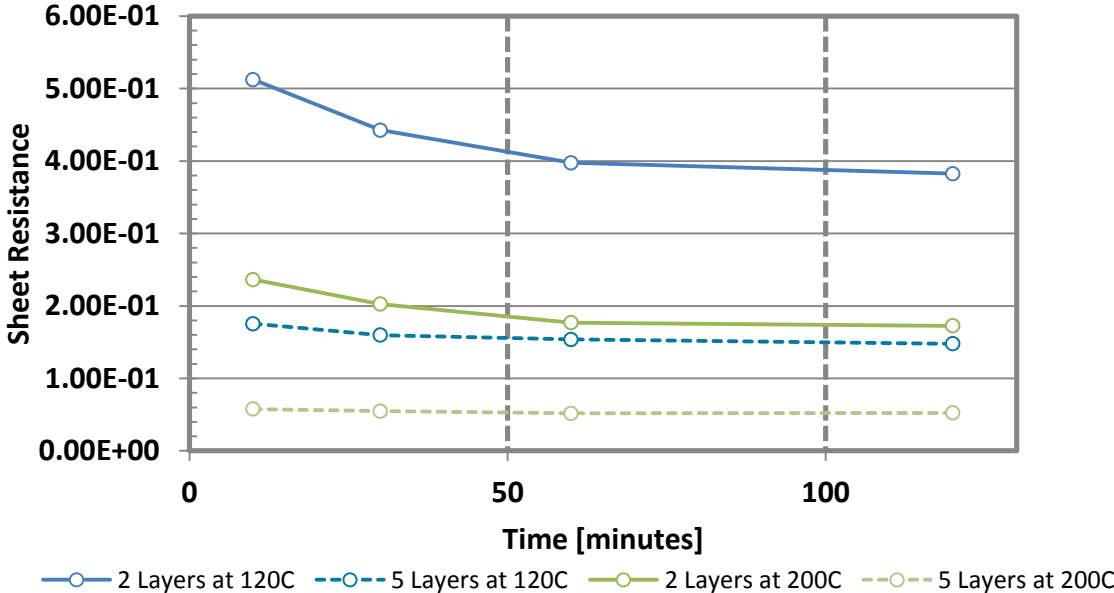


Figure 18: Cabot Ink Sheet Resistance Vs. Time

As seen, sintering at higher temperatures greatly decreases the amount of time required to reach the final conductivity values achievable at that temperature, as well as dramatically increasing overall conductivity. The tradeoff is that substrates such as PET have glass transition temperatures near 120°C, and therefore must not be processed at these temperatures as warping and deformation will occur.

In order to extract the conductivity from the sheet resistance, the layer thicknesses are needed. As the surface roughness on polymer and organic substrates is higher than the thickness of the conductors, 1-5 layers of ink were printed on glass which has a smooth surface, and then are sintered at 200°C for 1 hour. The traces were then measured using a Dekktak profilometer. The results are as shown in Figure 19.

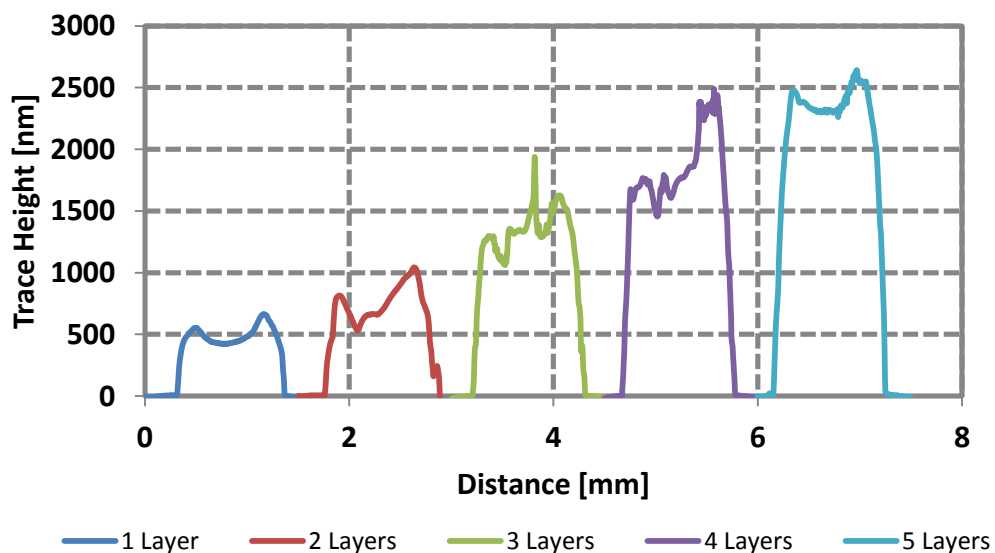


Figure 19: Thickness of Printed Cabot Ink Layers on Glass

From the above figure, it is seen that each layer adds approximately 500nm of thickness to the structure. Using the area of the traces along with their resistance



yields the conductivity of the sintered nanoparticle inks which will be discussed in a following section.

### 3.1.4.2 Laser Sintering

One of the main issues with heat sintering is that many plastic and organic substrates cannot handle the high heats required to melt nanoparticles together. For example,



Figure 20: Paper 120C (Left) 200C (Right)

a sheet of paper sintered at 200°C is shown in Figure 20, and it can be seen that the paper has started to burn. This is where laser sintering has a huge advantage. With laser sintering which is shown in Figure 21, a laser is passed over the deposited nanoparticles, and heats the particles with very little heating of the substrate. The majority of the heat is absorbed by the particles themselves and does not penetrate to the substrate if the laser power is held low enough.

A study of sheet resistance versus laser power is performed using the same inkjet-printed structures as the heat sintering study, and the results of laser sintering versus heat sintering are reported. As shown in Figure 22, laser sintering achieves sheet resistances as low as heat sintering at 200°C with lower powers and

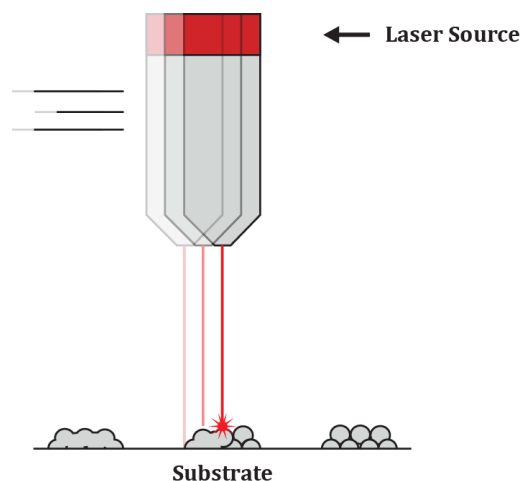


Figure 21: Laser Sintering

much quicker times. The laser achieves the same sheet resistance in 10 – 20

seconds that requires one hour in an oven at 200°C, and, the substrate remains in an unaltered state. The one issue is alignment of the laser with the printed pattern, but this can be taken care of with printed alignment marks and careful alignment.

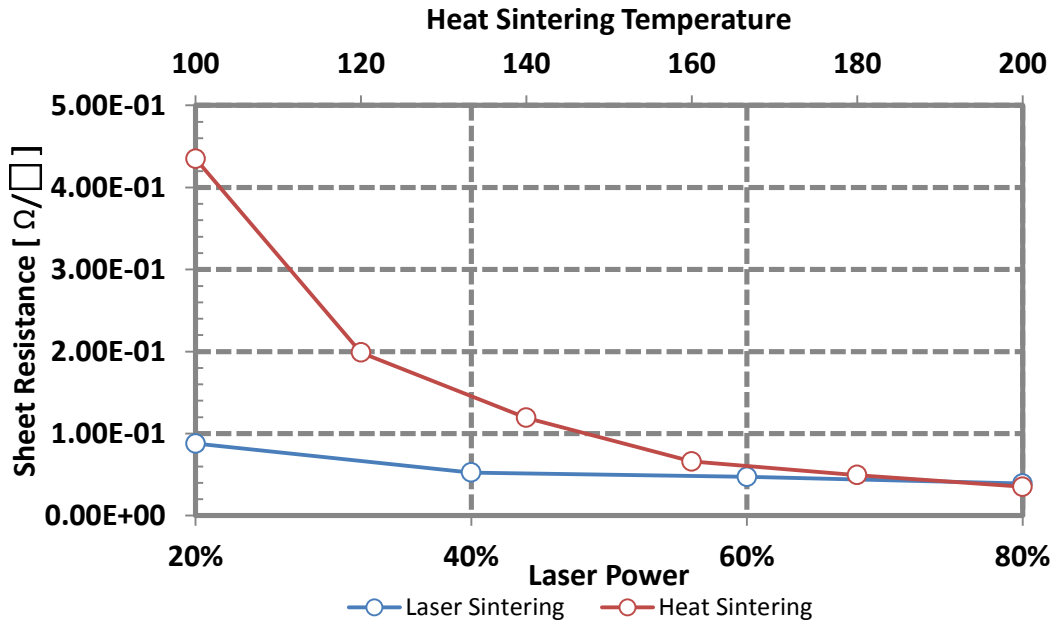


Figure 22: Laser Vs. Heat Sintering for 5 Layers of Cabot Ink

### 3.1.4.3 Conductivity Summary

In this section, the conductivity of printed test structures is characterized over several variables of the inkjet-printing process including layers printed, sintering time, temperature, and laser sintering. The thickness of the structures is also tested using a profilometer with traces printed on a smooth glass surface in order to relate sheet resistance to conductivity ( $\sigma$ ) using the following equation:

$$\sigma = \frac{\int(\text{trace height})dx}{\text{Sheet Resistance}} \quad (1)$$

The following table contains the estimated conductivities for the previously tested structures. The conductivities for sintering at 120 and 200°C are very similar to published values in [32].

Table 4: Inkjet Ink Conductivities

# Layers	Sintering - 120°C	Sintering - 200°C	Laser
1	5.45e5	1.6e6	-
2	1.11e6	4.9e6	-
3	1.16e6	5.56e6	-
4	1.52e6	1.3e6	-
5	2.1e6	1.2e7	1.1e7
<b>Published</b>	3e5 (1 layer)	3e6 (1 layer)	

As seen in the table, using the correct sintering parameters can lead to conductivities above  $1e7$  which is only five times lower than bulk silver at  $6.4e7$  S/m. Introducing more printed layers, or sintering at higher temperatures can bring inks even closer to bulk silver conductivities, but at an increased cost. The results from this section prove that silver nanoparticle inks are suitable for implementing microwave frequency structures and antennas.

### 3.2 Substrate Characterization

The lack of available substrate characterization data on polymer and organic substrates is a major obstacle in using them for the fabrication of microwave structures. Since these are not common microwave substrates, the first issue is that manufacturers have not put in the effort to characterize them for electrical permittivity ( $\epsilon_r$ ) and loss tangent ( $\tan\delta$ ) past low MHz frequencies, and for some substrates such as photo paper, the electrical properties are not provided at all. The second issue is that most polymer and organic substrates have widely varying parameters based on manufacturer processing techniques, batch quality, substrate thickness, and other factors. For example, Dupont publishes the relative permittivity of Kapton at 1kHz, and the values of permittivity range between 2.8 and 3.8 depending on a variety of factors [33]. Therefore, whenever using a new flexible substrate such as paper, Kapton, PET, or others, the electrical properties must be characterized.

Several methods have previously been used to characterize microwave substrates ranging from resonant cavities, transmission line resonators, and group velocity measurements of microstrip and co-planar waveguide structures [34]. Following sections in this chapter elaborate on the methods used to measure the relative permittivity of Photo Paper, PET, and Kapton. This data is essential for the design of antennas on these substrates.

### 3.2.1 Ring Resonator Technique

One of the most common substrate characterization methods is to use a two-port microstrip ring resonator to extract the permittivity and loss tangent of a substrate. A ring resonator is shown in Figure 23 where  $l$  is the microstrip feed length,  $G$  is the capacitive coupling gap between feed line and ring,  $C$  is the circumference of the ring, and  $W$  is the width of the microstrip line. The ring resonates whenever the circumference is equal to one wavelength or multiples of one wavelength [35]. This is expressed in (2).

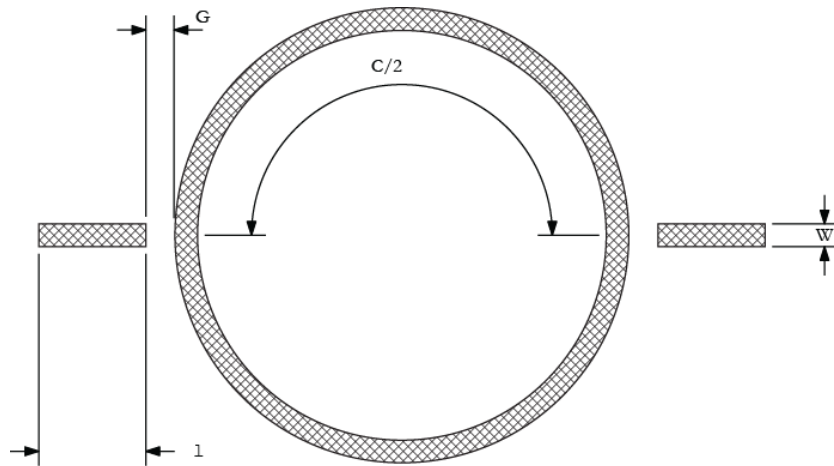


Figure 23: Ring Resonator

$$n\lambda_g = 2\pi r \quad (2)$$

From the resonant frequencies, the relative permittivity can be extracted using the geometry of the microstrip lines, and the circumference of the ring. The velocity of propagation,  $V_p$  in a microstrip line is well known through (3), where  $\epsilon_{eff}$  is the effective permittivity due to inhomogeneous dielectric common to the microstrip structure [36]:

$$V_p(f) = \frac{c}{\sqrt{\varepsilon_{eff}(f)}} \quad (3)$$

And, relating the velocity of propagation to the wavelength we get:

$$\lambda_g(f) = \frac{c}{f\sqrt{\varepsilon_{eff}(f)}} \quad (4)$$

From these equations  $\varepsilon_{eff}(f)$  can be calculated. Since the fields in a microstrip line are quasi-TEM due to the inhomogeneous dielectric of microstrip structure, the relative permittivity of the substrate becomes a function of the permittivity of the substrate and the geometry of the microstrip line shown in Figure 24 along with the equation to extract the relative permittivity.

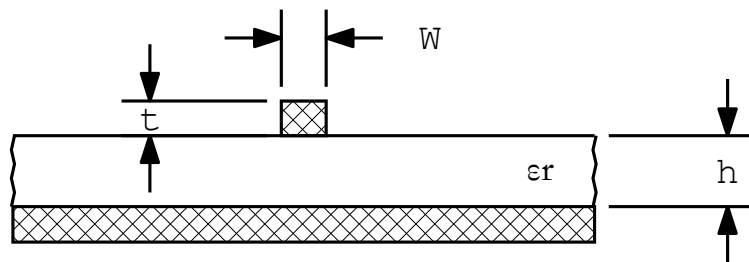


Figure 24: Microstrip Structure

$$\varepsilon_{eff}(f) = \begin{cases} \frac{\varepsilon_r(f) + 1}{2} \left[ 1 - \frac{1}{2H'} \left( \frac{\varepsilon_r(f) - 1}{\varepsilon_r(f) + 1} \right) \left( \ln \frac{\pi}{2} + \frac{1}{\varepsilon_r(f)} \ln \frac{4}{\pi} \right) \right]^{-2} & \frac{w}{h} < 1.3 \\ \frac{\varepsilon_r(f) + 1}{2} + \frac{\varepsilon_r(f) - 1}{2} \left( 1 + 10 \frac{h}{w} \right)^{-0.555} & \frac{w}{h} < 1.3 \end{cases} \quad (5)$$

Where:

$$H' = \ln \left( 4 \frac{h}{w} + \sqrt{16 \left( \frac{h}{w} \right)^2 + 2} \right) \quad (6)$$

Once the relative permittivity versus frequency is extracted, the quality factor  $Q$  of the each of the resonance peaks denoted by  $n = (1, 3, 5, \dots)$  can be used to extract the total losses  $\alpha_{tot}$  in the resonator which are composed of conductor  $\alpha_c$ , dielectric  $\alpha_d$ , and radiation losses respectively  $\alpha_r$  [35].

$$\alpha_{tot,n} = \alpha_{c,n} + \alpha_{d,n} + \alpha_{r,n} = \frac{8.686\pi f_r \sqrt{\varepsilon_{eff}}}{cQ} \left[ \frac{dB}{length\ unit} \right] \quad (7)$$

The conductor ( $\alpha_c$ ) and radiation ( $\alpha_r$ ) losses can be extracted with a series of empirical formulas or simulators and removed from the total loss which leaves only the dielectric loss. In this work, Agilent's line-calc program is used to extract the conductor and radiation losses. With the conductor and radiation losses removed from the total loss, (8) can be used to relate the dielectric loss to loss tangent [35].

$$\tan \delta = \frac{\alpha_{d,n} \lambda_o \sqrt{\varepsilon_{eff,n}} (\varepsilon_{r,n} - 1)}{8.686\pi \varepsilon_{r,n} (\varepsilon_{eff,n} + 1)} \left[ \frac{dB}{length\ unit} \right] \quad (8)$$

As characterization work began before the ink-jetting process had been characterized, a shadow masked sputtering process is used to fabricate the ring resonator on a PET substrate.

To fabricate a prototype ring resonator for testing, sputtered gold was used on PET and Kapton with a laser cut shadow mask. The ring resonator is shown in Figure 25. Due to the limitations on sputtering thickness (1 $\mu\text{m}$ ), and large minimum gap size (100 $\mu\text{m}$ ) was required.

This large gap reduced coupling to the ring, and

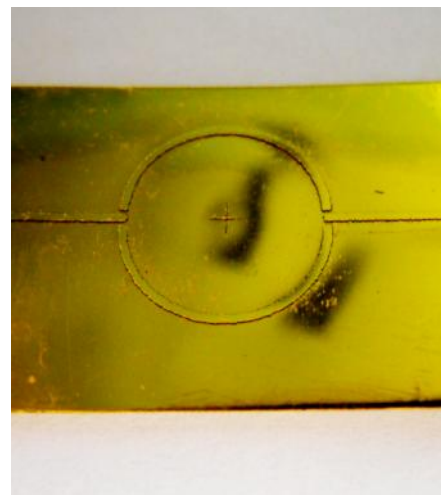


Figure 25: Fabricated PET Ring Resonator

hence the insertion loss of the resonator was near the noise floor which made dielectric loss tangent extraction impossible. The return loss of the resonator is shown in Figure 26, which is used to extract the permittivity of the PET. While the results are in the range of published PET values, the loss tangent was not able to be extracted due to the lack of coupling from large gap sizes required by the sputtering process.



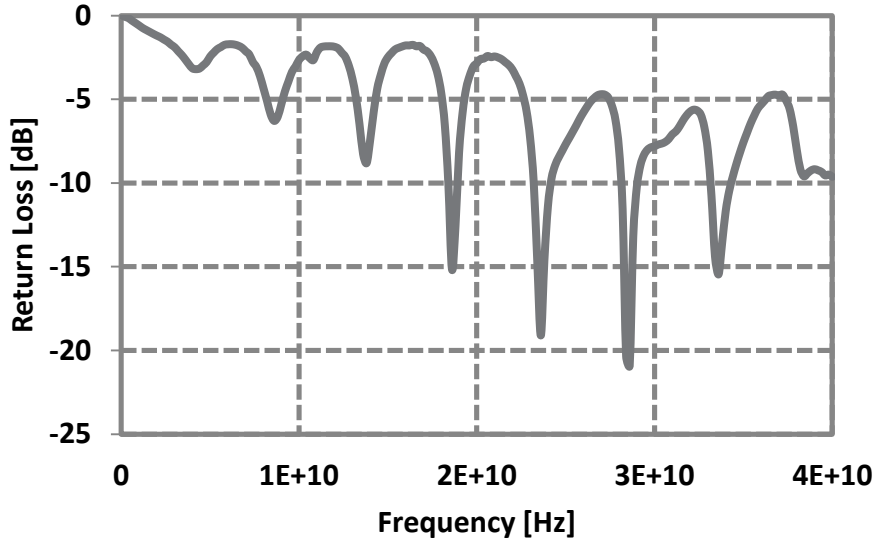


Figure 26: PET Ring Resonator Return Loss

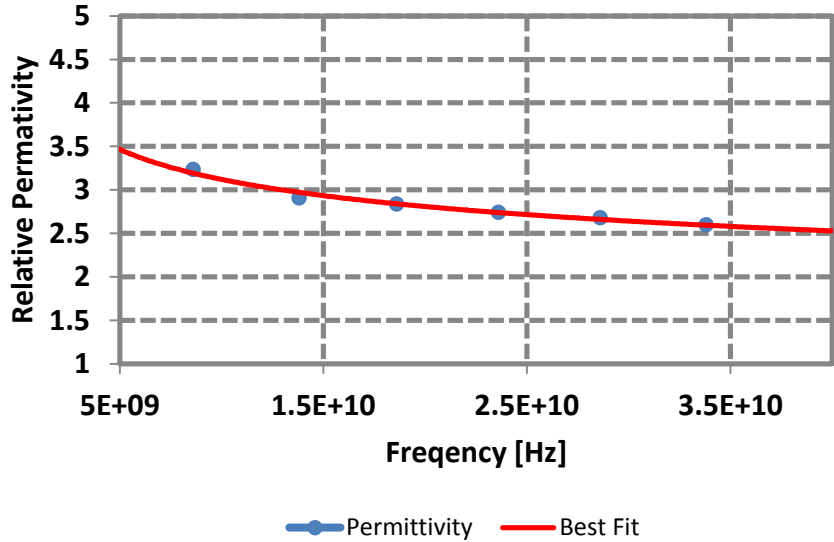


Figure 27: PET Ring Resonator Permittivity

Due to the poor results of the sputtering process, and a lack of other processes in our lab to fabricate ring resonators with small gaps on PET, Kapton, or Paper, it was decided to move on to another type of resonator that would be easier to fabricate – the microstrip T-Resonator

### 3.2.2 T-Resonator Technique

The T-Resonator, while not as common as the ring resonator in characterization, is much simpler to fabricate as it consists of a microstrip transmission line with an open circuit stub. The structure of the T-Resonator is shown in Figure 28. Due to the open circuit stub with length  $d$ , a null occurs in the transmission whenever  $d$  is an odd multiple of a quarter wavelength [37] which is caused by the reflected wave being  $180^\circ$  out of phase once it returns from the open end of the stub.

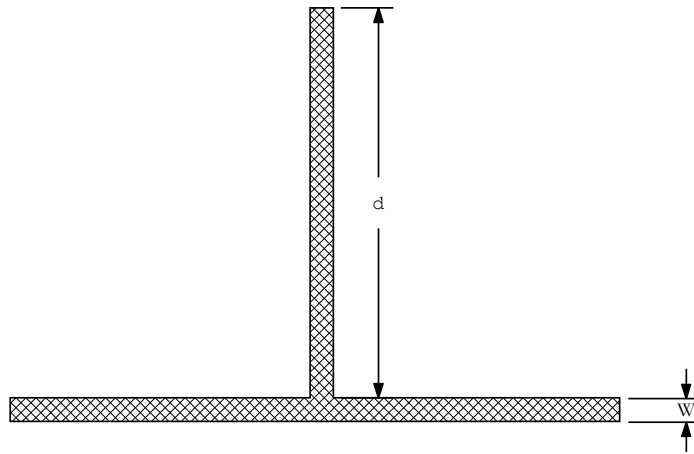


Figure 28: Microstrip T-Resonator

$$f_{r,n} = \frac{nc}{4L\sqrt{\epsilon_{eff}}} \quad (9)$$

The equation for resonance is shown in (9) where  $n$  is the resonance index (1, 3, 5, ...),  $c$  is the speed of light in vacuum,  $L$  is the length of the open circuit stub, and  $\epsilon_{eff}$

is the effective permittivity of the microstrip line [37]. However, due to the parasitics of the T-junction and fringing fields at the end of the open circuit stub, a correction factor for the length of the stub needs to be incorporated when calculating  $\epsilon_{eff}$ . A method for doing this is presented in [37]. Shown in (10),  $k$  is the correction factor which includes the junction and open circuit effects on the resonant frequency.

$$\epsilon_{eff,n} = \frac{nc}{4(d+k)f_{r,n}} \quad (10)$$

Using the relations of relative to effective permittivity in a microstrip (5) – (6) in section 3.2.1, the permittivity of the substrate can be extracted.

The Q-factor of the resonance peaks can be used to extract the loss tangent of the substrate. The loaded Q-factor is calculated in (11), and then needs to be converted to the unloaded Q-factor (12). which de-embeds the loading caused by the measurement equipment [37].

$$Q_{l-n} = \frac{f_{r,n}}{BW_{3dB-n}} \quad (11)$$

$$Q_{ul-n} = \frac{Q_{l-n}}{\sqrt{1 - 2 \cdot 10^{La/10}}} \quad (12)$$

In (11),  $Q_{l-n}$  is the Q-factor for the  $n^{\text{th}}$  resonance,  $f_{r,n}$  is the resonant frequency, and  $BW_{3dB-n}$  is the 3-dB bandwidth. In (12),  $La$  is the insertion loss at resonance which is

used to de-embed the loading effects. The total losses in the microstrip resonator (13) can then be extracted [38].

$$\alpha_{tot,n} = \alpha_{c,n} + \alpha_{d,n} + \alpha_{r,n} = \frac{8.686\pi f_{r,n} \sqrt{\epsilon_{eff,n}}}{cQ_{ul-n}} \left[ \frac{dB}{length\ unit} \right] \quad (13)$$

There are a variety of methods to extract conductor and radiation losses, however in this work, Agilent's Line-calc utility is used to subtract these two losses from the total loss leaving only the dielectric losses. The dielectric loss can be directly converted to loss tangent through (14) using standard microstrip loss equations given in [34].

$$\tan\delta = \frac{\alpha_{d,n} \lambda_o \sqrt{\epsilon_{eff,n}} (\epsilon_{r,n} - 1)}{8.686\pi \epsilon_{r,n} (\epsilon_{eff,n} + 1)} \quad (14)$$

To fabricate the T-Resonators, the same sputtering process which was used in the previous section was used for Kapton and PET. However, paper had heating and degradation issues when used in the high vacuum sputtering process, so inkjet printing was used to fabricate the paper based resonator instead as at this time the process had been characterized.

One of the issues that arose with Kapton and PET was that the substrates were very thin which required thin transmission lines for the T-Resonator to have a characteristic impedance near 50Ω. This leads to high conductor losses in the resonator. The lower the conductor loss, the better the interference by the open circuit stub, and the easier it is to distinguish resonant peaks. Paper can be heat

bonded together to form a thicker layer which means wider transmission lines and less conductor loss. The substrate dimensions and corresponding microstrip width are shown in Table 5.

Table 5: Resonator Dimensions

Material	Thickness (in)	Thickness ( $\mu\text{m}$ )	Microstrip Width (mm)	Stub Length d (mm)
Photo Paper	0.062	230	1.05	48
Polyethylene	0.007	177.8	0.40	48
Kapton HN	0.005	127.0	0.28	45

The paper-based T-Resonator is shown in Figure 29 along with the TRL calibration lines. The stub was designed to have resonances at odd intervals of 1 GHz (1, 3, 5 ...), with the intent of measuring the permittivity and loss tangent up to 10 GHz. While more frequency points would have been better, a lower resonant frequency would require a longer stub which is more difficult to fabricate and can cause more uncertainty in extracting conductor loss. The measured insertion loss is shown in Figure 30.



Figure 29: Microstrip T-Resonator

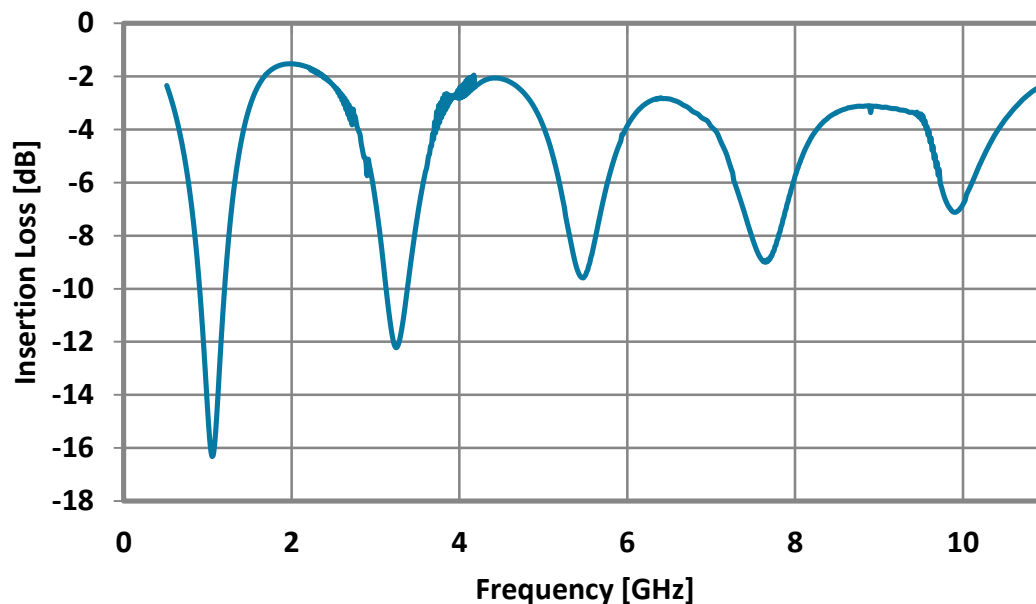


Figure 30: Paper T-Resonator Insertion Loss

Using the aforementioned technique of extracting substrate permittivity, Figure 31 was attained which shows the relative permittivity vs. frequency. The data has been compared to the results in (reference) and shows good agreement at the measured frequencies. Dispersion is relatively high over the frequency range, but this can be expected as paper is an organic substrate and has not been tailored for microwave use.

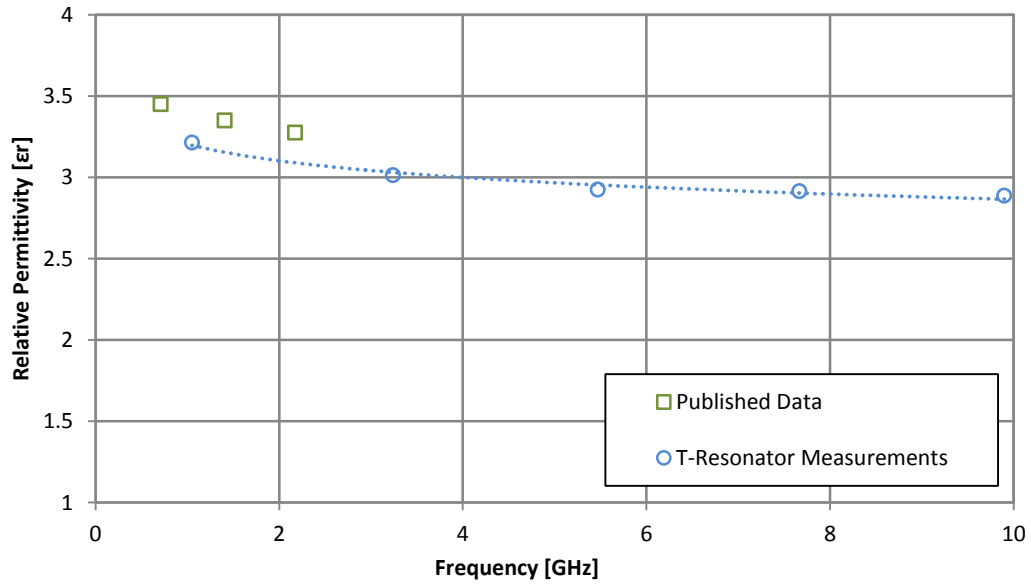


Figure 31: Extracted Relative Permittivity of Photo Paper

Following the extraction of the relative permittivity, the extraction of the loss tangent was performed which is shown in Figure 32. The loss tangent is within reasonable range to previously published data which leads us to believe our extraction was accurate.

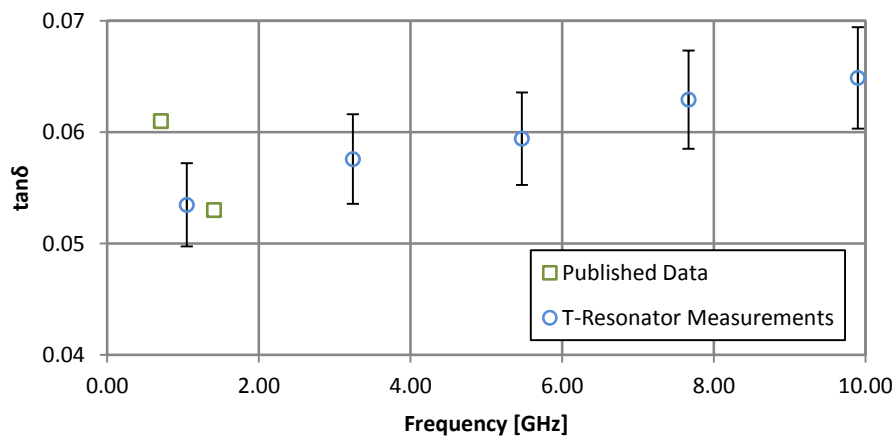


Figure 32: Extracted Loss Tangent of Photo Paper

The Kapton and PET resonators both had very high edge roughness due to the shadow masking process used with sputtering which made it very difficult to accurately model conductor loss and therefore loss tangent extraction was not performed on these substrates. However, the relative permittivity was extracted for both materials and is shown in Figure 34. A close up comparison of the fabricated microstrip lines showing the high edge roughness with sputtering and low roughness in inkjet printing is shown in Figure 33.

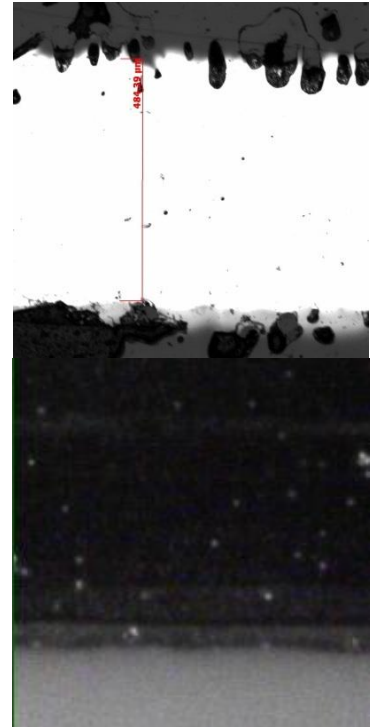


Figure 33: Top – Sputtered Line, Bottom - Printed Line

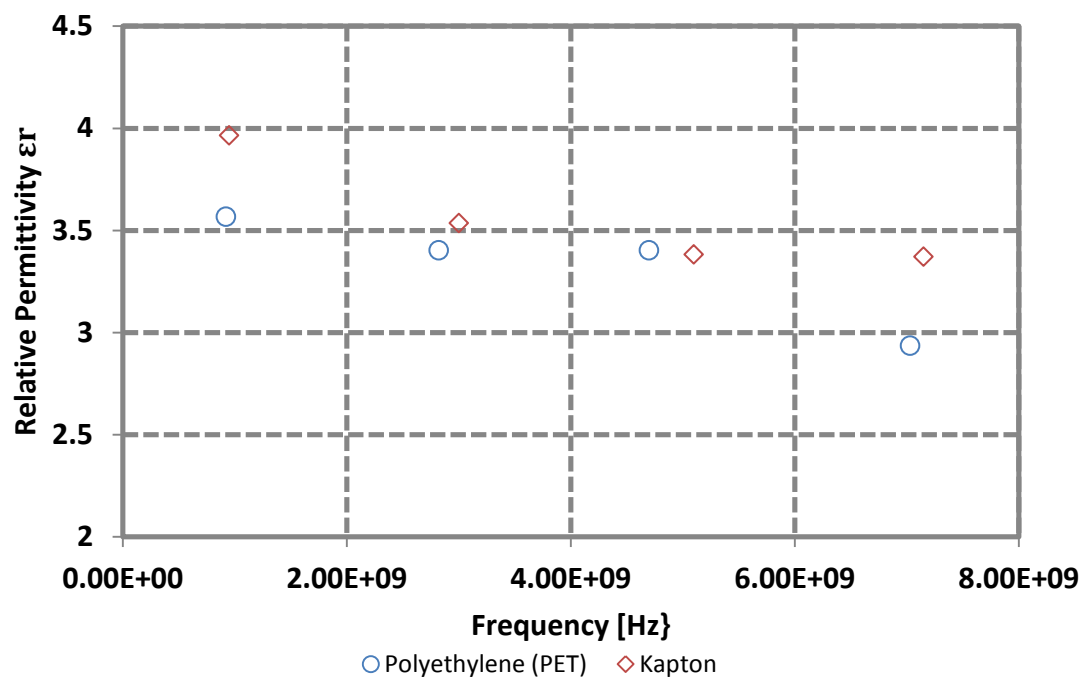


Figure 34: Extracted Permittivity of Kapton and PET



### 3.2.3 Transmission Line Method

One of the drawbacks of the T-Resonator method for extracting the loss tangent is that extracting conductor losses from a nanoparticle ink on a porous material such as paper is very difficult due to variable surface roughness. Therefore, a transmission line method is used as well to extract the dielectric losses on paper in

which the transmission line is fabricated from laser-cut aluminum foil which allows for easy conductor loss extraction.

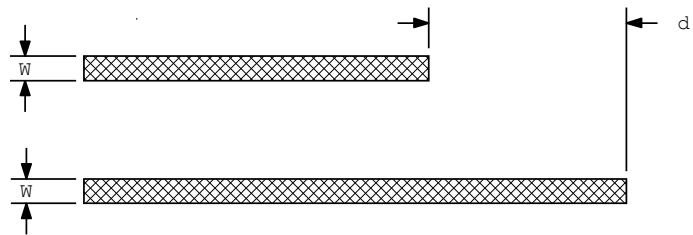


Figure 35: Transmission Line Loss Tangent Extraction

The laser cut lines have a

known thickness and conductivity as well as known edge roughness which the inkjet and sputtering processes do not have.

In this method, the insertion loss for two different lengths of transmission line is measured which is shown in Figure 36. The difference in insertion loss between the two lines is then divided by the difference in length  $d$  which de-embeds the end effects of the connectors. This total loss per unit length is again the combination of conductor, radiated, and dielectric losses from (13). Using the same methods described in 3.2.2, the dielectric loss is isolated from the total loss of the transmission line. From the dielectric loss, the loss tangent is extracted using (14). A smoothing function was used on the data to reduce noise. The loss tangent is then compared with the published and T-Resonator data in Figure 37. As seen, the loss tangent data from the transmission line method is in proximity to the loss from the T-

Resonator. This confirms that the loss tangent is near 0.05 over the UWB frequency band.

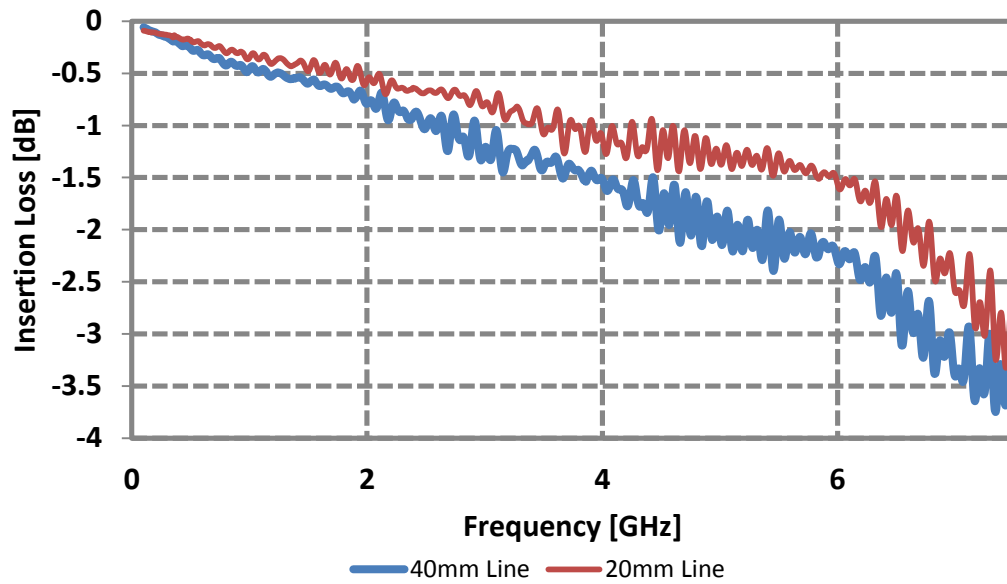


Figure 36: Insertion Loss of Two Lengths of Transmission Line

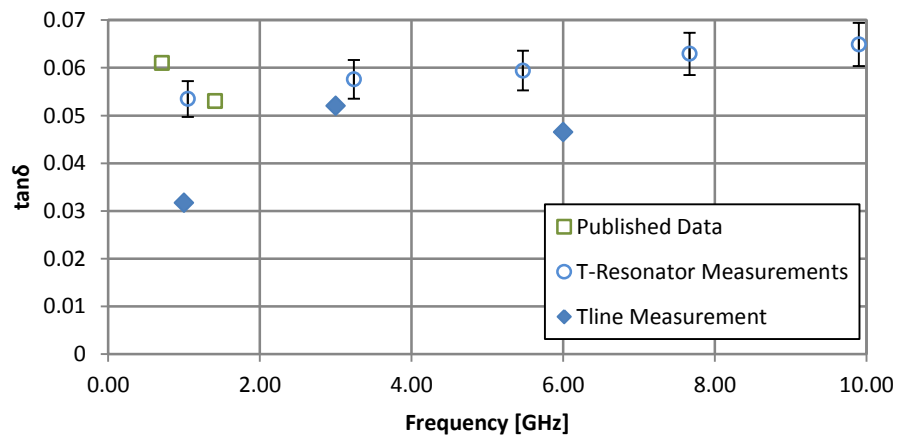


Figure 37: Loss Tangent Comparison Between Methods

### **3.3 Summary**

As demonstrated in this chapter, the characterization of the inkjet printing process is performed and several techniques were used to investigate the electrical parameters of Paper, Kapton, and Polyethylene. The measured electrical properties are close to published data in the frequencies where data has been published on these substrates. While these substrates have high dispersion over the 1 – 8GHz frequency range, proper design can help to lessen the effects of dielectric loss. The inkjet-printing process has been tuned to produce conductivities near that of bulk metals, and feature sizes for structures and spacing of approximately 50um are able to be obtained. With the results of characterization, it is shown that high frequency antenna and microwave design using this process is realizable. The results of this section will allow for modeling and simulation of the antennas designed in the following chapters.

## 4. INKJET-PRINTED FRACTAL ANTENNAS

---

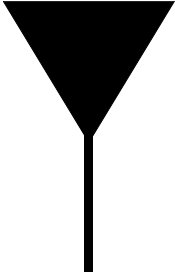
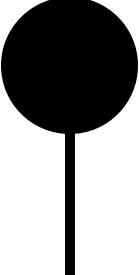

The characterization work in the previous chapter builds the foundation for designing antennas on polymer and organic substrates using the inkjet printing process. As stressed earlier, inkjet printing on polymer and organic substrates is important due to: low cost, light weight, disposability, environmental compatibility, and flexibility. And, due to the fact that paper is the cheapest and most promising substrate for these applications, it is the chosen substrate for all antennas fabricated in this thesis.

As discussed in Chapter 2, a major deficiency in the inkjet-printed antenna field is the lack of wideband and directive antennas. Using inkjet-printed antennas for wearable, high data rate, and energy harvesting applications requires expanding beyond the existing RFID antennas. These futuristic applications require antennas that have high gain and ultra-wideband performance. The work in this chapter blends the advantages of inkjet printing with wideband fractal antenna design to produce omnidirectional wideband antennas and prove that inkjet printing is an effective process for wearable and high data rate applications. The two antennas discussed in this chapter are the Serpinski fractal monopole antenna which is intended for 2.4GHz operation and an extension of the Serpinski monopole antenna to allow for ultra-wideband (3 – 10.6GHz) operation.

## 4.1 2.4 GHz Sierpinski Fractal Monopole

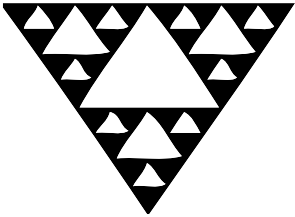
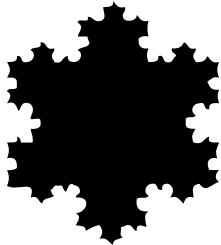
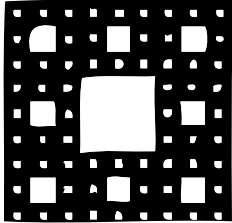
Wideband monopole antennas demonstrated in the literature [39], [40], [41], use a variety of shapes such as triangles and circles to better match the antenna and feed line (CPW, microstrip) impedances. Since inkjet printing is a planar process, it is very easy to feed antennas with microstrip or CPW lines and for this work, a microstrip-fed monopole is chosen. Some common microstrip-fed monopoles from literature are shown in Table 6.

Table 6: Wideband Monopole Types

		
Triangular Monopole [39]	Circular Monopole [40]	Square Monopole [41]

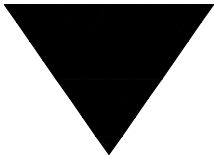
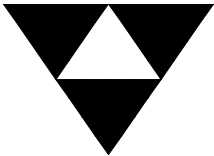
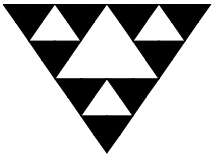
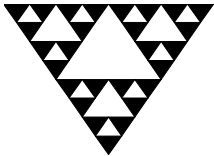
It has also been demonstrated that fractal patterns used in antenna design can decrease size while increasing the antenna's effective bandwidth [42]. Along with these benefits, fractals also have a unique benefit of decreasing cost in inkjet printing as fractal patterns decrease the amount of metallization required. The fact that fractal geometries require less ink and demonstrate superior wide bandwidth performance with smaller sizes makes them an attractive prospect for wideband, low cost antenna systems. Table 7 shows several fractal patterns that have been used in antenna design.

Table 7: Fractal Pattern Examples

		
Sierpinski Gasket	Koch Snowflake	Sierpinski Carpet

By looking at Tables 6 and 7, a good match is seen between the Sierpinski fractal and the triangular monopole, so the Sierpinski will be used to reduce ink consumption and increase the bandwidth of the triangular monopole. Table 8 shows the progression of the Sierpinski fractal along with the ink reduction achieved by increasing the number of iterations of the fractal pattern. By the third iteration, almost 60% reduction in ink is achieved. As ink is the primary cost in inkjet-printed antennas, using fractal geometry reduces the cost to almost half of the fully printed structure.

Table 8: Sierpinski Fractal Iterations

Iteration #	0	1	2	3
Fractal Progression				
Ink Reduction	0%	25%	43.75%	57.8%

#### 4.1.1 Sierpinski Monopole Design on Paper

The printed fractal monopole consists of a microstrip feed line, a tapered ground plane for increased wideband matching, and a Sierpinski Gasket radiating element which is shown in Figure 38. The width of the microstrip line is obtained by using the characterized  $\epsilon_r$  of photo paper which is 3.2 at

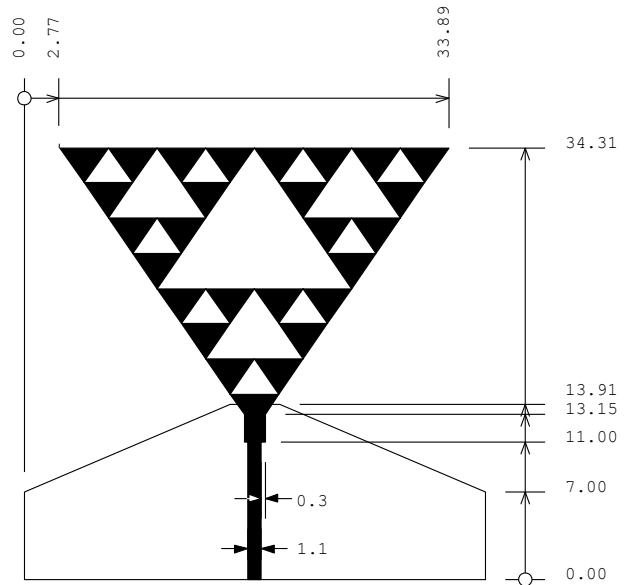
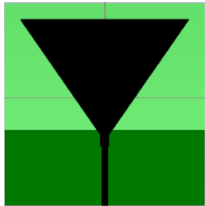
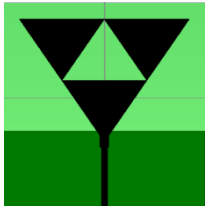
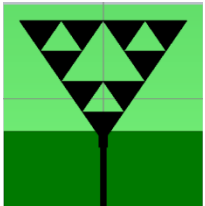
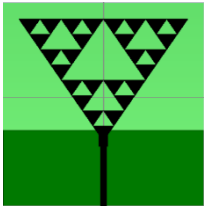


Figure 38: Microstrip T-Resonator (Units in mm)

2.4GHz, and a substrate thickness of 440um as inputs to CST's line calculation utility.

Several iterations of the Sierpinski Gasket monopole with a flat truncated ground plane are simulated to quantify the effects of adding the fractal pattern to the triangular monopole. The different iterations along with the resonant frequency are shown in Table 9. The return loss of the various iterations of the antenna is shown in Figure 39 which demonstrates the decrease in resonant frequency with the increase in the number of iterations of the fractal with equal antenna dimensions.

Table 9: Triangular Monopole with Sierpinski Progression

Iteration	0	1	2	3
CST Model				
$F_{\text{resonant}}$ [GHz]	2.65	2.55	2.49	2.44

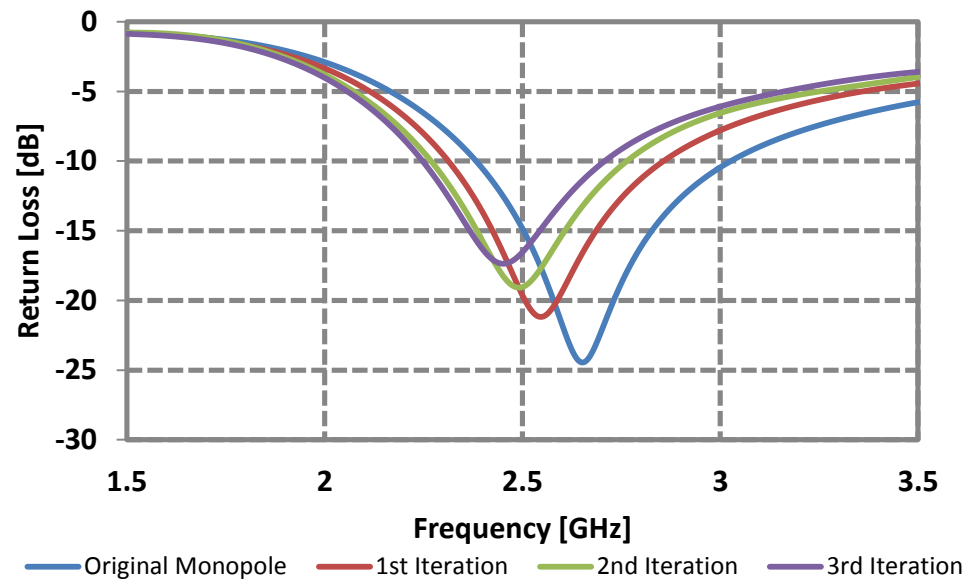


Figure 39: Return Loss for Fractal Iterations

As seen by the return loss progression, the matching worsens with increased fractal iterations. A technique commonly used in matching wideband antennas is to taper the ground plane [43], [44]. By tapering the ground plane which is shown in Figure 38, better matching is achieved as shown in Figure 40. It may also be noticed that the resonant frequency slightly decreases with the increased match. This is caused by an increased distance between the top edge of the Sierpinski Gasket radiating element and the bottom edge of the tapered ground. The steeper the taper, the larger this distance, and the lower the operating frequency will become.



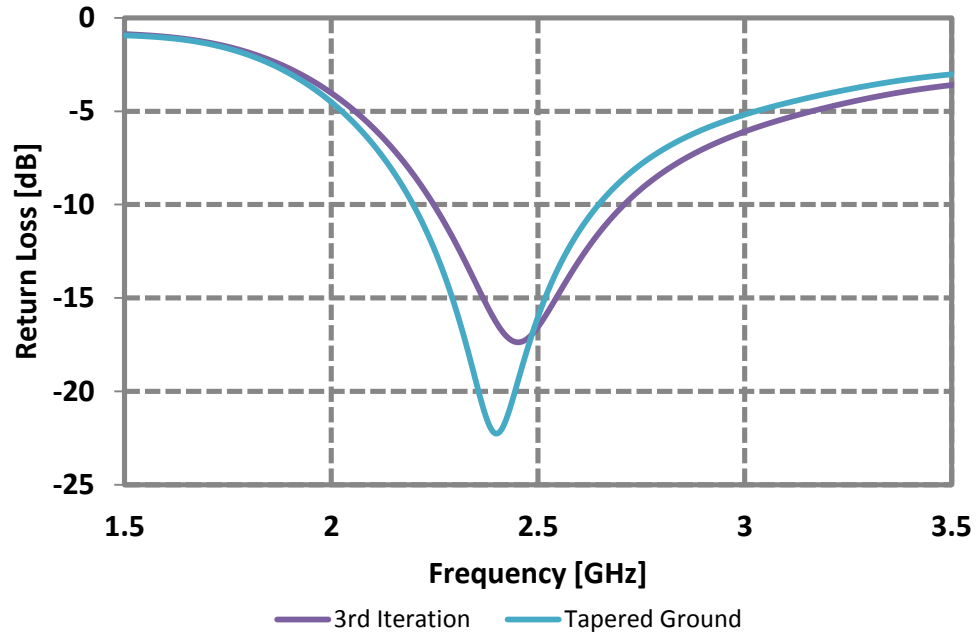


Figure 40: Increased Match by Tapering Ground Plane

As the Sierpinski Monopole is a planar monopole with truncated ground plane, the radiation is similar to that of a broadside radiating wire antenna or dipole. The E (vertical or phi) and H (horizontal or theta) cuts are shown in Figure 41.

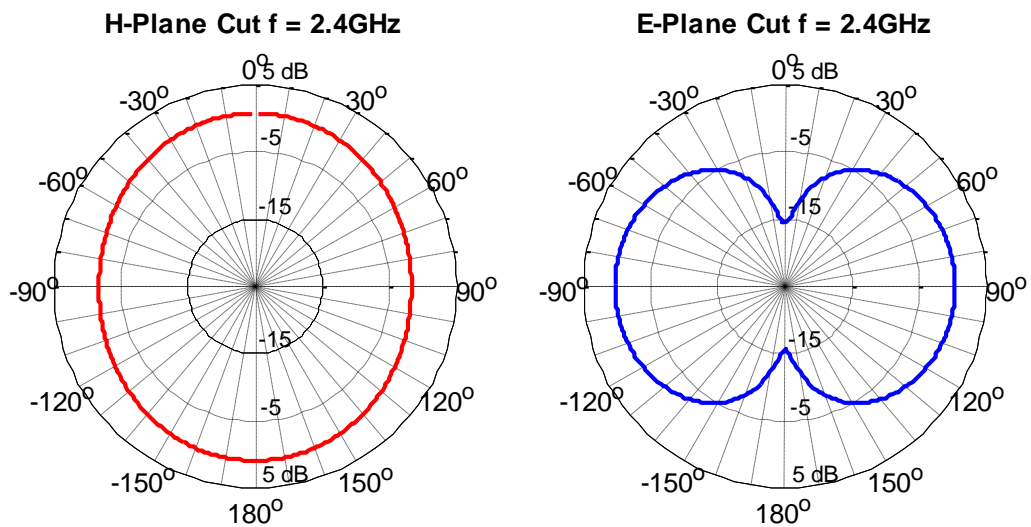


Figure 41: Simulated Radiation Pattern of Sierpinski Monopole

The maximum simulated gain of the antenna is 1 dBi and the pattern is nearly isotropic in the H-plane.

#### 4.1.2 Sierpinski Monopole Fabrication

Since the Sierpinski monopole is a two layer antenna, the radiator and patterned ground plane will be printed separately on a sheet of photo paper, aligned, and then glued together with a thin layer of spray adhesive. Two sided printing is possible, but as paper is thin (220um per sheet), a 50 ohm microstrip line is only 500um in width. To increase the microstrip width which decreases losses, two sheets of paper are used increasing the microstrip width to around 1mm. The mask for the Sierpinski Monopole is shown in Figure 42 which incorporates the ground plane, radiator, and alignment marks for combining the two layers after fabrication. The layers are aligned by laser cutting holes in the center of the alignment marks, and feeding alignment pins through the holes on each substrate. The two substrates are then slid together on an alignment jig with a thin layer of spray adhesive on the back side of the top layer which is illustrated in Figure 43.

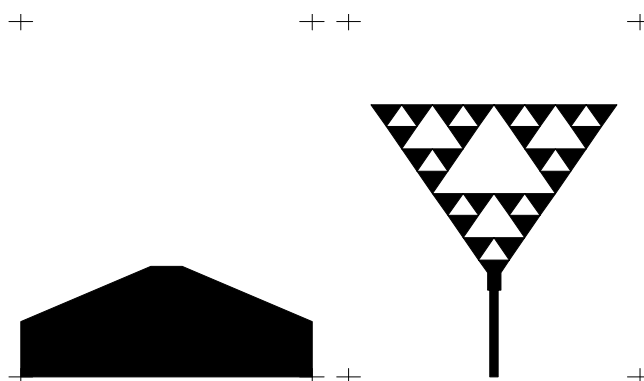


Figure 42: Mask for Sierpinski Fractal Monopole

Once the two layers are joined together, an SMA connector is mounted with a conductive epoxy as soldering will burn the paper. The entire antenna is then put in an oven to cure the epoxy. The final fabricated antenna is shown in Figure 43.

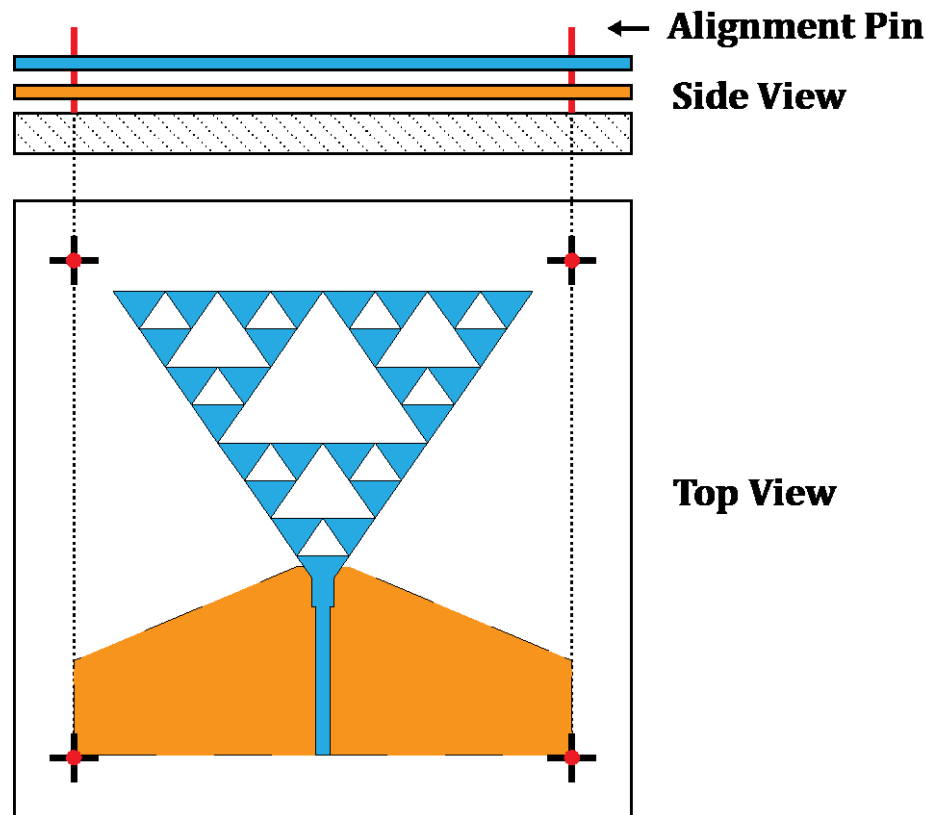


Figure 43: Layer Alignment for Printed Structures

### 4.1.3 Sierpinski Monopole Measurements

The fabricated Sierpinski monopole is shown in Figure 44. The SMA connector connected with a silver heat cure epoxy can be clearly seen. In order to ensure correct operation of the fabricated antenna, the return loss is measured using a

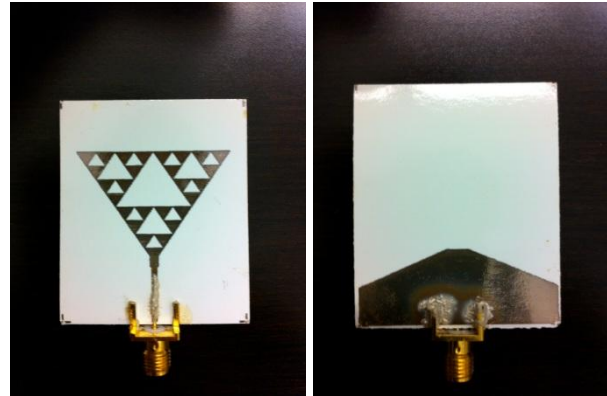


Figure 44: Fabricated Sierpinski Monopole

Agilent 8720ES 40GHz VNA and plotted against the simulated return loss in Figure 45. The measurements were performed in a 0.4 – 40 GHz NSI anechoic chamber at Rose-Hulman Institute of Technology.

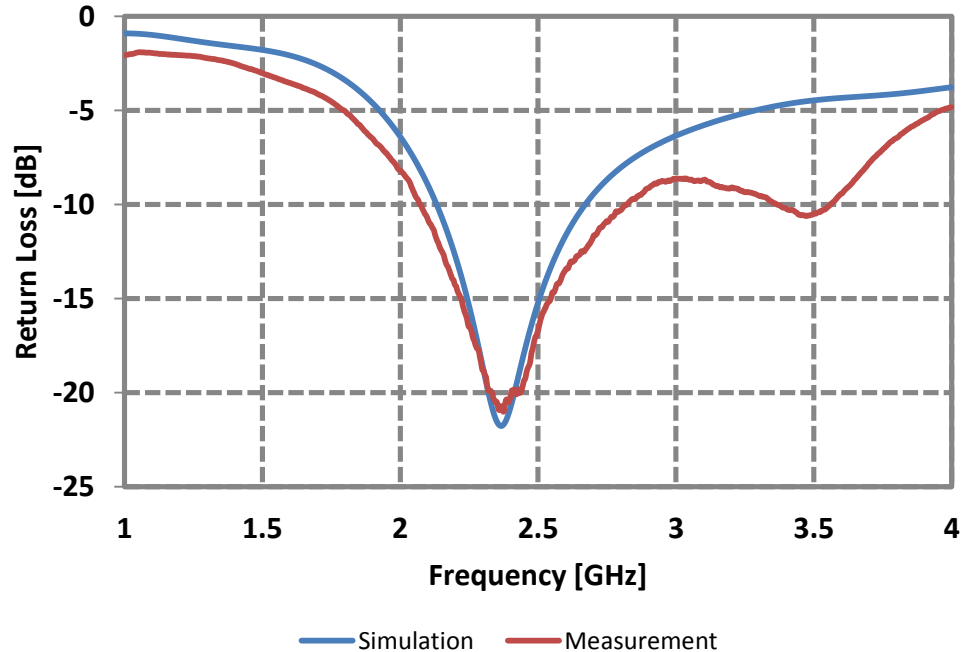


Figure 45: Mask for Sierpinski Fractal Monopole

As shown, the measured return loss is very close to the simulated return loss of the structure. The resonant frequency matches the simulated resonant frequency and the bandwidth follows simulations quite well. There is another small dip on the return loss around 3.5 GHz which may be caused by parasitics from the connector mounting and cable radiation as the truncated ground plane may not be at perfect ground potential which will send return current down the outside of the cable. Further simulations including a connector and coax cable can be performed to confirm this but as the main operating band matches simulations well, this will not be investigated during this thesis.

The radiation pattern is then measured in a 0.5 – 40 GHz tapered farfield chamber provided by King Abdullahziz City for Science and Technology, Riyadh [45], and the results are shown in Figure 46. The radiation pattern at 2.4 GHz matches well with the simulated pattern, and the max gain of the measured antenna is 0.97 dB, which is very close to the max gain in dB in simulation. The discrepancies that do appear in the pattern measurements may come from connector parasitics, and cable radiation due to the asymmetric microstrip to monopole transition. As discussed earlier, return currents have the potential to flow on the outer edge of the coaxial cable caused by the truncated ground being at a slightly different potential than ground which will cause interference and decreased gain in the measured radiation pattern. However, the simulated and measured results are closely related for return loss and radiation pattern.

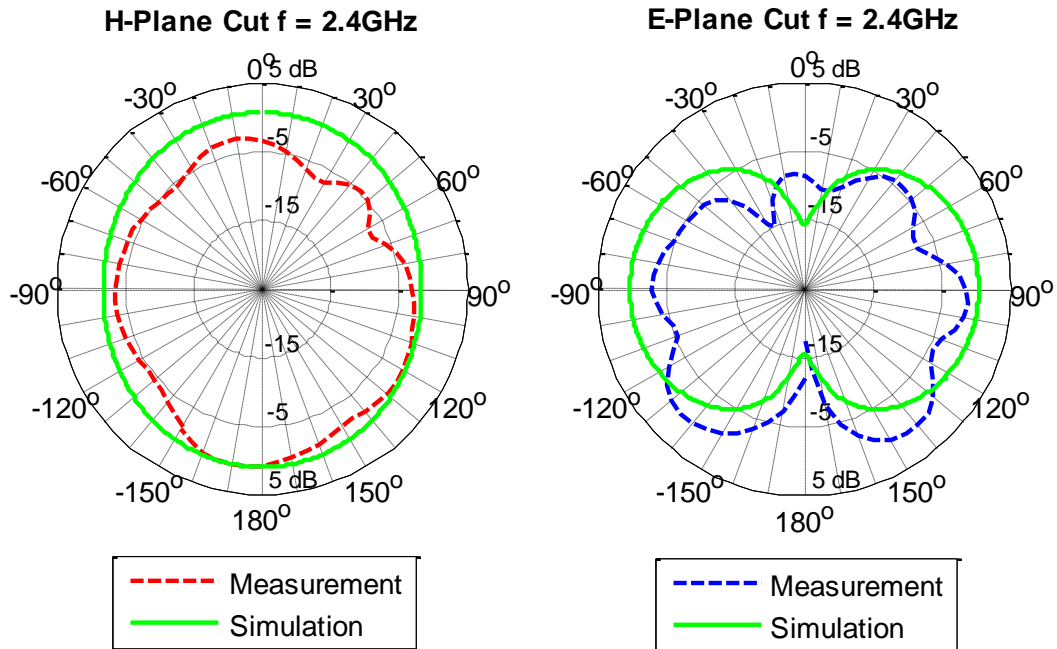


Figure 46: Increased Match by Tapering Ground Plane

#### 4.1.4 Summary

By implementing fractal design, the ink consumption and antenna performance of a 2.4 GHz triangular monopole are improved. Wideband and omni-directional performance is also achieved. The design has been successfully ink-jetted and the measured results match simulation within a margin of error. A table comparing the simulated and measured results is displayed below.

Table 10: Comparison of Measured and Simulated Sierpinski Monopole Parameters

	Simulation	Measurement
Resonant Frequency	2.4 GHz	2.35 GHz
Bandwidth	564 MHz	737 MHz
Gain	1 dB	0.97 dB

## 4.2 UWB Sierpinski Monopole

The previous section demonstrates a complete fabricated wideband antenna on paper using fractal design to reduce ink usage and increase the antenna's electrical length. The next step is to design and fabricate a UWB (3.1 – 10.6 GHz) antenna to prove that large bandwidths can be covered by paper-based inkjet-printed antennas. This is important as wearable antennas for high data rate applications can exploit the UWB band using very low emission rates for high data throughput – up to 500Mbps at 10 meters [46]. Several methods have been used to improve the impedance bandwidth of the monopole. One application demonstrated in the

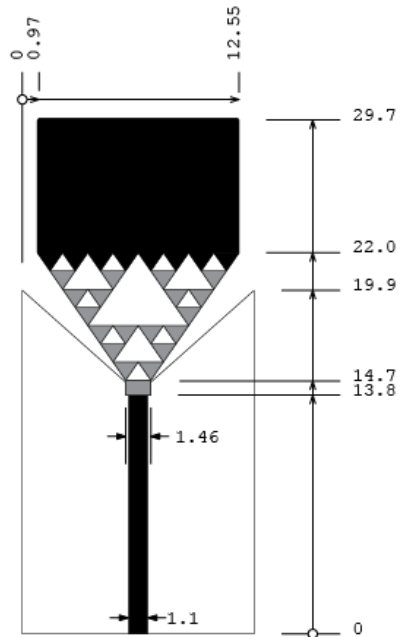


Figure 47: UWB Monopole Design

literature to which the Sierpinski Gasket ink reduction technique can be applied is the incorporation of a tapered triangular matching network (grey) to a square microstrip monopole [47]. The tapered matching network greatly extends the impedance bandwidth of the monopole allowing for bandwidths of nearly a decade. The design of the proposed antenna is shown in Figure 47. Another consideration for this antenna is that the currently published UWB inkjet-printed antenna has radiating element dimensions of 6 x 6 [29] cm, so the dimensions of the radiating element of this antenna should be smaller. As shown in Figure 47, the radiating element dimensions are 1.5 x 1.35 cm which is around 16 times smaller than the currently published inkjet-printed UWB antenna. This is due to the fact that the

operating frequency of the previously published antenna works down to 2 GHz instead of 3.1 GHz, and because the fractal design allows this monopole to be a factor smaller than non-fractal matched UWB monopoles.

#### 4.2.1 UWB Sierpinski Monopole Design

The antenna is composed of a microstrip feed line, a tapered transition into a monopole using the Sierpinski fractal, and a tapered ground plane to aid in extending the impedance bandwidth of the antenna. The width of the microstrip line and substrate thickness are again 1.1 mm and 440  $\mu\text{m}$  respectively as the substrate used is two layers of photo paper – one for the top radiating element and one for the ground plane. When designing the antenna, several variables were taken into account: the height of the monopole ( $h$ ), the width of the monopole ( $w$ ), and the angle of the taper ( $\theta$ ).

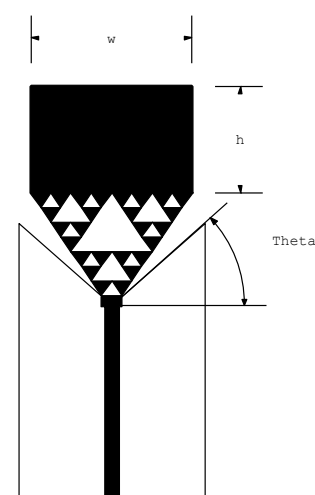


Figure 48: UWB Monopole

The height of the monopole is selected to be one quarter wavelength on a paper substrate which is near 15mm, and the triangular taper is chosen to be an isosceles triangle which fixes the width of the monopole. To determine the best transition angle for wideband impedance matching, the ground tapering angle is swept from 0 to 60°. Simulation results of the sweep in Figure 49 show that the optimum angle is near 45° meaning the gap between the monopole and ground taper is 15°.



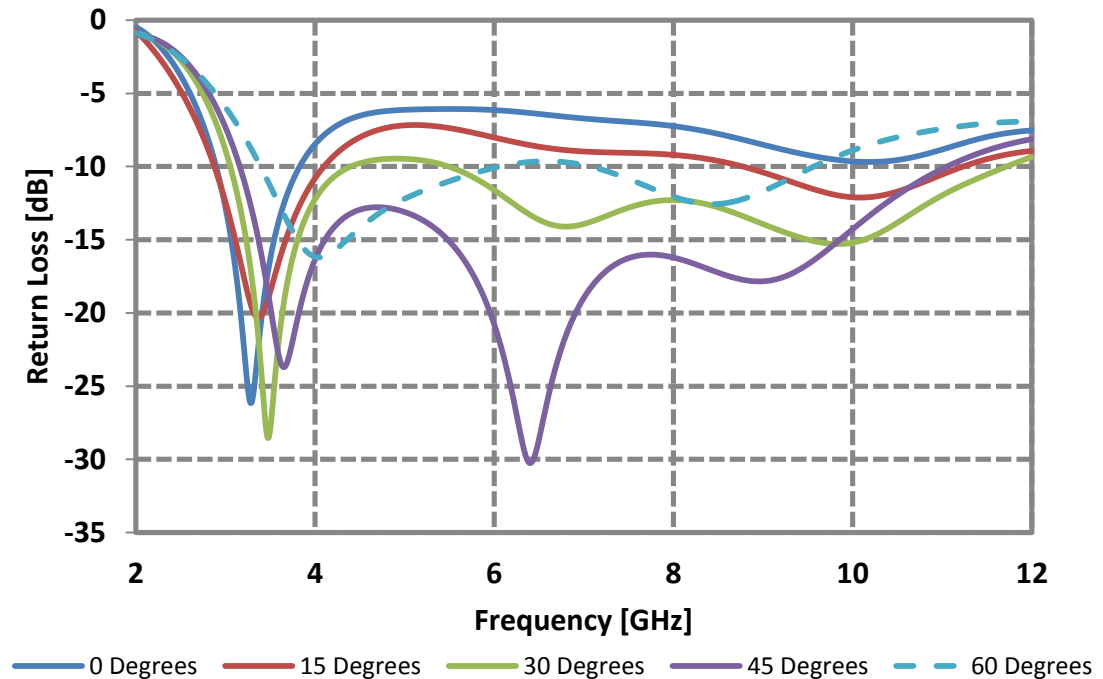


Figure 49: Sweep of Ground Tapering Angle on UWB Monopole

The simulations for the ground tapering include the fractal pattern in the triangular impedance matching section of the monopole which is used to decrease ink usage and the lower operating frequency of the antenna as shown in the previous section. The simulation in Figure 50 shows the effects of not including the fractal in the matching network. As shown, the fractal pattern lowers the lowest operating frequency by about 200 MHz and enhances match while keeping the high end of the operational band the same.

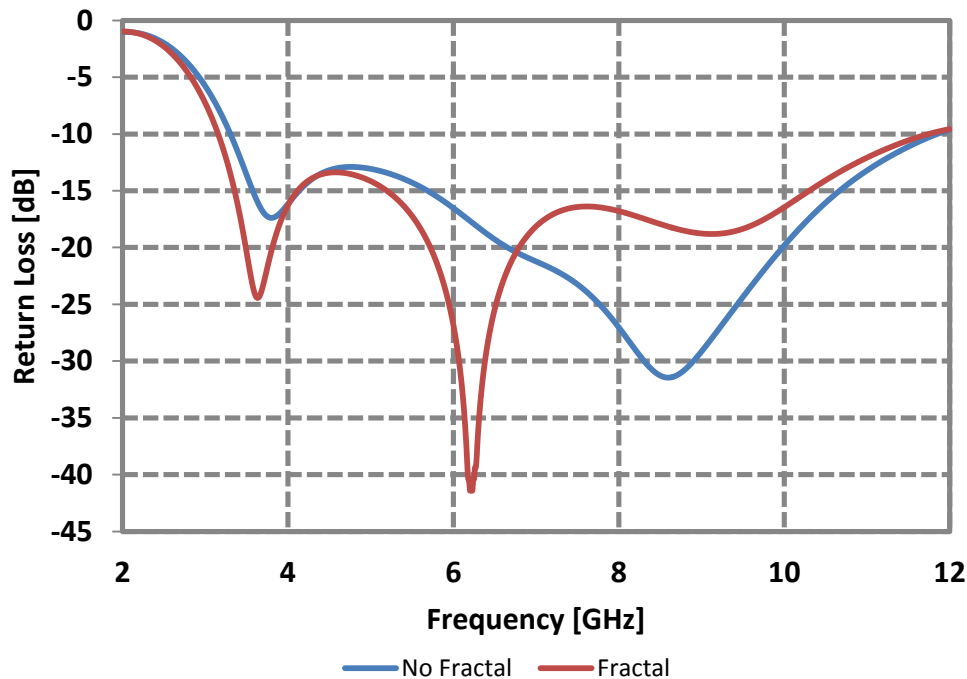


Figure 50: Fractal vs. Non Fractal Matching Network

The radiation pattern of the UWB monopole is similar to that of a microstrip monopole, or dipole having a somewhat isotropic pattern in the H-Plane, and a doughnut shaped pattern in the E-Plane. The radiation patterns for several frequencies over the UWB band are shown below. As seen, there is not a large variation in pattern over the operating range. The maximum gain over the frequency range however does change which is common for antennas with such bandwidth because of electrical size and pattern interference at different frequencies which is displayed in Figure 52.

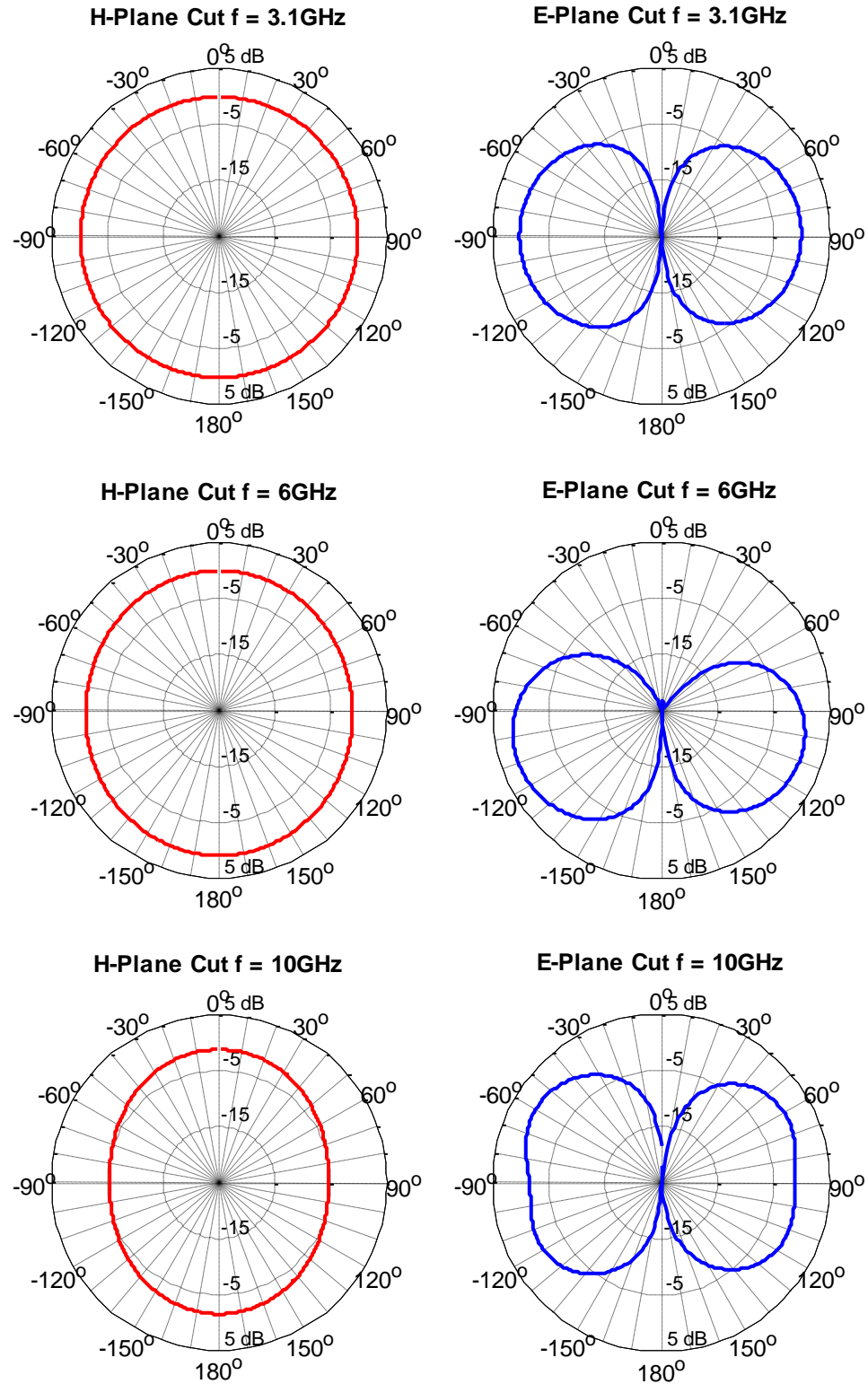


Figure 51: Simulated Pattern for UWB Monopole

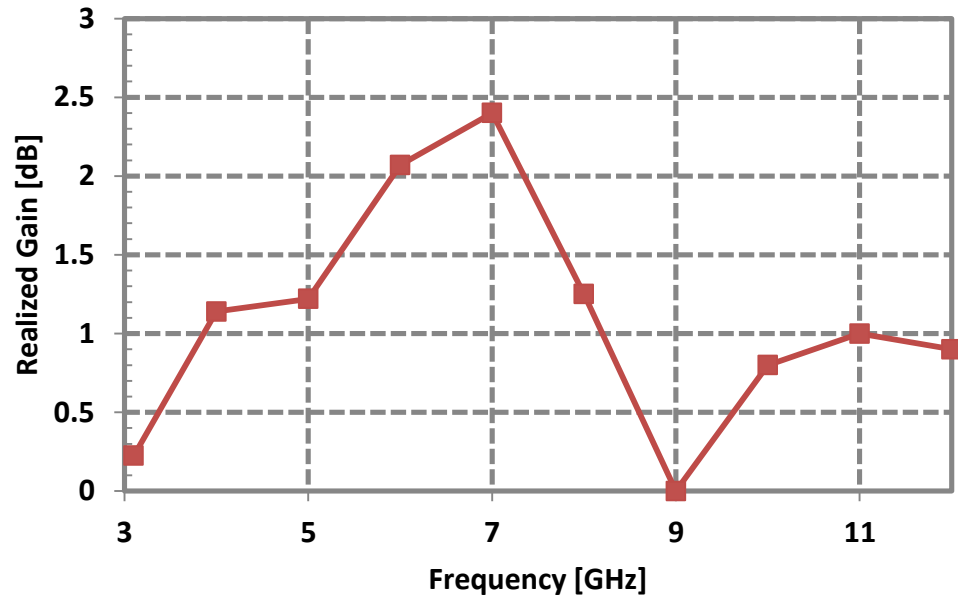


Figure 52: Simulated Gain vs. Frequency of the UWB Monopole Antenna

#### 4.2.2 UWB Monopole Measurements

The fabricated UWB monopole is shown to the right in Figure 53. After fabrication, the return loss is measured using an Agilent 8720ES 40GHz VNA to ensure correct operation. As seen in Figure 54, the operating frequency is from 3.4 – 10.6 GHz which is slightly off from the simulated 3.1 – 11 GHz operating range.

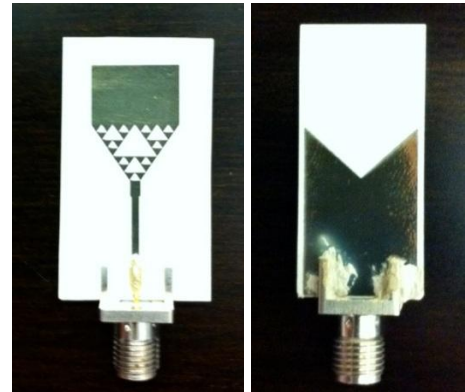


Figure 53: Fabricated UWB Monopole

But, as the antenna is very dependent on alignment of the top and bottom layers and alignment is only accurate to several hundred microns when gluing multiple pieces of paper together (see Figure 43), the results are satisfactory and the antenna will work for the UWB band.

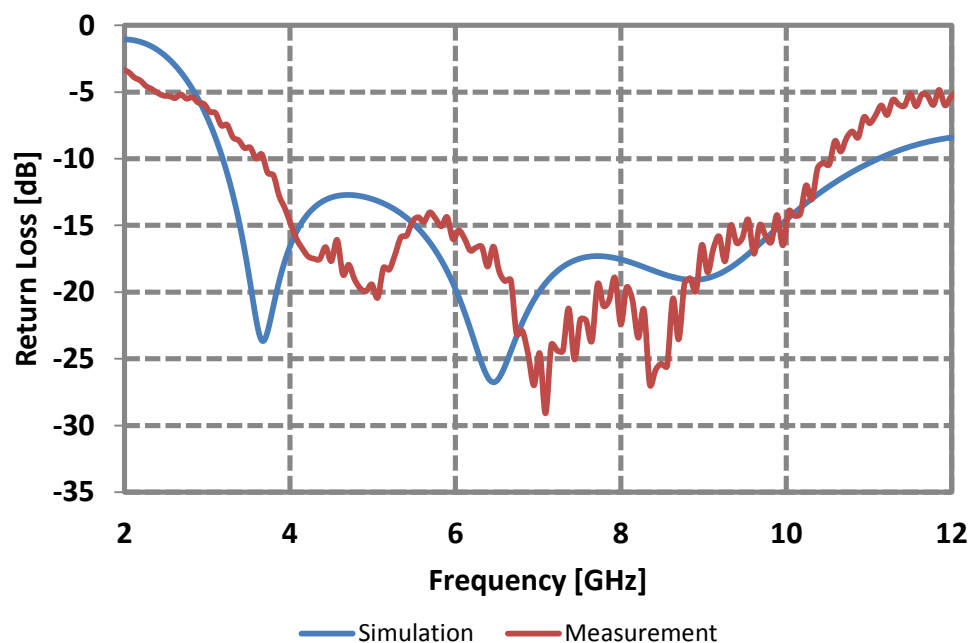
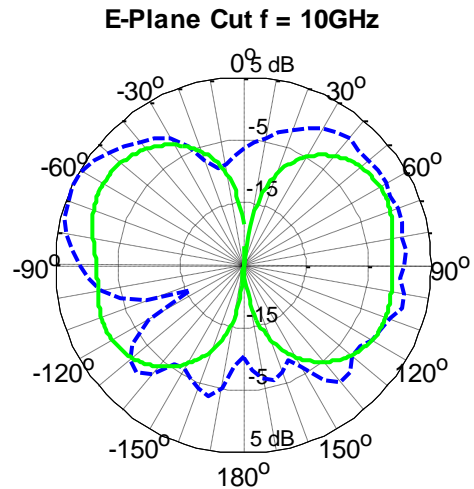
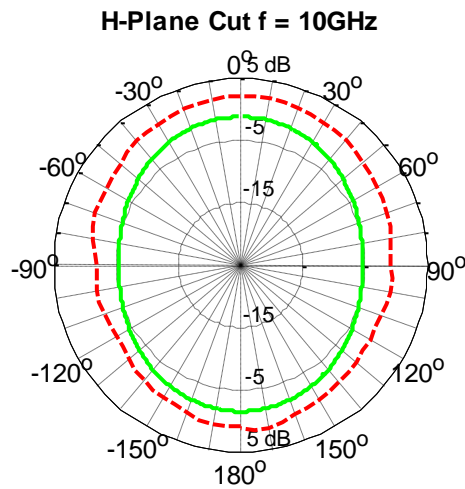
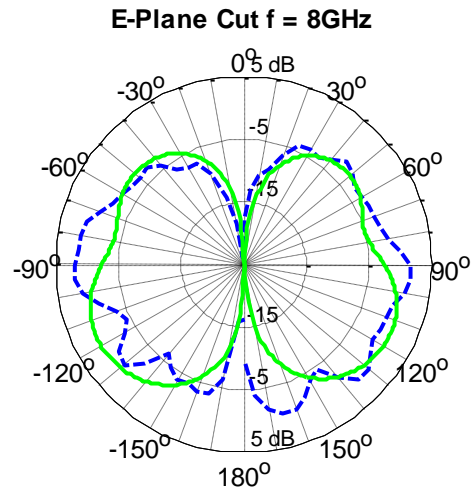
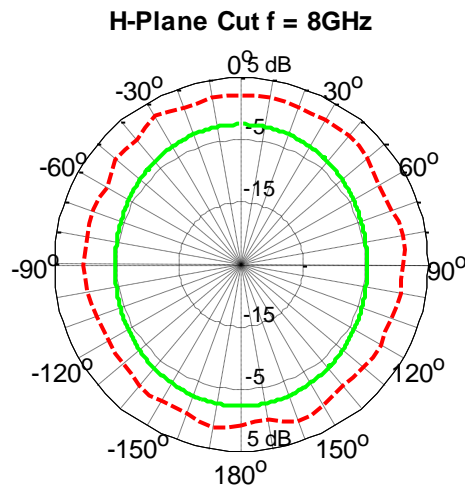
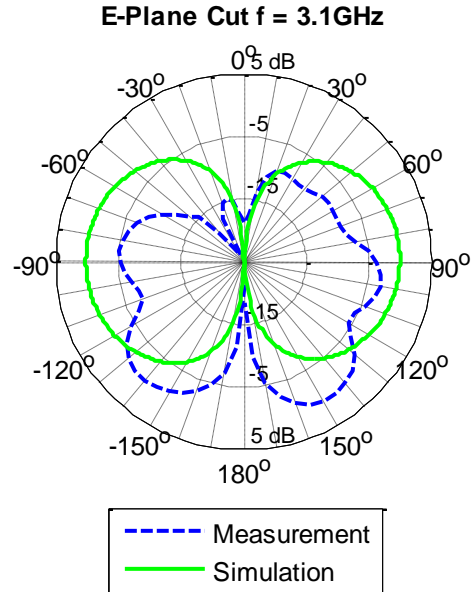
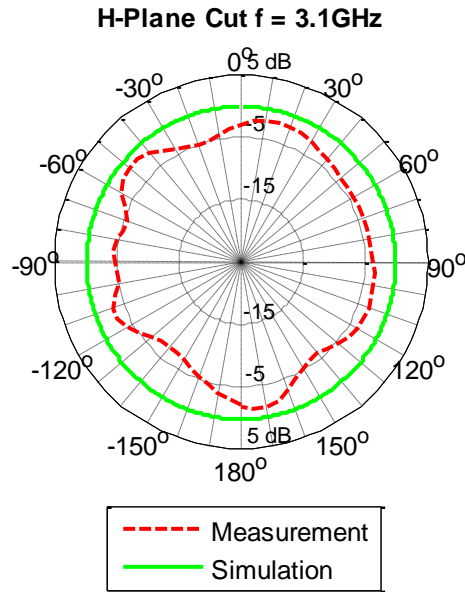


Figure 54: UWB Monopole Return Loss Measurement

The measured gains and radiation patterns for several frequencies are shown in Figure 55. As seen, the simulated and measured patterns are very similar having omni-directional radiation in the H-Plane, and dipole-like radiation in the E-Plane. Some non-symmetries are present which is in the most likely case is due to cable radiation which is a common problem in coaxial cable antenna measurements. As the cable and SMA connector are not modeled in the simulation, this is a very likely source of error.



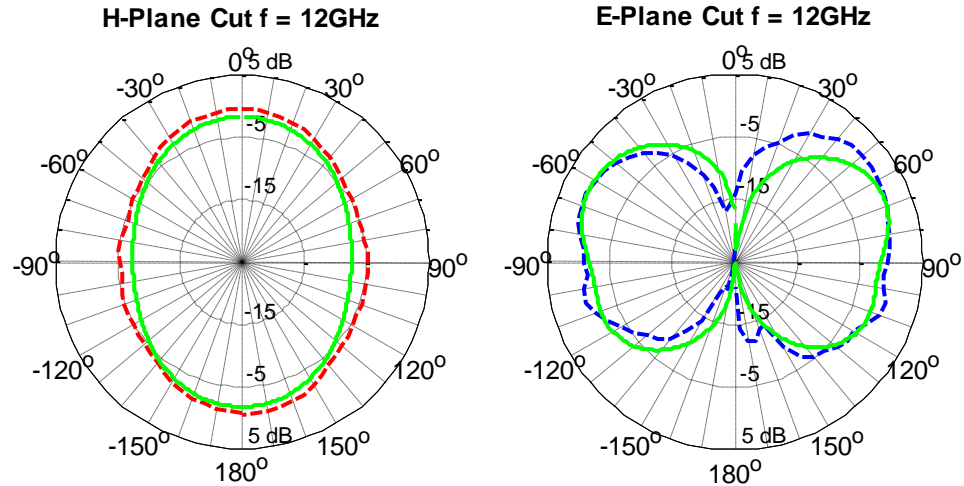


Figure 55: Simulated vs. Measured Gain and Radiation Pattern of UWB Monopole

The measured and simulated maximum gain vs. frequency is shown in Figure 56. As seen the gain pattern follows well at the lower frequency band but higher by 2dB from 9-11 GHz. This is a trend that is seen in several of the antenna measurements, and is attributed to a calibration error in the measurement chamber around this frequency.

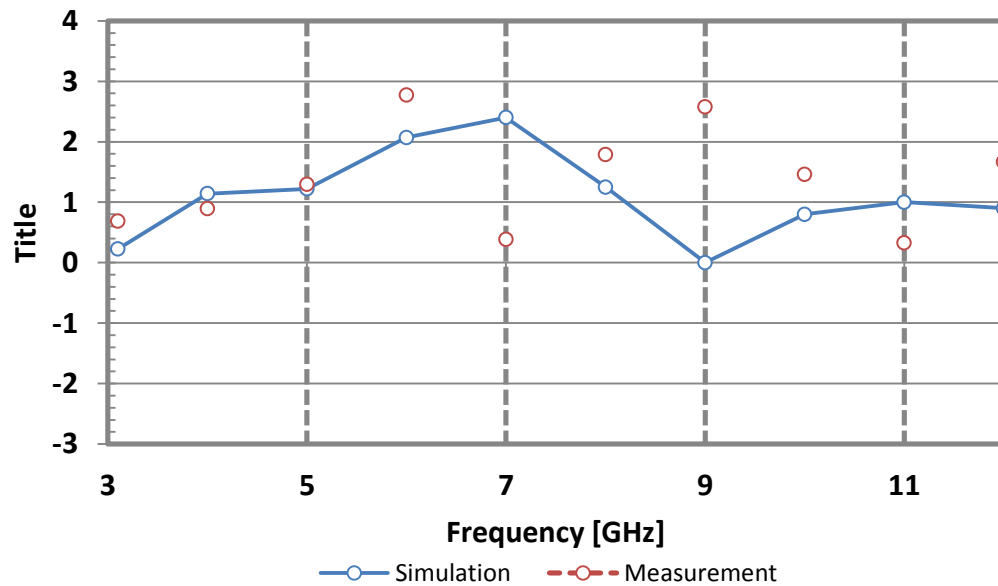


Figure 56: Max Realized Gain vs. Frequency



### **4.2.3 Summary**

As shown in return loss and radiation pattern measurements, the UWB monopole with fractal matching network exhibits positive gains and below -10dB return loss over the UWB band with the exception of the lower end of the band which starts at 3.4 GHz – though the gain is still positive down to 3 GHz. A second version of the UWB monopole is discussed in the following section which addresses this issue.

### 4.3 UWB Sierpinski Monopole Version 2

As demonstrated in the previous section, an inkjet-printed UWB monopole sixteen times smaller than currently published inkjet-printed UWB antennas was achieved, and the Sierpinski Gasket pattern was used to lower the operating frequency and decrease ink usage. The only issue was that during fabrication, the lower operating frequency was shifted from 3.1 to 3.4 GHz. Several issues including alignment offsets most likely attributed to this problem.

A second version of the monopole was designed which exhibits slightly better low end matching by truncating the ground taper. This creates a larger gap between the radiator and ground plane which lowers the lowest operating frequency. The second version is shown in Figure 57.

The return loss for the second version of the UWB monopole is compared against the first in

Figure 58. As seen, the low end performance has a better match while the high end does not suffer from the truncation of the ground plane.

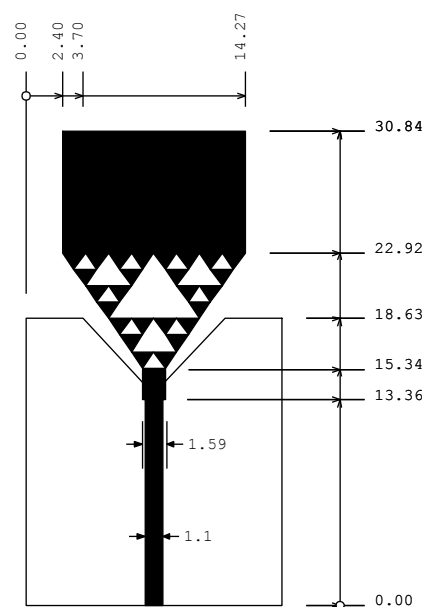


Figure 57: Version 2 UWB Monopole Antenna

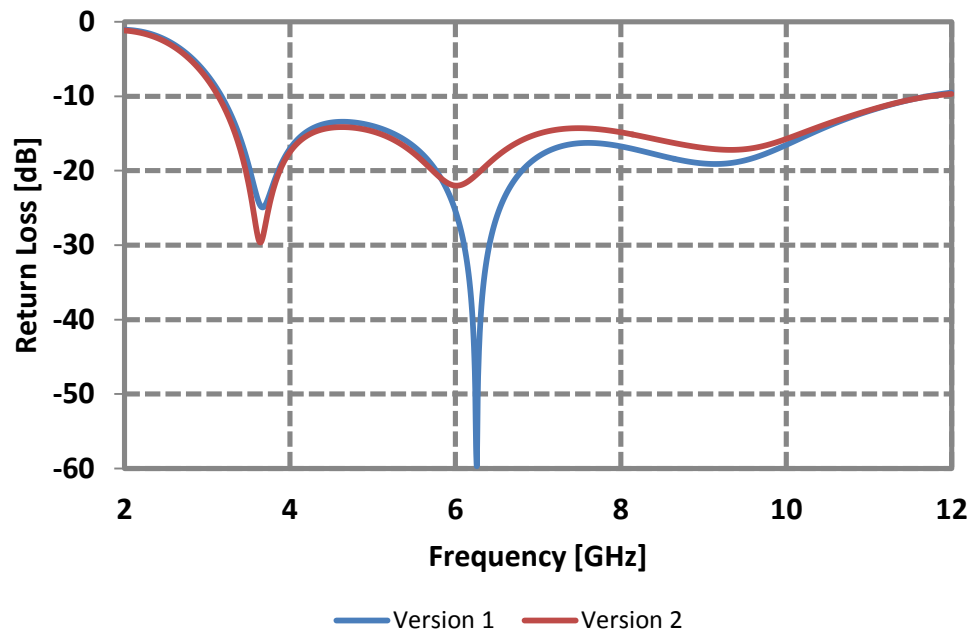


Figure 58: First and Second Version of the UWB Monopole

#### 4.3.1 UWB Sierpinski Monopole Version 2 Measurements

Again, the return loss and radiation pattern are measured to confirm the operation of the antenna. As seen in Figure 60, the return loss matches the simulation much better, and the lower end operation point is 3.15 GHz. The higher end however, is at -8dB at 10.6GHz – the upper end of the UWB band – which

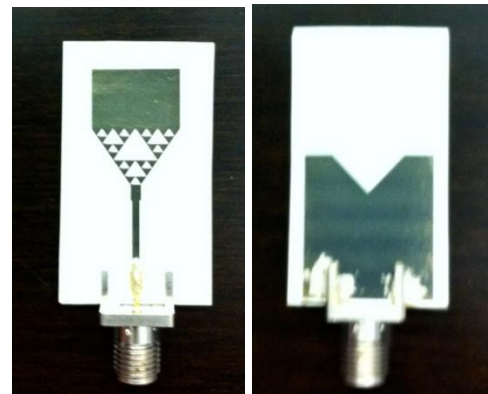


Figure 59: Fabricated UWB Monopole V2

corresponds to a VSWR of 2.25. Several specifications allow for the VSWR to be below 3, meaning around 70% power transmitted over the band.

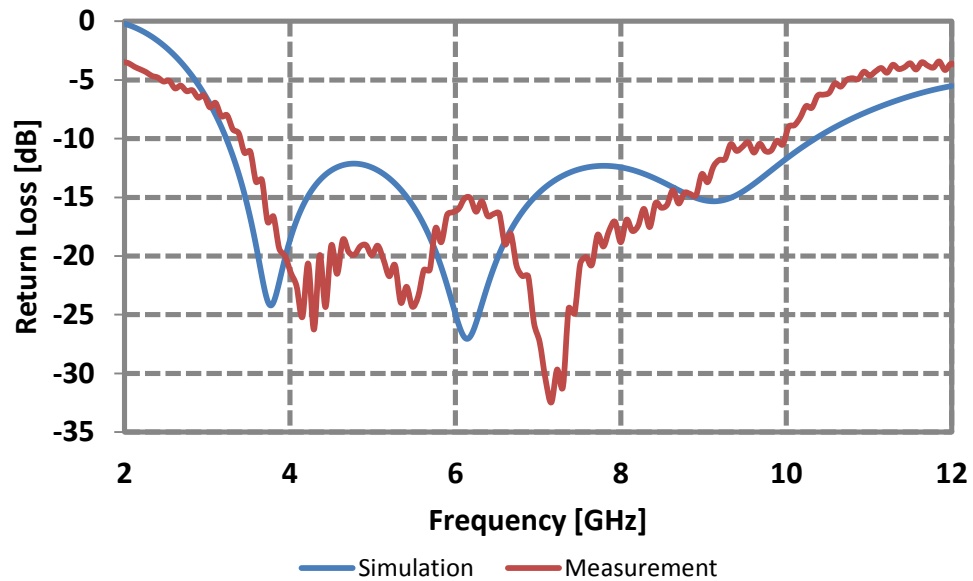


Figure 60: UWB Monopole Version 2 Return Loss Measurement

The radiation pattern and gain are measured to quantify the operation of the second version of the UWB monopole. Several selected patterns over the operating range of the antenna are displayed below which show a good agreement between the measured and simulated patterns. The gain vs. frequency is displayed in Figure 62, which shows a better gain around 9 GHz than the simulated antenna, and positive gains over the entire UWB band.

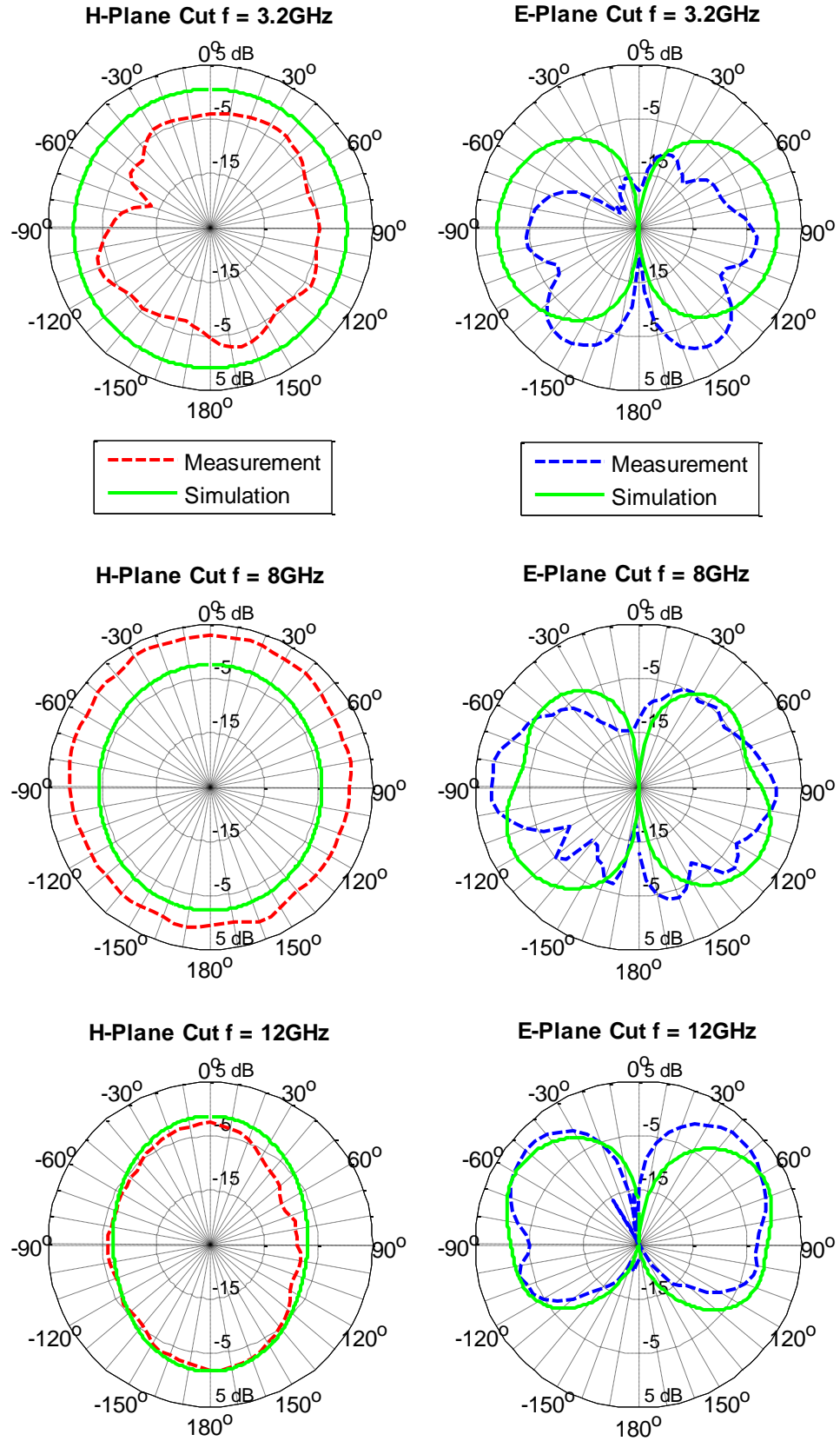


Figure 61: UWB Monopole Version 2 Pattern Measurements

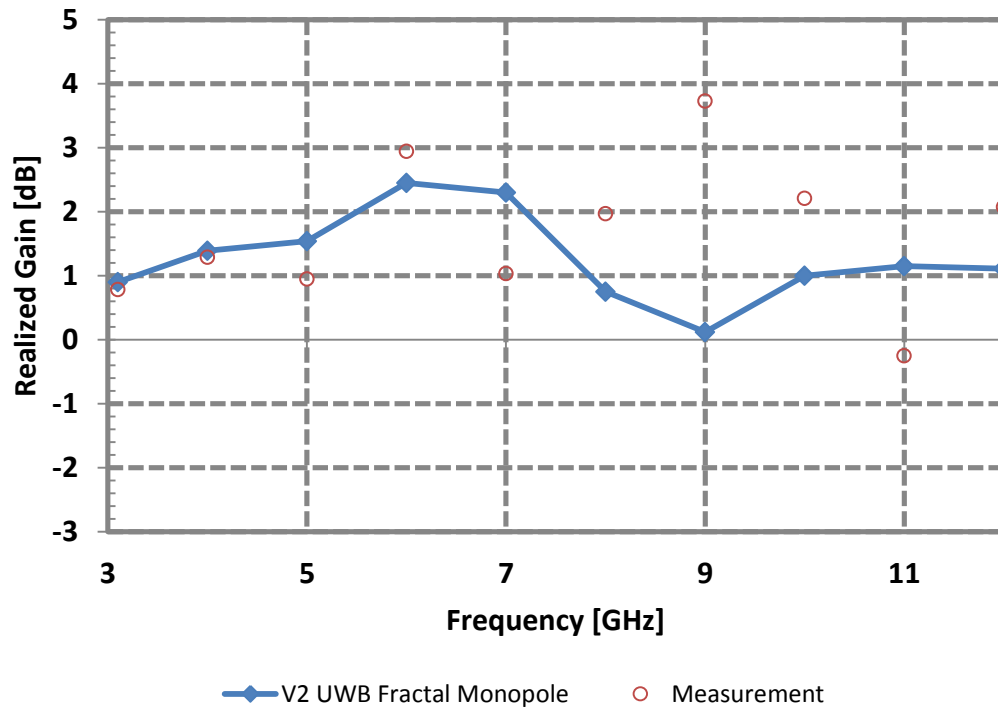


Figure 62: UWB Monopole Version 2 Gain Vs. Frequency

### 4.3.2 Summary

This chapter has discussed two versions of a microstrip fed UWB monopole that uses a Sierpinski fractal pattern to reduce ink usage and decrease the lowest operating frequency allowing for device minimization. Both antennas operate with a VSWR of under 2.25 over the UWB band and show positive gains from 3 – 11GHz. The patterns are nearly isotropic in the H-Plane and similar to a Dipole in the E-Plane. The antenna has been able to cover the UWB band with a 16x smaller footprint than currently published inkjetted UWB antennas on paper.

---

## 5. DIRECTIVE UWB PRINTED ANTENNAS

---

While the antennas demonstrated in Chapter 4 exhibit wideband operation, their omnidirectional behavior restricts them to applications where communication range is not important. On the other hand, several applications such as long-range communications, directional receiving/transmitting to base stations, and energy harvesting require higher gains and directional beam antennas.

As already discussed in Chapter 1, there are currently no published directional, high gain antennas that have been inkjet-printed in general, let alone on paper. The highest published gain from an inkjet-printed antenna is around 3 dB which is shown earlier in Table 2. The work in this chapter focuses on producing directional and high gain antennas that also demonstrate ultra-wide bandwidth. The aim is to demonstrate that inkjet printing is a viable fabrication method that may be extended to applications requiring gains above several dB.

In order to achieve high gains and wide bandwidth, several antennas such as log periodic dipole arrays, horns, cavity backed spirals, and Vivaldi antennas have previously been demonstrated. Since inkjet printing is currently a planar process, Vivaldi antennas and log periodic dipole arrays are an optimum choice.

The antennas presented in this section include two variations on a Vivaldi antenna intended to operate over the entire FCC UWB band, and a planar log periodic dipole

array which is used for energy harvesting in the American UHF television band. The target is to achieve gains above 5dB using inkjet-printing on a paper substrate.



## 5.1 UWB Antipodal Vivaldi

The first high gain directional antenna designed is an antipodal Vivaldi with a microstrip feed. The vivaldi is a balanced traveling wave antenna in which different frequencies radiate at different distances along the tapered arm structure. A traveling wave antenna works by radiating its energy before reflections occur meaning there is no standing wave on the structure. Theoretically the vivaldi's lowest operating frequency is where the largest gap is equal to one half wavelength of the lowest operating frequency. The highest operating frequency is infinite as the arm separation goes to zero – though this will not happen in reality.

As the vivaldi is a balanced antenna, the feed needs to be a balanced, or differential input to the two arms with the currents being  $180^\circ$  out of phase. As the measurement equipment available is unbalanced, a balun is required to convert from the SMA input to differential input. As shown in Figure x, a microstrip input accepts the unbalanced signal, and a tapered ground plane to differential pair feeds the balanced arms.

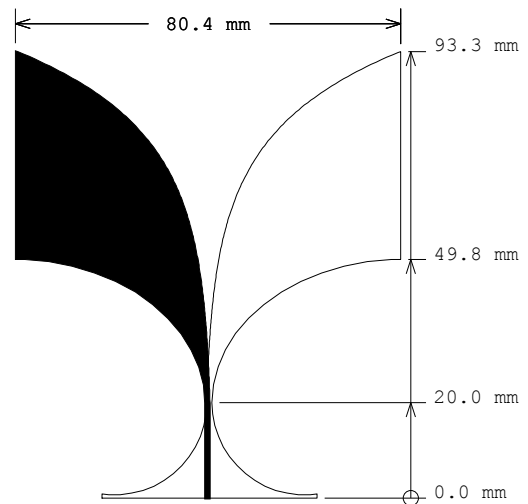


Figure 63: UWB Antipodal Vivaldi

### 5.1.1 Antipodal Vivaldi Design

The first step in designing the antipodal vivaldi is to design the microstrip to differential pair transition. This is done in CST by feeding the microstrip and differential pair ends with waveguide ports and looking at the insertion and return loss as the ground tapering radius is varied. Figure 65 shows the insertion loss for the final microstrip to differential pair transition.

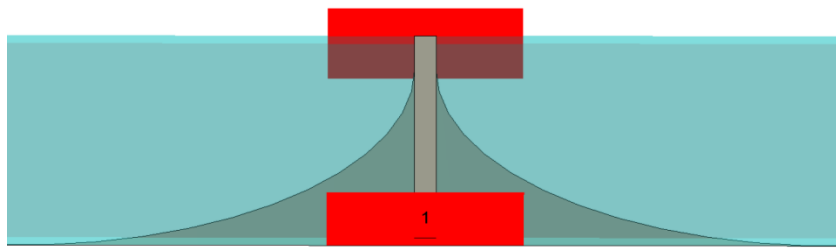


Figure 64: Vivaldi Transition

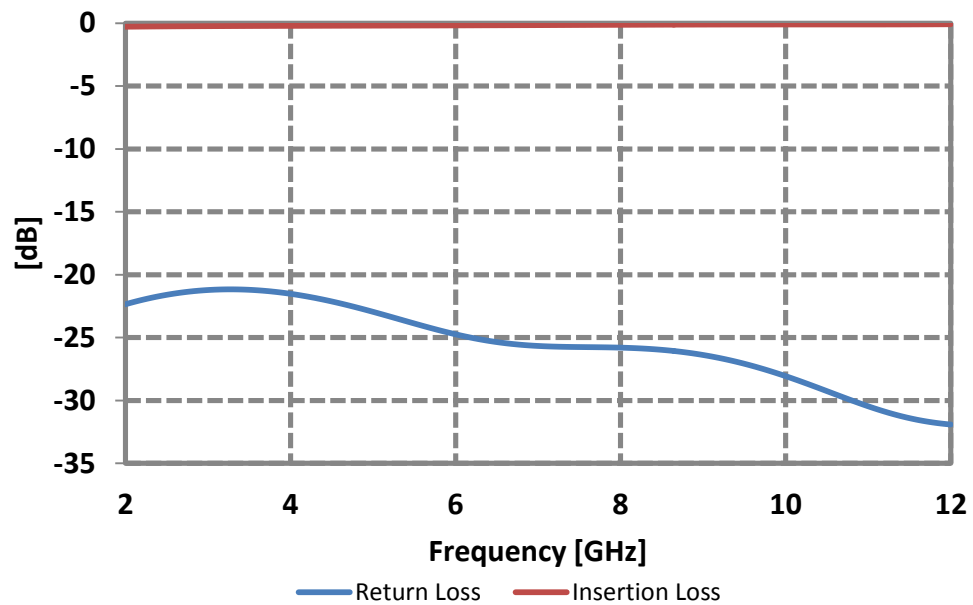


Figure 65: Vivaldi Transition Return and Insertion Loss

After obtaining a good transition, the arms are attached to the transition and the taper, which is exponential in this case, is optimized to produce the best return loss over the UWB band. The equation of the taper is shown in (15) where  $x$  is the in the direction of the length of the antenna, and  $y$  is in the direction of the width of the antenna.

$$x = 0.5 * \exp(\alpha * y) \quad (15)$$

Figure 66 below shows the effect of different values of  $\alpha$  on the tapered arms of the vivaldi and Figure 67 shows the corresponding return loss. As shown, the case where  $\alpha = 0.055$  yields a return loss of less than -10dB over the entire UWB range, and even works down to 2.1GHz under -8.5dB. Therefore,  $\alpha = 0.055$  is chosen as the taper curve.

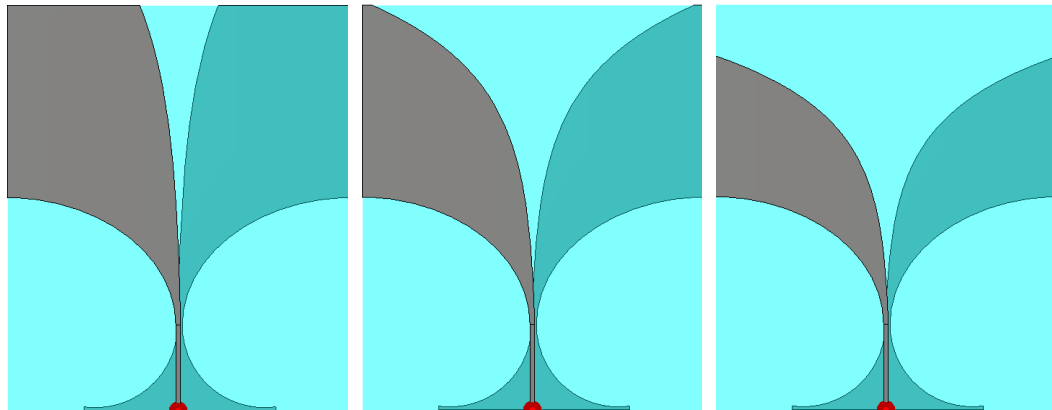


Figure 66:  $\alpha = 0.04$  (Left),  $0.055$  (Middle),  $0.07$  (Right)

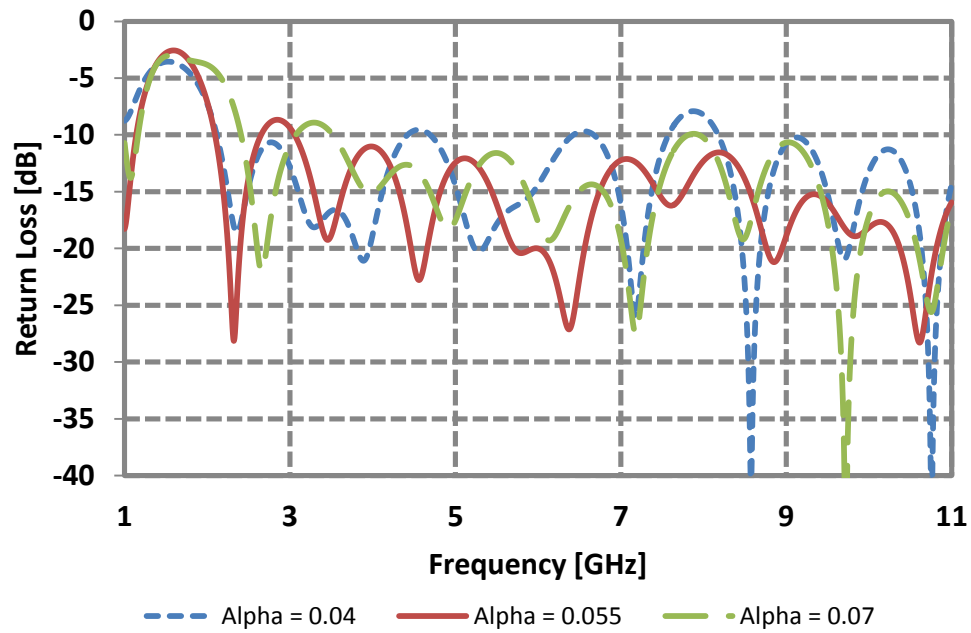


Figure 67: Return Loss for Different Alpha Values

A simulated radiation pattern in the middle of the band which is 6 GHz is shown below in Figure 68. Notice the high gain produced by the simulated antenna which is near 6.5dB. The simulated gain vs. frequency is shown in Figure 69.

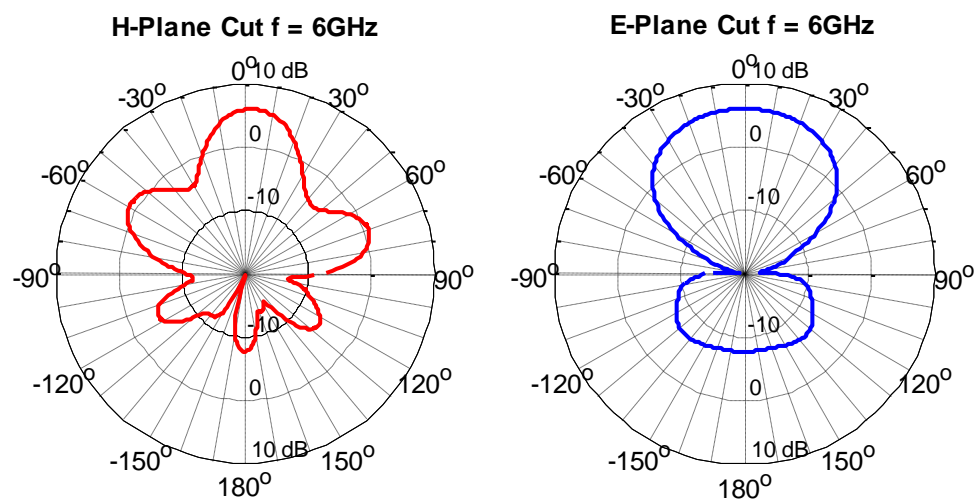


Figure 68: Vivaldi Radiation Pattern at 6 GHz

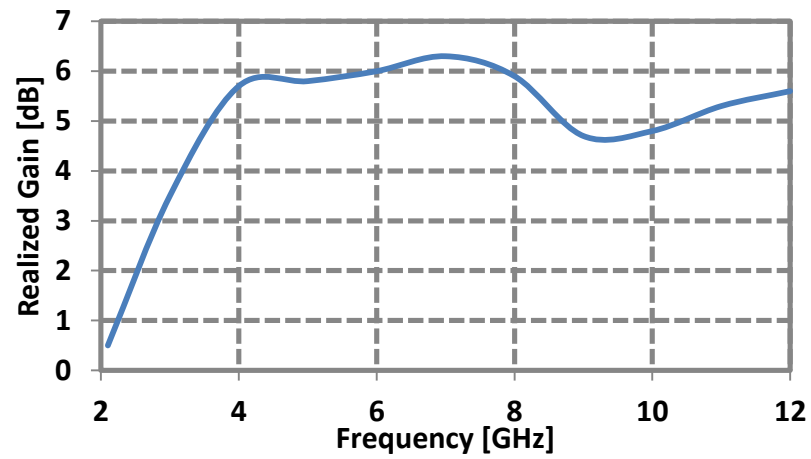


Figure 69: Vivaldi Gain vs. Frequency

As seen, the simulated gain at the start of the UWB band is near 4 dB and averages 5.5 dB over the bandwidth of the antenna. From 4 – 12 GHz the gain is very stable varying by only 1 dB.

### 5.1.2 Antipodal Vivaldi Measurements

The final fabricated vivaldi is displayed in Figure 70. The same alignment methods were used as discussed in Section 4.1.2 to align the two halves of the antenna.

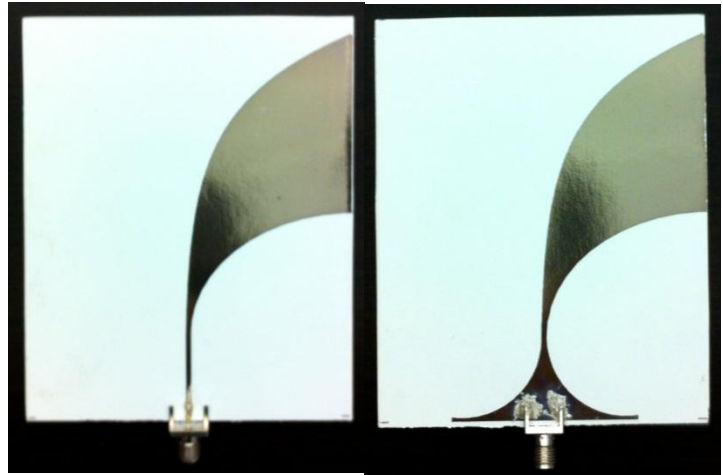


Figure 70: Fabricated Vivaldi

The return loss is first measured using an Agilent 8720ES 40GHz VNA in an anechoic chamber. The measured return loss is displayed in Figure 71.

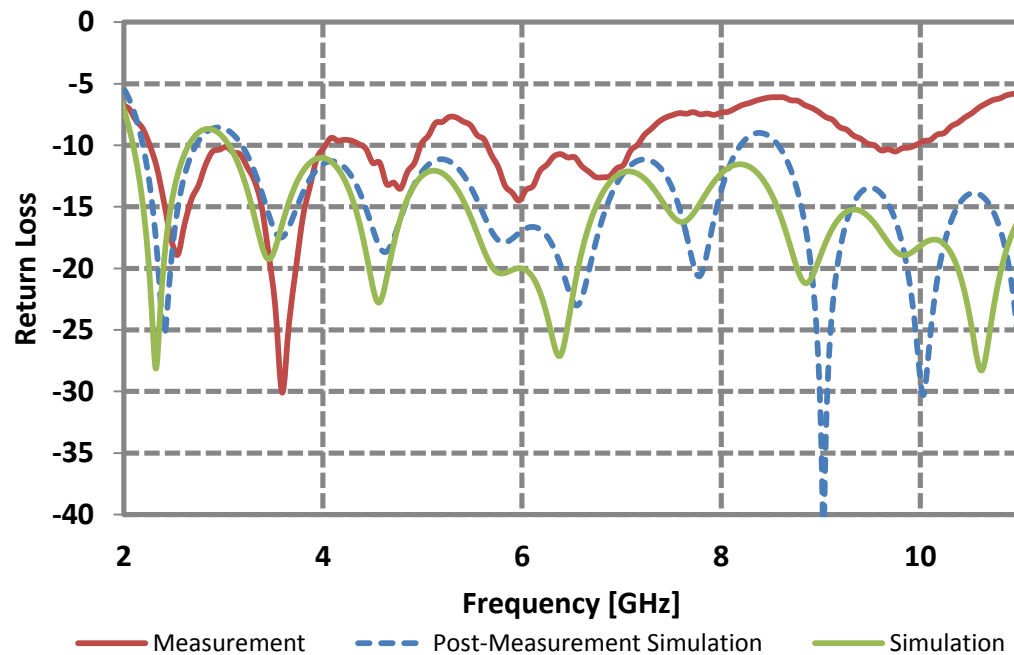
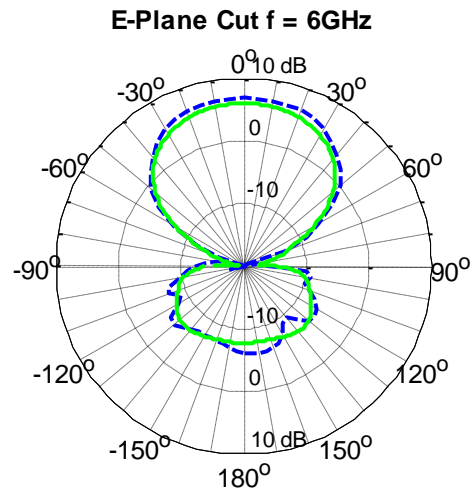
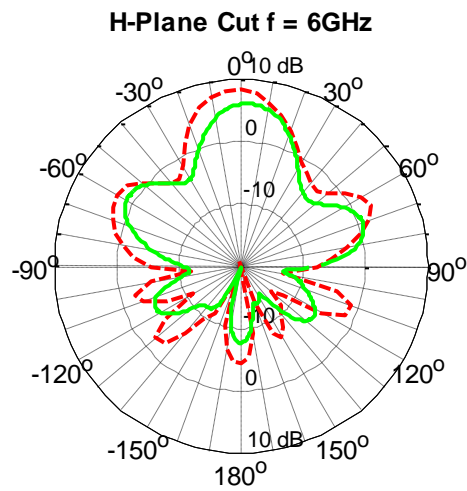
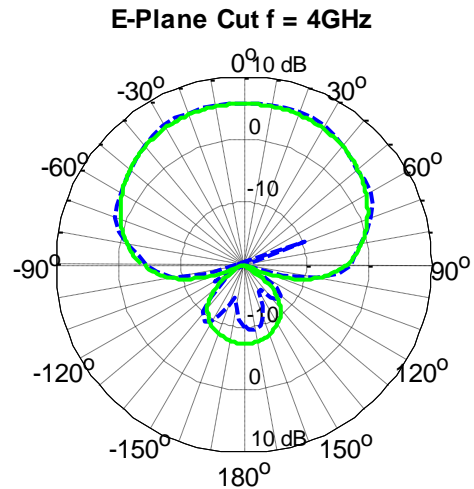
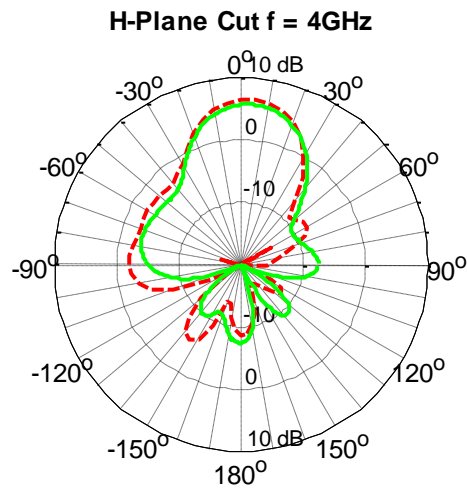
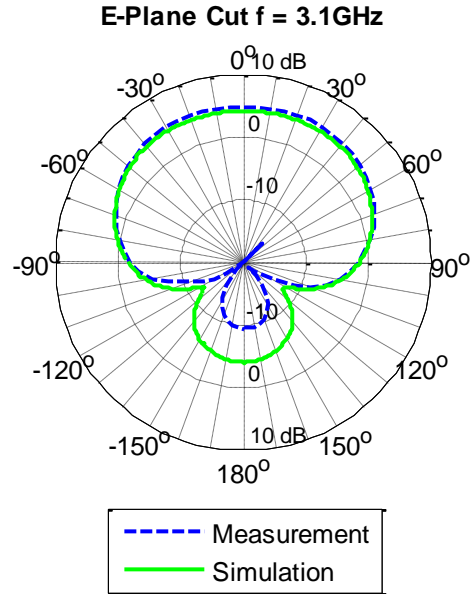
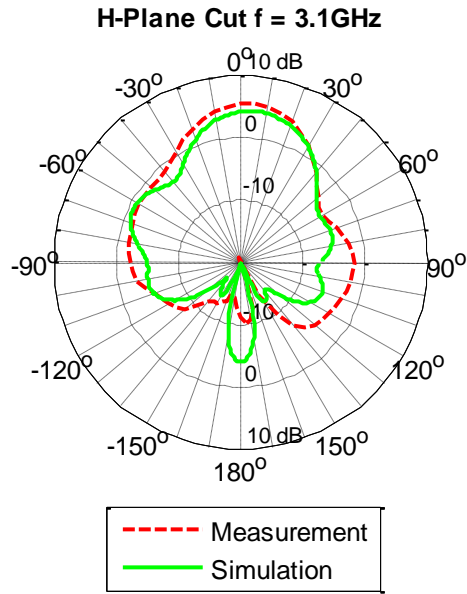


Figure 71: Vivaldi Measurement Vs. Simulation

As seen, the return loss goes above -10dB near 5 GHz and 7 GHz which does not match the simulation. After placing the antenna on a light table and inspecting the alignment, it is found that the upper and lower layers are displaced horizontally by 200 $\mu$ m. By entering these parameters into the simulation and re-simulating, and using a frequency dependent permittivity a closer simulation result is obtained.

The radiation pattern and gain are then measured to confirm the radiation properties of the antenna which are shown in Figures 72 and 73 respectively. As shown, the radiation patterns match very well with the simulation, and the gain vs. frequency follows a very similar pattern to the simulation with a maximum gain of 8.6dBi. This is nearly 3 times higher than the highest gain of paper-based inkjet-printed antennas in literature.





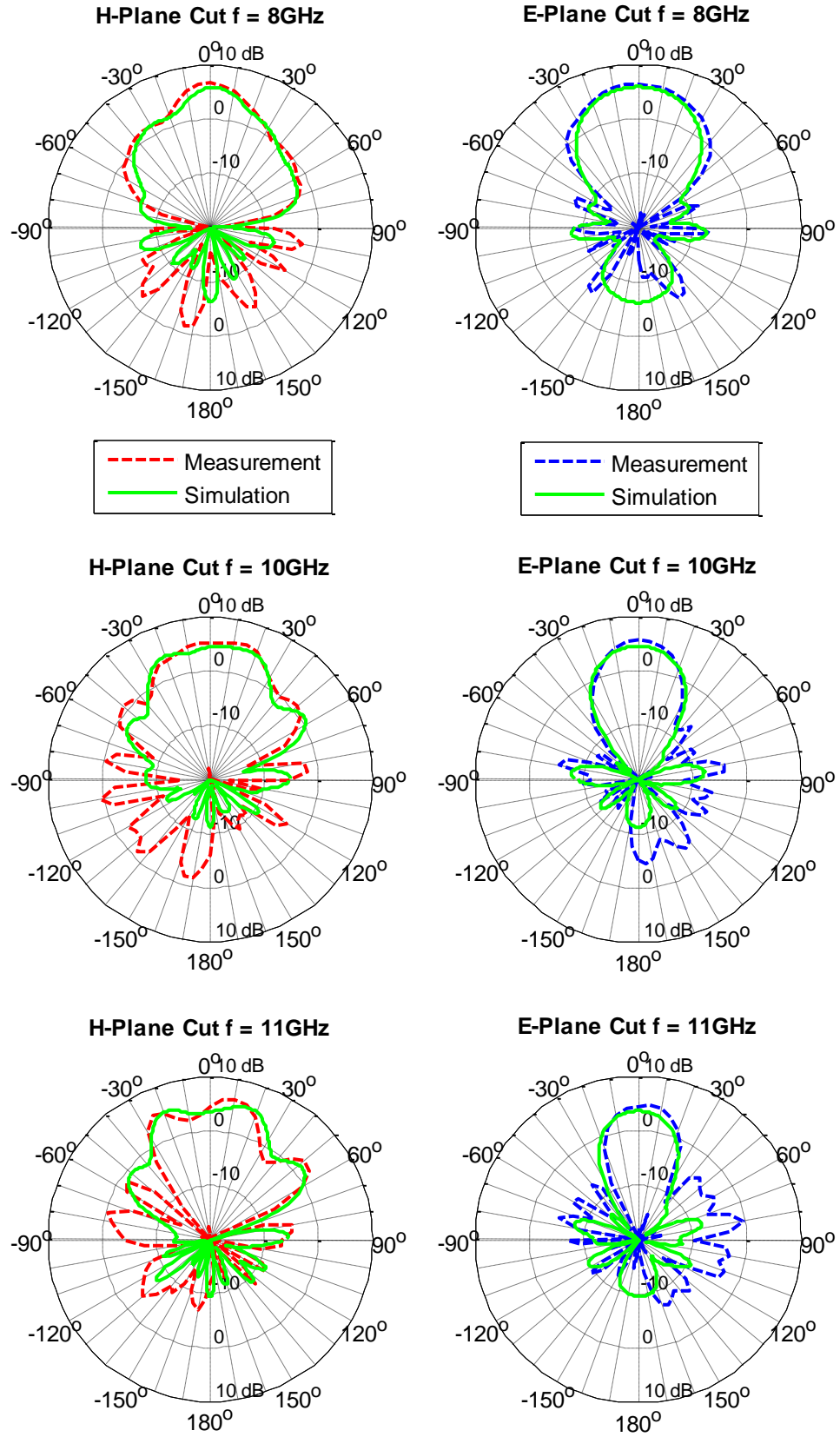


Figure 72: Vivaldi Radiation Pattern

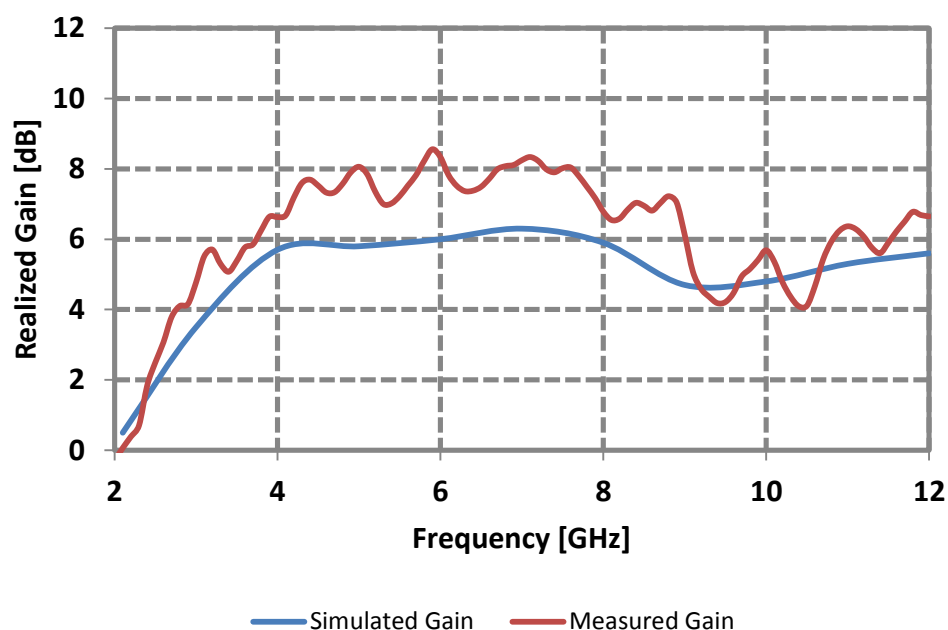


Figure 73: Vivaldi Gain vs. Frequency

### 5.1.3 Summary

The inkjet-printed antipodal Vivaldi, while failing to meet the simulated return loss, performs well over the entire UWB band with an average gain of 6.6 dBi over the band. It has the highest gain for currently publicized inkjet-printed antennas on paper, and provides a good solution for long range communications, energy harvesting, and many others.

## 5.2 UWB Antipodal Vivaldi Version 2

The measurements for the first antipodal Vivaldi show that several changes need to be made to match the antennas impedance better over the UWB band which will produce better gains. The time domain signal in Figure 75 shows that there is a small reflection at the transition (0.2 – 0.6 ns) and a large reflection at the end of the Vivaldi (1.25ns) when the arms terminate which is expected as there is a discontinuity.

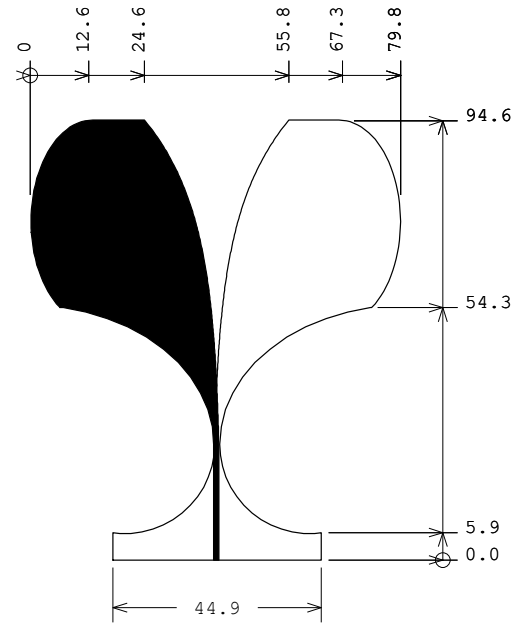


Figure 74: UWB Antipodal Vivaldi V2

In order to reduce the reflections occurring at the end of the Vivaldi, a smooth curve will be applied to the termination which should help eliminate abrupt changes.

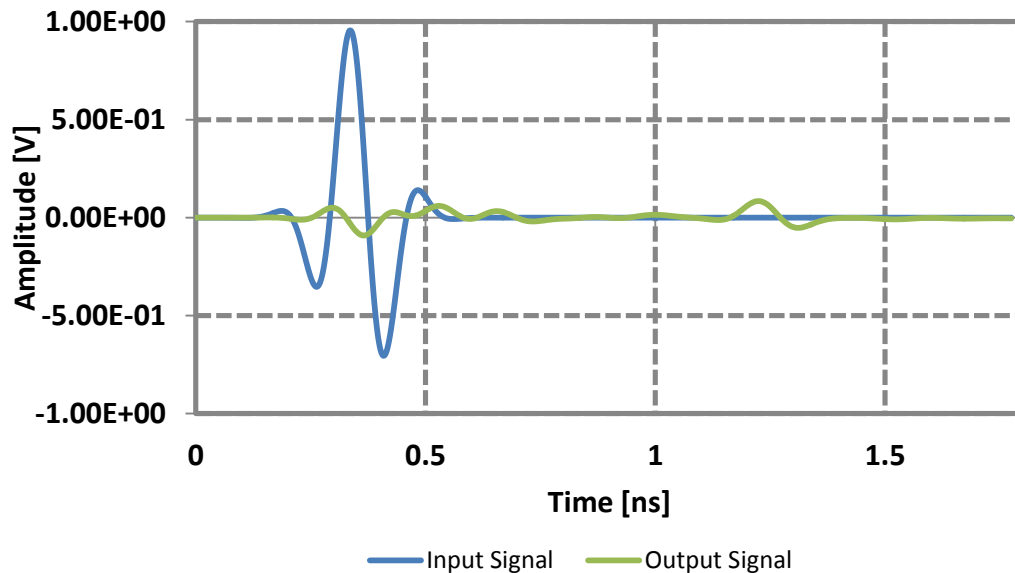


Figure 75: Vivaldi Version 1 Time Domain Signal

### 5.2.1 UWB Antipodal Vivaldi V2 Design

In order to enhance the frequency response of the Vivaldi, the ends of the arms are given a radius which smooths the discontinuity at the end. This can be seen in Figure 74. Due to the curved ends, the taper rate needs to be optimized to receive the best performance over the UWB band. The taper in this case is decreased from 0.055 to 0.05 which yields the following return loss. As seen it has a much better return loss and operates from 2.2 through 11 GHz. The time domain signals in Figure 77 shows the smaller end reflection from the smoother transition.

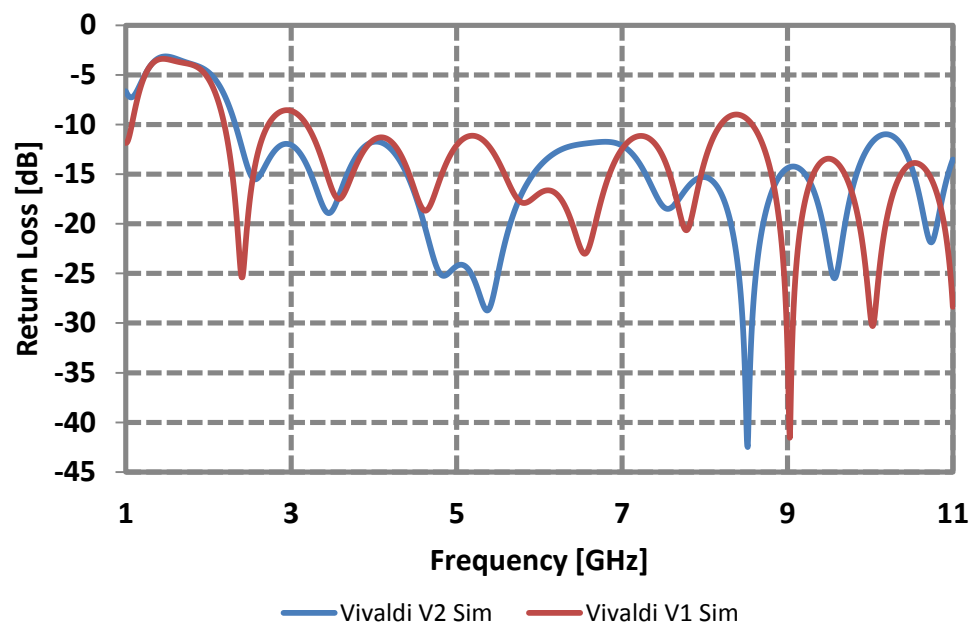


Figure 76: Vivaldi V2 vs. V1 Return Loss

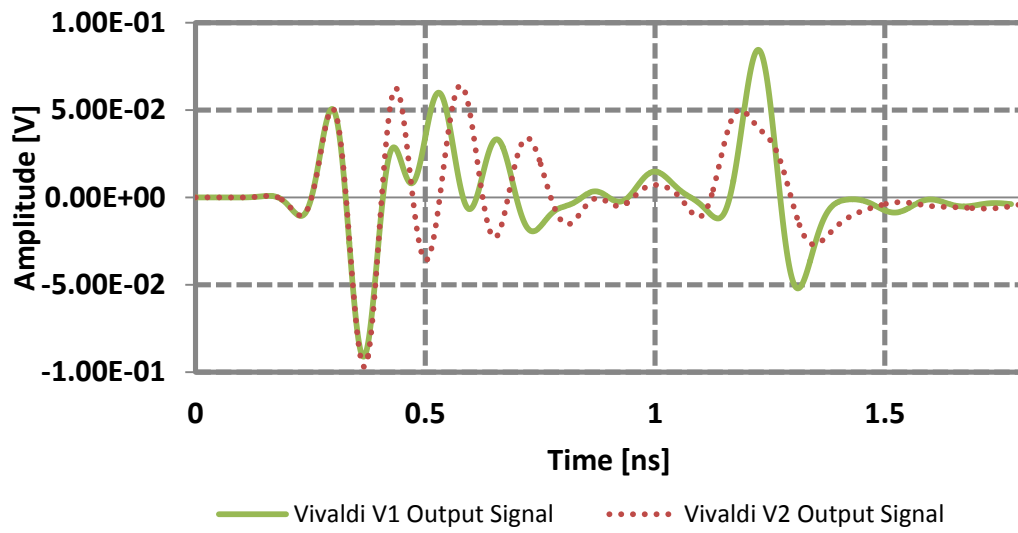


Figure 77: Minimized Time Domain Reflections

### 5.2.2 UWB Antipodal Vivaldi V2 Measurement

The final fabricated vivaldi is displayed in Figure 78. The same alignment methods were used as discussed in Section 4.1.2 to align the two halves of the antenna, except this time, the alignment pins are cross shaped instead of circular which allows for more precise alignment.

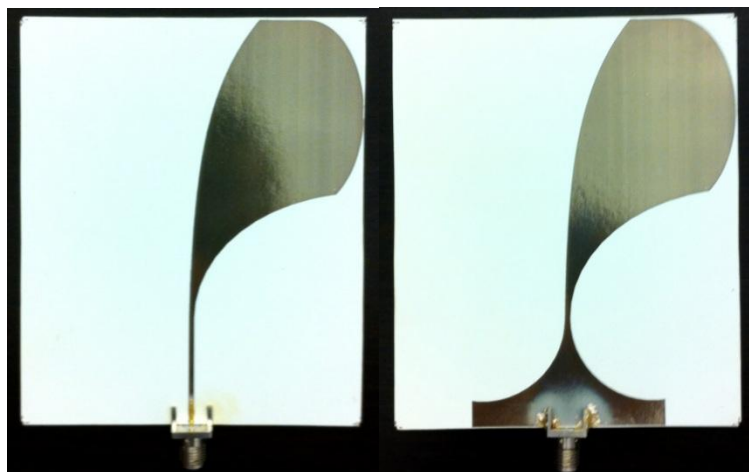


Figure 78: Fabricated Vivaldi V2

The return loss is first measured using an Agilent 8720ES 40GHz VNA in an anechoic chamber. The measured return loss is displayed in Figure 79.

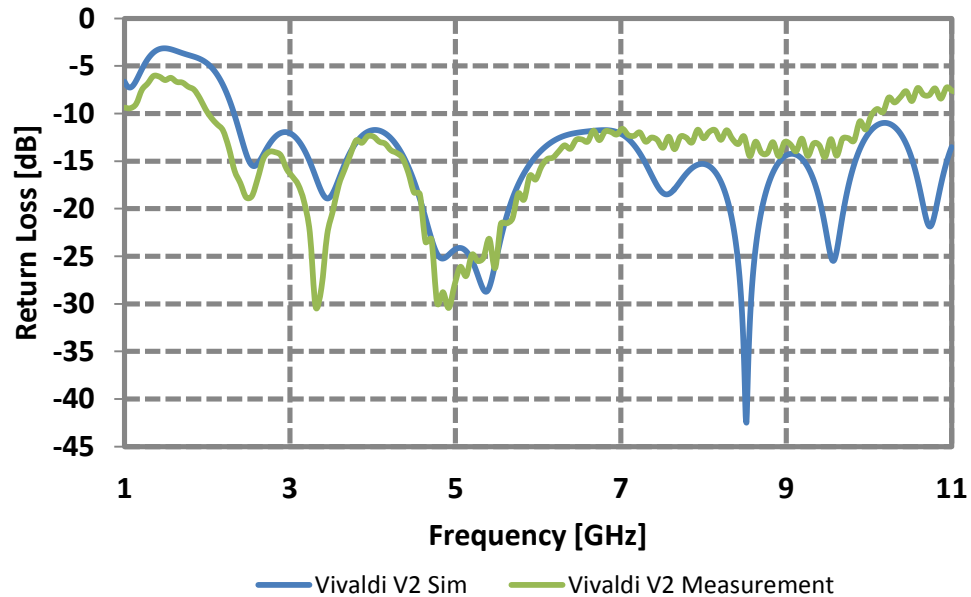
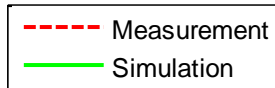
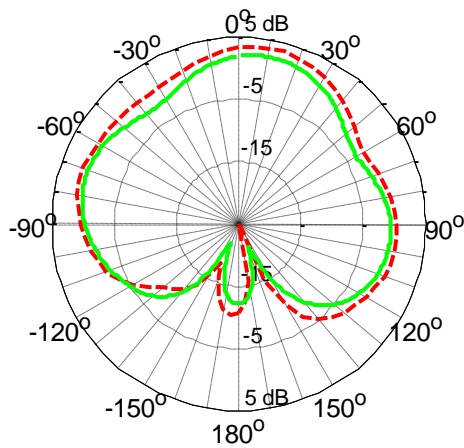
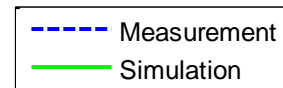
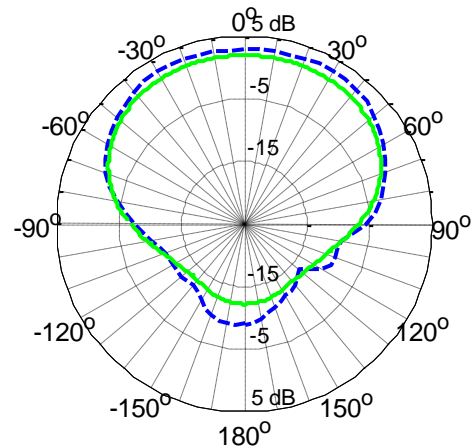
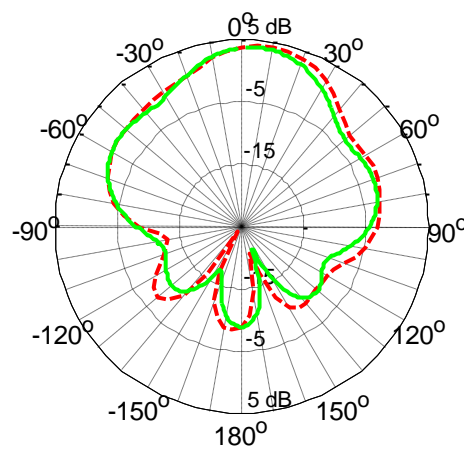
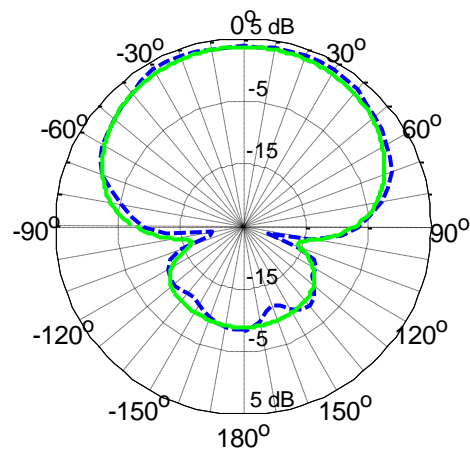
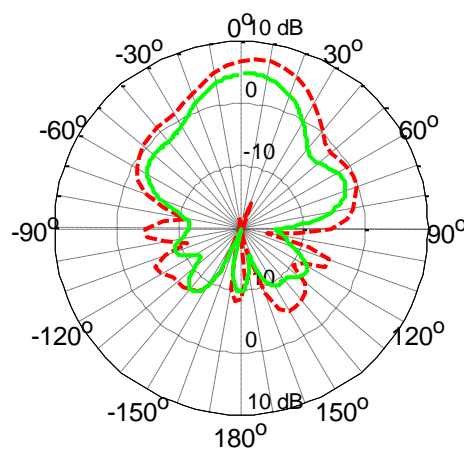
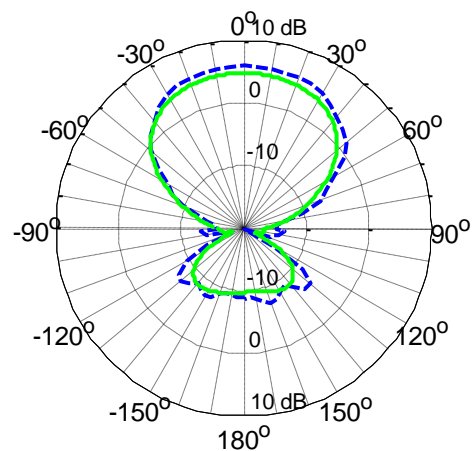


Figure 79: Vivaldi V2 Return Loss Measurements

The measured return loss values show the antenna operating from 2 – 10.4 GHz under -10dB. While the upper end of the UWB band is 10.6, the return loss is still -8.7 at this point meaning there is still a relatively good match. The operation is much better than that of the version 1 antipodal vivaldi. The radiation pattern and gain vs. frequency are shown in Figures 80 and 81 respectively.

The resulting data shows that the measured radiation is almost identical with the simulation, and the gain vs. frequency is much more stable than the first version of the vivaldi. This is due to the better high frequency matching achieved.

H-Plane Cut  $f = 3.1\text{GHz}$ E-Plane Cut  $f = 3.1\text{GHz}$ H-Plane Cut  $f = 4\text{GHz}$ E-Plane Cut  $f = 4\text{GHz}$ H-Plane Cut  $f = 6\text{GHz}$ E-Plane Cut  $f = 6\text{GHz}$ 



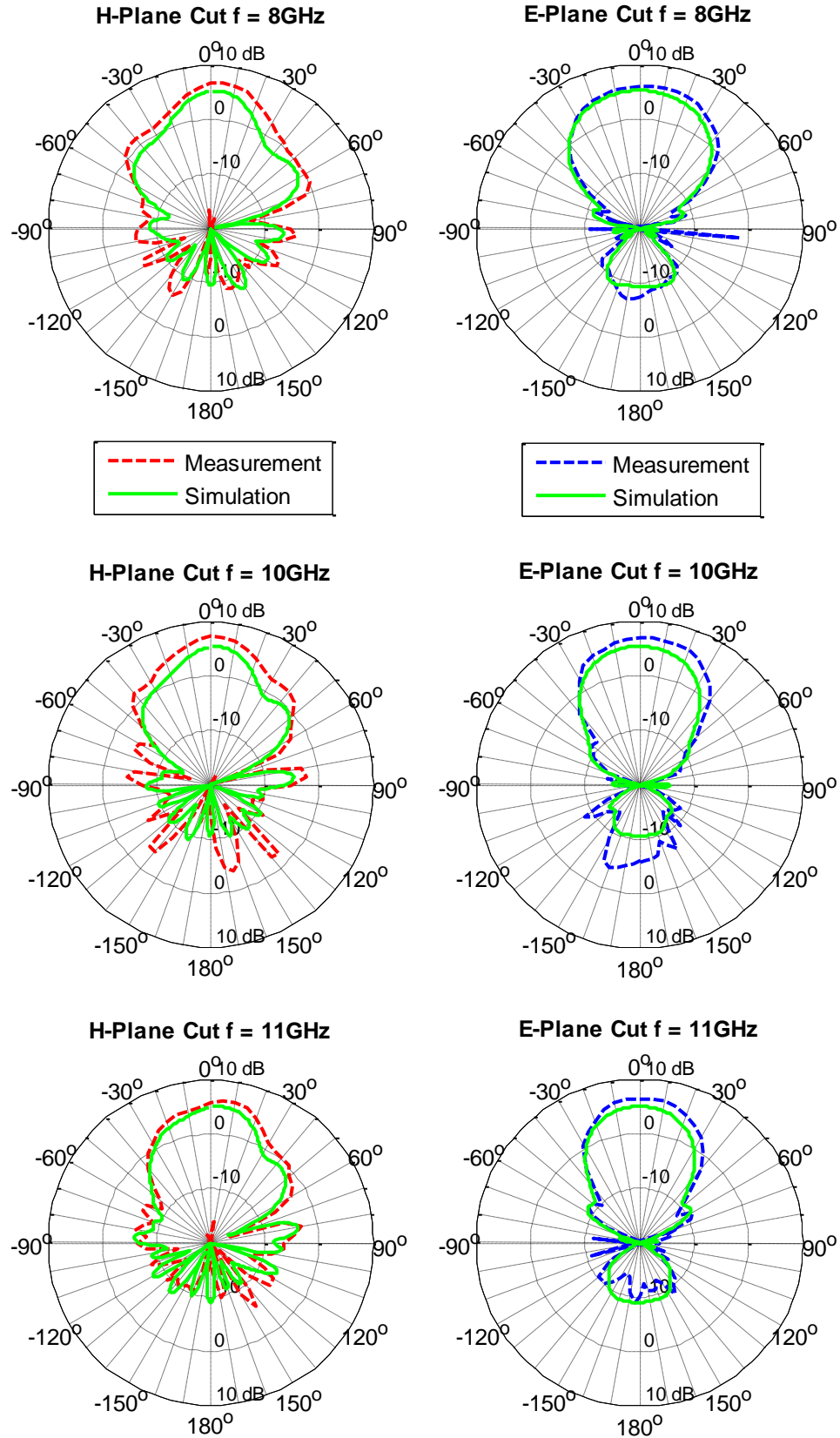


Figure 80: Vivaldi V2 Radiation Pattern Measurements

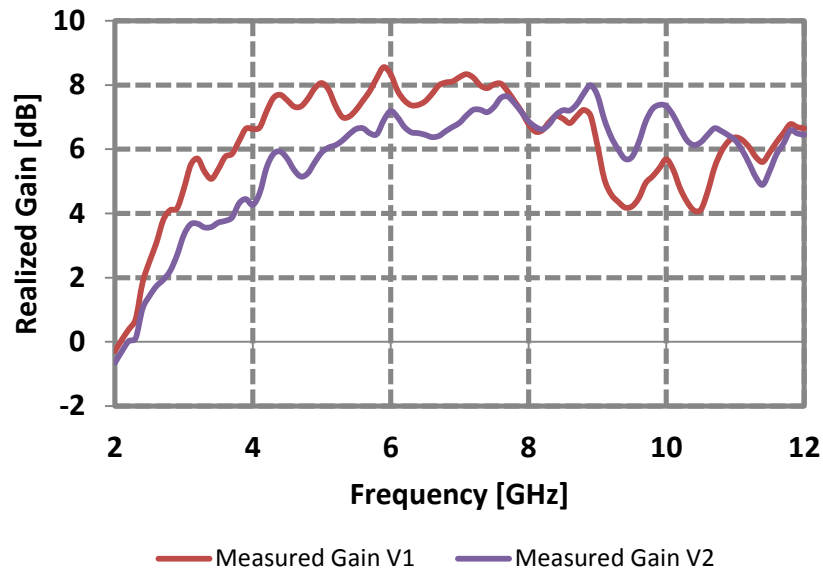


Figure 81: Vivaldi V2 Gain Measurements

The average in-band gain for UWB is 6.2dB which is only 0.4dB lower than the first version of the vivaldi and the gain is much more stable at the high end meaning the performance for this antenna is better for use over the entire UWB band.

### 5.2.3 Summary

Two separate antipodal Vivaldi antennas have been designed and measured with successful results. The gains have both surpassed all published inkjet-printed antennas at this time. The next steps will be to reduce ink usage and size for these antennas to make them more commercially viable solutions.

### 5.3 Applied Log Periodic Dipole Array with Slow Wave Structures

A series of inkjet-printed antennas have been investigated in the previous section, and a final applied antenna will be presented in this section which is used for energy harvesting from the UHF TV band in the U.S. As time goes on, many low cost and low powered sensors have appeared on the market that can be used as remote self-powered sensors operating off of scavenged energy.

The principle for this application is using a high gain antenna to capture energy from local television towers in the UHF band, rectify the signal, and charge a super capacitor or small battery so sensors can operate indefinitely without external power or battery replacement.

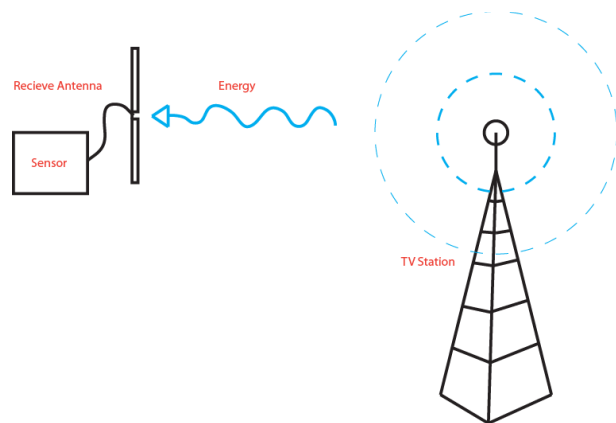


Figure 82: Energy Harvesting from UHF Band

For this application, a log periodic dipole array is chosen as the log periodic dipole array is directive and wideband – as energy captured is a product of the gain and bandwidth of the antenna wideband operation increases energy capture. As the antenna will be designed in the 400 – 600 MHz range, minimization techniques will need to be used to reduce the size of the antenna. The log periodic is chosen over the Vivaldi for exactly this reason – dipole arms are much easier to minimize than the traveling wave structure of the Vivaldi.

### 5.3.1 Log Periodic Dipole Array Design

The log periodic dipole array is shown in Figure 83. It is a traveling wave antenna meaning that over a certain frequency band, one pair of arms is active while the others act as directors and reflectors similar to a Yagi Uda parasitic antenna. However, instead of radiating in the direction of wave travel on the antenna, the antenna radiates backwards.

If the antenna is viewed as an infinite array of isotropic radiators with equal spacing, a case where the angle  $\alpha$  goes

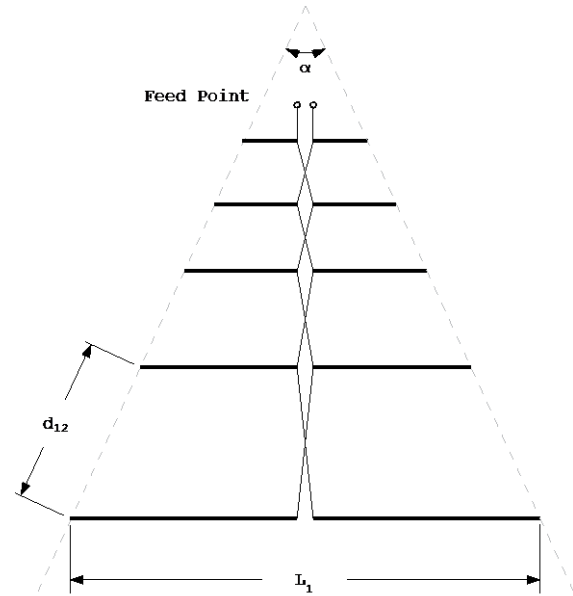


Figure 83: Log Periodic Design

to zero, the far field pattern can be represented by (16) where  $N$  is the number of radiators,  $K$  equivalent to  $2\pi/\lambda$ ,  $d$  is the spacing between elements, and  $\alpha$  is the relative phase shift between elements [48].

$$|E| = 1 + \sum_{n=1}^{N-1} e^{-inKd \cos \phi + \alpha} \quad (16)$$

The magnitude of radiation is maximum when the quantity in the exponent is zero, meaning:

$$\phi = \cos^{-1} \frac{-\alpha}{Kd} \quad (17)$$

When there is no phase shift, meaning  $\alpha = 0$ ,  $\phi = \pm 90$ , it produces a broadside radiation pattern. If the phasing of the array is lagging, the beam shifts forwards,

and if the phase is leading, the beam shifts backwards. In the active region, the phase shift between elements is:

$$\alpha = \pi - Kd \quad (18)$$

The  $\pi$  comes from the  $180^\circ$  phase shift between elements and  $Kd$  is the free space phase shift due to travel time of the wave between the elements. As  $d$  is typically around a quarter wavelength in the active region,  $\alpha$  leads by  $90^\circ$ . This produces a backwards firing beam typical of the log periodic.

In designing the log periodic (Reference Figure 83), the spacing and length of the elements are determined  $\tau$ , the ratio of lengths between adjacent elements, and  $\sigma$ , the relative spacing coefficient whereas [48]:

$$d_{12} = \frac{1}{2}(L_1 - L_2)\alpha \quad (19)$$

$$\cot \alpha = \frac{4\sigma}{1 - \tau} \quad (20)$$

A typical rule is that as  $\tau$  approaches 1, meaning adjacent arms are identical in length, the gain increases, though there is an optimum spacing  $\sigma$  that will give the highest gain for any given  $\tau$ .

The bandwidth of the antenna is a function of the longest and shortest elements, the longest element setting a lower bound on the frequency of operation and the shortest element setting an upper bound. In order to decrease the element lengths and keep the same operating frequencies, a slow-wave minimization technique

which staggers the inductance and capacitance of the dipole arms, similar to that of a stepped impedance filter on a transmission line, will be used. Meandering the arms causes cross polarization, so using the stepped L-C approach will give better radiation characteristics for the antenna [49]. Figure 84 shows different L-C staggered dipoles and the corresponding return loss is displayed in Figure 85.

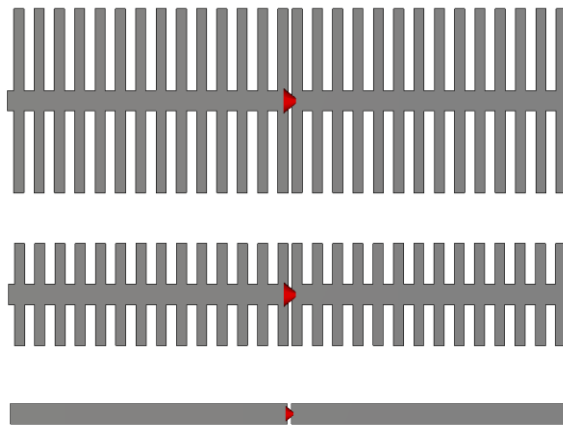


Figure 84: Stepped Capacitor 400% Dipole Width (Top), 200% (Middle), 0% (Bottom)

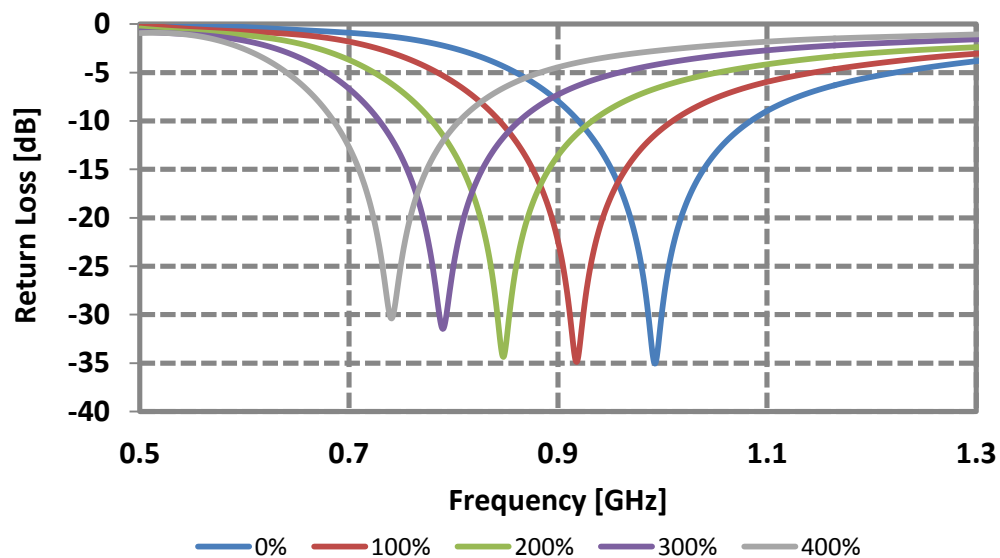


Figure 85: Return Loss for Stepped Capacitor Dipoles

As shown by simulation results, stepped impedance arms yield up to 23% length reduction using a 4 to 1 step width ratio.

For the final version of the printed log periodic, a 2 to 1 ratio for stepped impedance is used. The target capture frequency is 525MHz, so arms with resonance of 450 – 550MHz are used. A value of 0.93 for  $\tau$ , and  $\sigma$  was parametrically swept over a confined range of 0.11 to 0.16 which yields a directivity of 6 – 9 in design tables to find the best match and gain for 450 – 550 MHz. The optimum  $\sigma$  is 0.11 which yields the antenna in Figure 86.

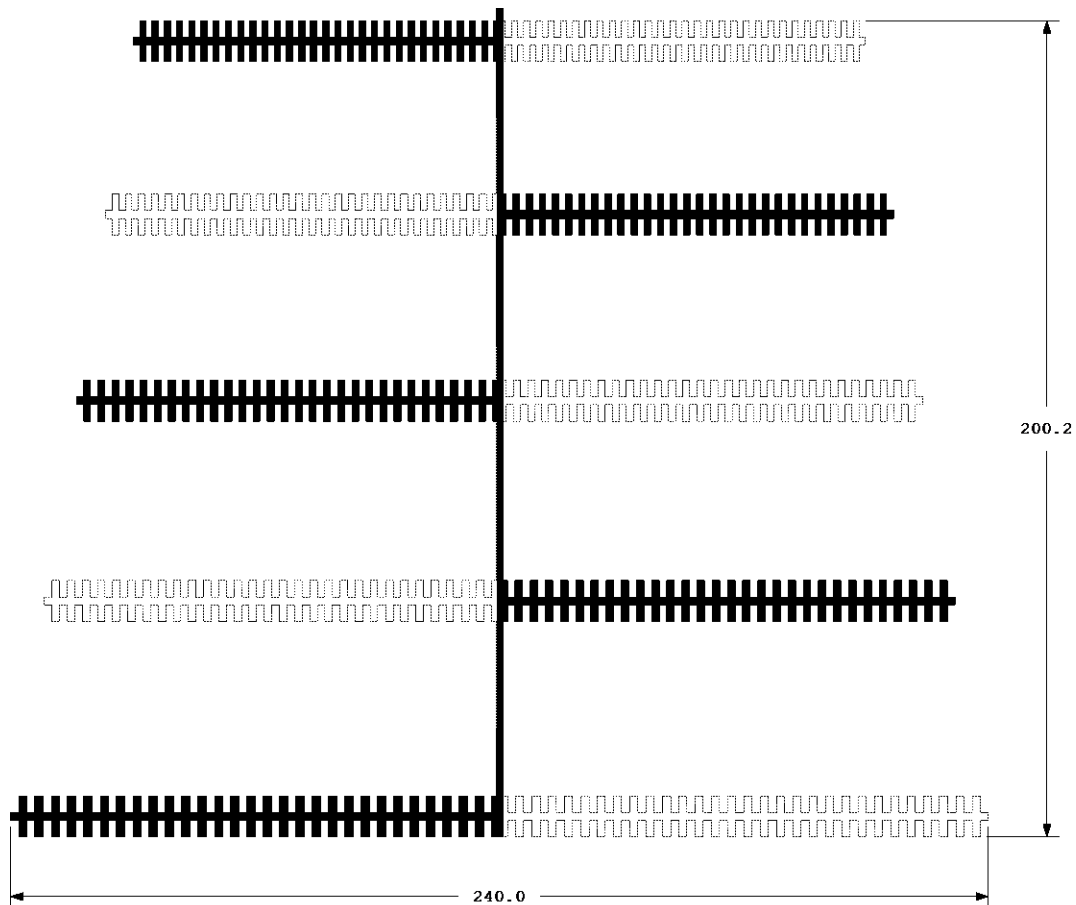


Figure 86: Final Log Periodic

The simulated return loss is shown in Figure 87.

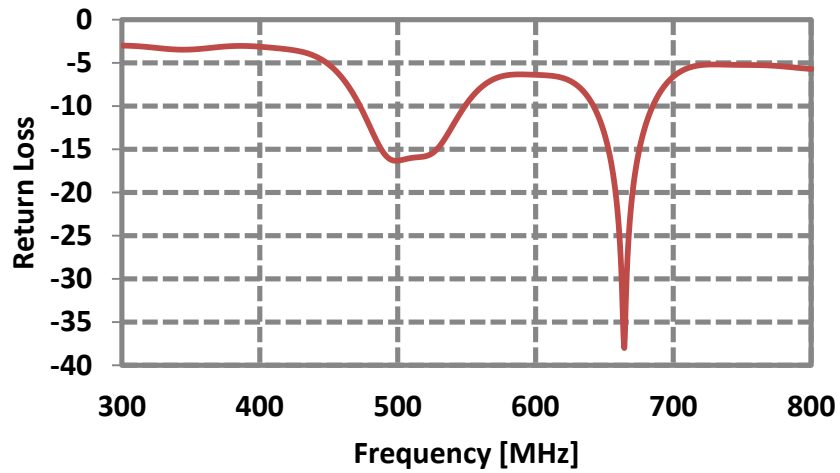


Figure 87: Log Periodic Simulated Return Loss

As seen by the return loss, the antenna operates from 480 – 550 MHz. The gain vs. frequency is displayed in Figure 88.

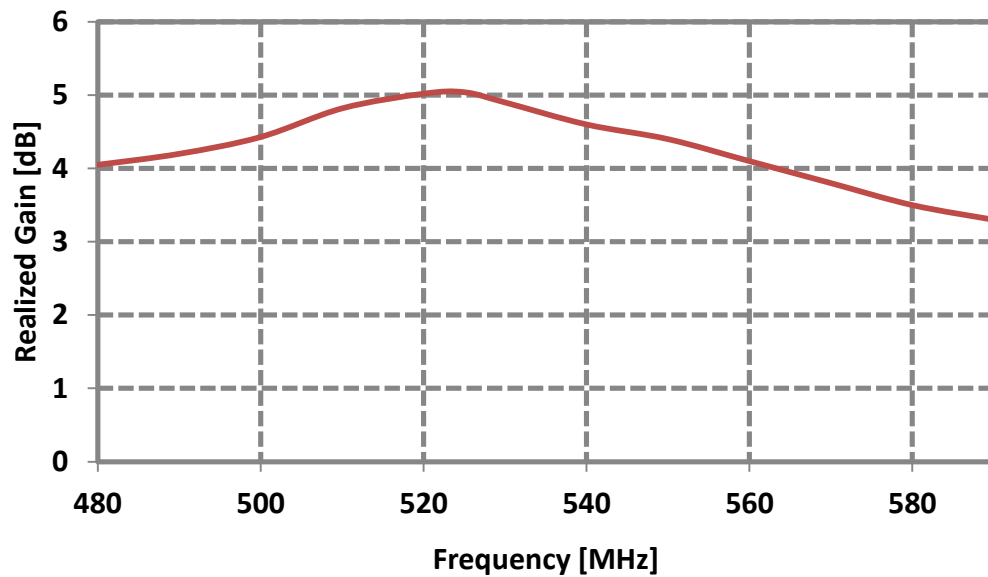


Figure 88: Log Periodic Simulated Gain



A simulated radiation pattern is shown below.

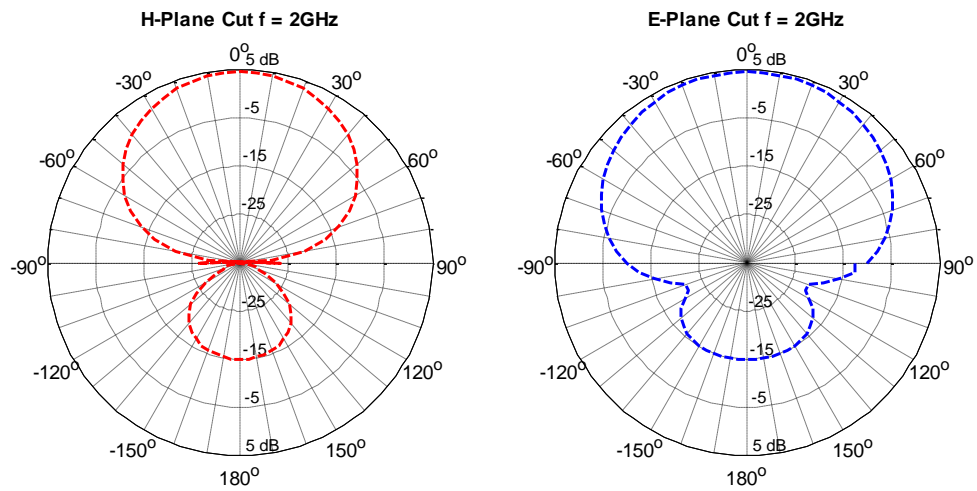


Figure 89: Log Periodic Simulated Radiation Pattern

### 5.3.2 Log Periodic Measurements

The final fabricated log periodic is displayed in Figure 90. As seen, the infinite balun runs along the top of the feed line and the center conductor wraps around to the opposing side

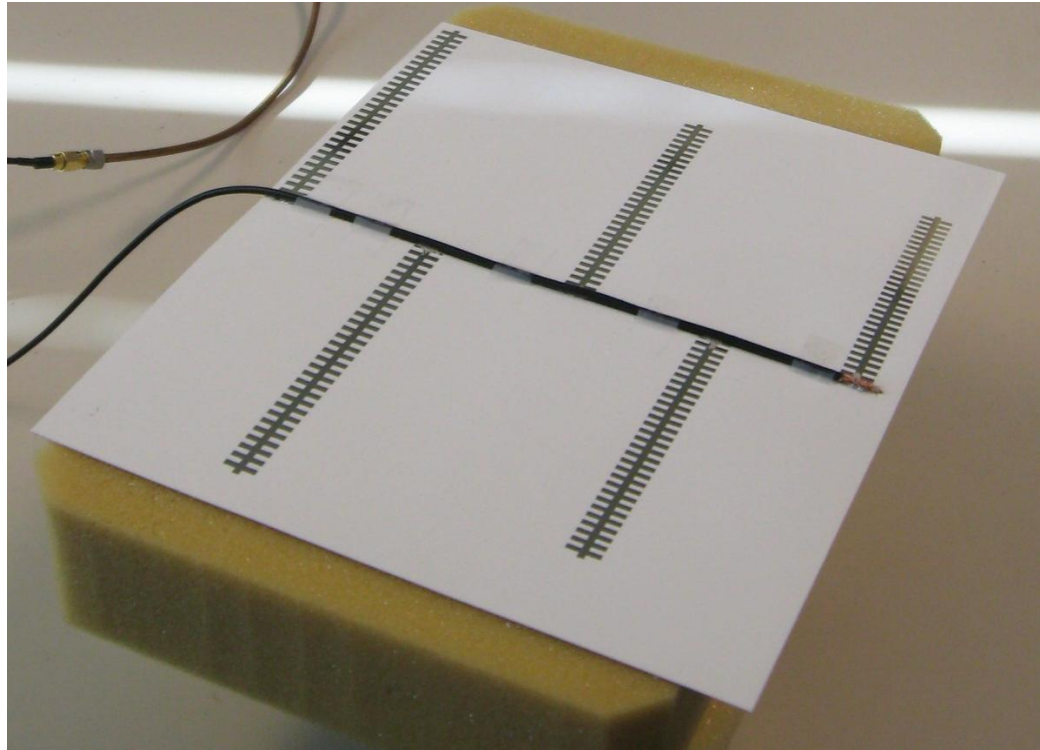


Figure 90: Fabricated Log Periodic

To feed the log periodic, an infinite balun is used. This is where a coaxial cable is run along the top of one side of the log periodic, directly over the feed line. The outside of the coaxial cable is soldered to the feed line, and the inner conductor is wrapped around to the opposite side of the feed line. This allows currents to flow on the bottom feed line and top feed line/outside of the outer conductor. But, these

currents will not cause radiation on the cable due to the truncation of the lower feed line.

The return loss is measured on a Rhode and Schwartz 8 GHz VNA and is displayed below. As seen, the main resonance point follows the simulation very well, and the second resonance point which is not of interest falls 50MHz from the simulation.

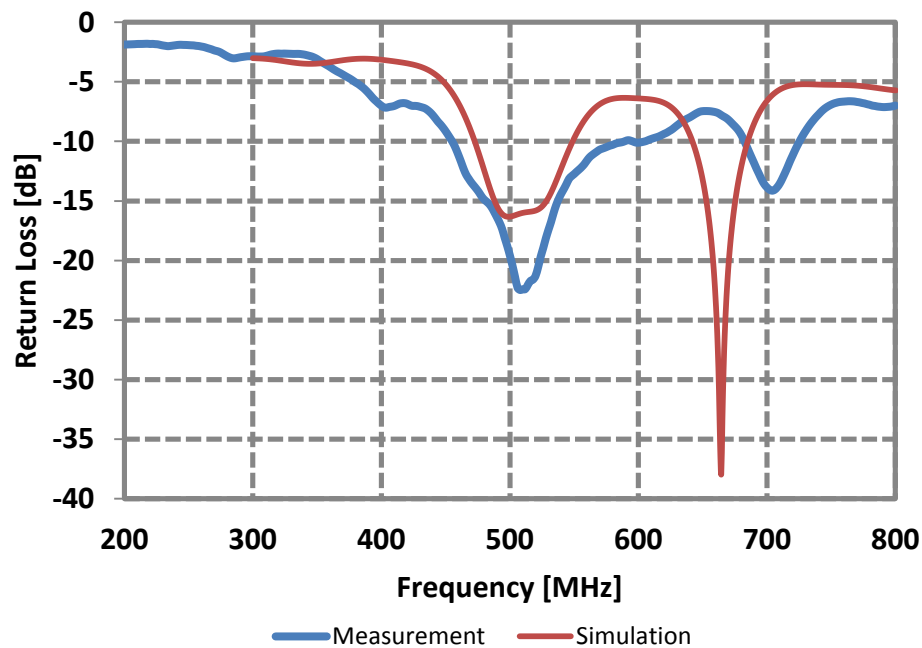


Figure 91: Log Periodic Simulated and Measured Return Loss

The pattern is not measured for this antenna as it was not able to be transported to Saudi Arabia in time. However, the maximum gain vs. frequency is measured and plotted against simulated gain vs. frequency below using an anechoic chamber, signal generator, and spectrum analyzer with a known receive antenna. As shown, the gain is very close to the simulation, and the gain pattern follows very well.

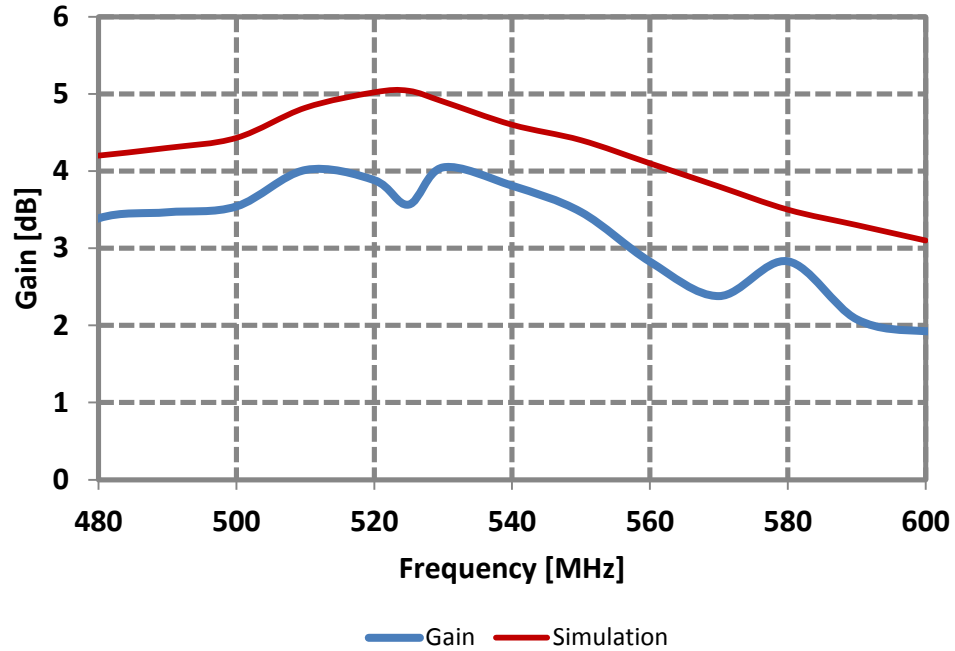


Figure 92: Log Periodic Simulated and Measured Gain

### 5.3.3 Summary

As demonstrated, an inkjet-printed log periodic dipole has been designed using slow wave structures to minimize the arm widths by 20%. The antenna is fabricated and the measurements show good agreement with the simulated results. Further miniturization can be done and will be pursued in future work.

## 6. CONCLUSIONS

---

### 6.1 Conclusions

The work presented in this thesis first tackles the characterization of the ink-jet fabrication process and several polymer and organic substrates for microwave frequency operation including paper, Kapton, and PET. The characterization data is then used in the design of several wideband, and wideband high-gain antennas for fabrication on paper based substrates.

The fabricated antennas that were measured proved include the smallest UWB antenna to date that has been inkjetted along with three antennas reporting higher gains than ever before published for inkjet printed antennas.

The applications of the antennas created in this work can extend to wearable, high data rate, and long range applications, as well as energy harvesting for remote self-powered sensor networks.

### 6.2 Future Work

The work in this thesis is a gateway into the design and implementation of fully integrated ink-jetted systems on paper. This includes the fabrication of actives, sensors, passives, along with packaging all using the inkjet printing process on paper and other polymer and organic substrates to create low-cost, flexible, and disposable systems.

---

## WORKS CITED

---

- [1] G. Wiederrecht, *Handbook of nanofabrication*. Boston, MA: Elsevier, 2009.
- [2] W. S. Wong, Ed., *Flexible Electronics* (Electronic Materials: Science and Technology). Springer, 2009, p.^pp. Pages.
- [3] S. K. Volkman, S. Molesa, B. Mattis, P. C. Chang, and V. Subramanian, "Inkjetted organic transistors using a novel pentacene precursor," *Organic and Polymeric Materials and Devices*, vol. 771, pp. 391-396, 2003.
- [4] L. Yang, A. Rida, R. Vyas, and M. M. Tentzeris, "RFID tag and RF structures on a paper substrate using inkjet-printing technology," *Ieee Transactions on Microwave Theory and Techniques*, vol. 55, pp. 2894-2901, Dec 2007.
- [5] A. N. Tran and et al., "A new platform for RFID research in Vietnam," *Advances in Natural Sciences: Nanoscience and Nanotechnology*, vol. 1, p. 045015, 2010.
- [6] A. C. Siegel, S. T. Phillips, M. D. Dickey, N. S. Lu, Z. G. Suo, and G. M. Whitesides, "Foldable Printed Circuit Boards on Paper Substrates," *Advanced Functional Materials*, vol. 20, pp. 28-35, Jan 8 2010.
- [7] L. Yang, R. W. Zhang, D. Staiculescu, C. P. Wong, and M. M. Tentzeris, "A Novel Conformal RFID-Enabled Module Utilizing Inkjet-Printed Antennas and Carbon Nanotubes for Gas-Detection Applications," *Ieee Antennas and Wireless Propagation Letters*, vol. 8, pp. 653-656, 2009.

- [8] L. Yang, A. Rida, and M. M. Tentzeris, "Design and Development of Radio Frequency Identification (RFID) and RFID-Enabled Sensors on Flexible Low Cost Substrates," *Synthesis Lectures on RF/Microwaves*, vol. 1, pp. 1-89, 2009/01/01 2009.
- [9] R. Vyas, V. Lakafosis, H. Lee, G. Shaker, L. Yang, G. Orecchini, A. Traille, and M. Tentzeris, "Inkjet Printed, Self Powered, Wireless Sensors for Environmental, Gas and Authentication Based Sensing," *Sensors Journal, IEEE*, vol. PP, pp. 1-1, 2011.
- [10] I. Mohammad and H. Huang, "Monitoring fatigue crack growth and opening using antenna sensors," *Smart Materials & Structures*, vol. 19, May 2010.
- [11] Y. Hyung Kuk, K. Woo Suk, Y. Young Joong, and L. Cheon-Hee, "A CPW-fed flexible monopole antenna for UWB systems," in *Antennas and Propagation Society International Symposium, 2007 IEEE, 2007*, pp. 701-704.
- [12] A. H. Rida, "CONDUCTIVE INKJET PRINTED ANTENNAS ON FLEXIBLE LOW-COST PAPER-BASED SUBSTRATES FOR RFID AND WSN APPLICATIONS," Masters of Science, EE, Georgia Institute of Technology, Atlanta, 2009.
- [13] A. Rashidian, D. M. Klymyshyn, M. T. Aligodarz, M. Boerner, and J. Mohr, "DEVELOPMENT OF POLYMER-BASED DIELECTRIC RESONATOR ANTENNAS FOR MILLIMETER-WAVE APPLICATIONS," *Progress in Electromagnetics Research C*, vol. 13, pp. 203-216, 2010.
- [14] A. Sridhar, "An Inkjet Printing-based Process Chain for Conductive Structures on Printed Circuit Board Materials," PhD., EE, University of Twente, Enschede, 2010.

- [15] S. Magdassi, A. Kamyshny, M. Ben-Moshe, and S. Aviezer, "Ink-jet printing of metallic nanoparticles and microemulsions," *Macromolecular Rapid Communications*, vol. 26, pp. 281-288, Feb 21 2005.
- [16] K. Futera, M. Jakubowska, and G. Koziol, "Printed electronic on flexible and glass substrates," *Photonics Applications in Astronomy, Communications, Industry, and High-Energy Physics Experiments 2010*, vol. 7745, 2010.
- [17] I. Microfab Technologies. (2010). *Microfab Technologies*. Available: [www.microfab.com](http://www.microfab.com)
- [18] I. Fujifilm Dimatix. (2011). *Dimatix*. Available: [www.dimatix.com](http://www.dimatix.com)
- [19] I. ULVAC Technologies. (2011). *ULVAC Technologies*. Available: <http://www.ulvac.com/flatpanel/litrexseries.asp>
- [20] G. Orecchini, F. Alimenti, V. Palazzari, A. Rida, M. M. Tentzeris, and L. Roselli, "Design and fabrication of ultra-low cost radio frequency identification antennas and tags exploiting paper substrates and inkjet printing technology," *Iet Microwaves Antennas & Propagation*, vol. 5, pp. 993-1001, Jun 6 2011.
- [21] G. Shaker, H. Lee, K. Duncan, and M. Tentzeris, "Integrated antenna with inkjet-printed compact artificial magnetic surface for UHF applications," in *Wireless Information Technology and Systems (ICWITS), 2010 IEEE International Conference on*, 2010, pp. 1-4.
- [22] A. Traille, L. Yang, A. Rida, T. Wu, and M. M. Tentzeris, "Design and Modeling of Novel Multiband/Wideband Antennas for RFID Tags and Readers Using Time-



/Frequency-Domain Simulators," in *Computational Electromagnetics in Time-Domain, 2007. CEM-TD 2007. Workshop on, 2007*, pp. 1-3.

[23] Y. Amin, S. Prokkola, S. Botao, J. Hallstedt, H. Tenhunen, and Z. Li-Rong, "Inkjet printed paper based quadrate bowtie antennas for UHF RFID tags," in *Advanced Communication Technology, 2009. ICACT 2009. 11th International Conference on, 2009*, pp. 109-112.

[24] A. Rida, Y. Li, T. Reynolds, E. Tan, S. Nikolaou, and M. M. Tentzeris, "Inkjet-printing UHF antenna for RFID and sensing applications on Liquid Crystal Polymer," in *Antennas and Propagation Society International Symposium, 2009. APSURSI '09. IEEE, 2009*, pp. 1-4.

[25] M. M. Tentzeris, A. Traille, L. Hoseon, A. Rida, V. Lakafosis, and R. Vyas, "Inkjet-printed paper/polymer-based 'green' RFID and Wireless Sensor Nodes: The final step to bridge cognitive intelligence, nanotechnology and RF?," in *Microwave Conference Proceedings (APMC), 2010 Asia-Pacific, 2010*, pp. 291-294.

[26] T. Yasin and R. Baktur, "Inkjet printed patch antennas on transparent substrates," in *Antennas and Propagation Society International Symposium (APSURSI), 2010 IEEE, 2010*, pp. 1-4.

[27] K. Kirschenmann, K. W. Whites, and S. M. Woessner, "Inkjet printed microwave frequency multilayer antennas," in *Antennas and Propagation Society International Symposium, 2007 IEEE, 2007*, pp. 924-927.

- [28] M. Y. Chen, X. Lu, H. Subbaraman, and R. T. Chen, *Fully printed phased-array antenna for space communications* vol. 7318: SPIE, 2009.
- [29] G. Shaker, A. Rida, S. Safavi-Naeini, M. M. Tentzeris, and S. Nikolaou, "Inkjet printing of UWB antennas on paper based substrates," in *Antennas and Propagation (EUCAP), Proceedings of the 5th European Conference on*, 2011, pp. 3001-3004.
- [30] (2011). *UT Dots*. Available: <http://www.utdots.com/>
- [31] Cabot. (2011). *Cabot Nanoparticle Ink*. Available: <http://www.cabot-corp.com/New-Product-Development/Printed-Electronics/Products>
- [32] M. L. Allen, M. Aronniemi, T. Mattila, A. Alastalo, K. Ojanpera, M. Suhonen, and H. Seppa, "Electrical sintering of nanoparticle structures," *Nanotechnology*, vol. 19, Apr 30 2008.
- [33] Dupont, "Kapton Data Sheet," Dupont, Ed., ed, 2010.
- [34] D. C. Thompson, O. Tantot, H. Jallageas, G. E. Ponchak, M. M. Tentzeris, and J. Papapolymerou, "Characterization of liquid crystal polymer (LCP) material and transmission lines on LCP substrates from 30 to 110 GHz," *Ieee Transactions on Microwave Theory and Techniques*, vol. 52, pp. 1343-1352, Apr 2004.
- [35] J. M. Heinola and K. Tolsa, "Dielectric characterization of printed wiring board materials using ring resonator techniques: A comparison of calculation models," *Ieee Transactions on Dielectrics and Electrical Insulation*, vol. 13, pp. 717-726, Aug 2006.

- [36] R. Hopkins, "The Microstrip Ring Resonator for Characterising Microwave Materials," University of Surrey, Guildford 2006.
- [37] K. P. Latti, M. Kettunen, J. P. Stoem, and P. Silventoinen, "A review of microstrip T-Resonator method in determining the dielectric properties of printed circuit board materials," *Ieee Transactions on Instrumentation and Measurement*, vol. 56, pp. 1845-1850, Oct 2007.
- [38] A. R. Fulford and S. M. Wentworth, "Conductor and dielectric-property extraction using microstrip tee resonators," *Microwave and Optical Technology Letters*, vol. 47, pp. 14-16, Oct 5 2005.
- [39] K. L. Wong and Y. F. Lin, "Stripline-fed printed triangular monopole," *Electronics Letters*, vol. 33, pp. 1428-1429, Aug 14 1997.
- [40] X. L. Liang, S. S. Zhong, and W. Wang, "UWB printed circular monopole antenna," *Microwave and Optical Technology Letters*, vol. 48, pp. 1532-1534, Aug 2006.
- [41] R. Rouhi, C. Ghobadi, J. Nourinia, and M. Ojaroudi, "Microstrip-Fed Small Square Monopole Antenna for Uwb Application with Variable Band-Notched Function," *Microwave and Optical Technology Letters*, vol. 52, pp. 2065-2069, Sep 2010.
- [42] D. H. Werner and S. Ganguly, "An overview of fractal antenna engineering research," *Ieee Antennas and Propagation Magazine*, vol. 45, pp. 38-57, Feb 2003.

- [43] H. Oraizi and S. Hedayati, "Miniaturized UWB Monopole Microstrip Antenna Design by the Combination of Giuseppe Peano and Sierpinski Carpet Fractals," *Ieee Antennas and Wireless Propagation Letters*, vol. 10, pp. 67-70, 2011.
- [44] S. T. Choi, K. Harnaguchi, and R. Kohno, "A Novel Microstrip-Fed Ultrawideband Triangular Monopole Antenna with Wide Stubs," *Microwave and Optical Technology Letters*, vol. 51, pp. 263-266, Jan 2009.
- [45] KACST. (2011). *King Abdullahziz City for Science and Technology*. Available: <http://www.kacst.edu.sa/>
- [46] G. Breed, "Wireless USB Uses Ultra Wideband (UWB) for High Data Rate," *High Frequency Electronics*, 2005.
- [47] M. A. Peyrot-Solis, G. M. Galvan-Tejada, and H. Jardon-Aguilar, "A novel planar UWB monopole antenna formed on a printed circuit board," *Microwave and Optical Technology Letters*, vol. 48, pp. 933-935, May 2006.
- [48] H. Kneve, "Design of Microwave Printed Circuit Log - Periodic Antennas," PhD., McMaster University, 1977.
- [49] B. Ghosh, S. M. Haque, and D. Mitra, "Miniaturization of Slot Antennas Using Slit and Strip Loading," *Antennas and Propagation, IEEE Transactions on*, vol. 59, pp. 3922-3927, 2011.